Magnetic Behavior of Cobalt Atoms at Long Copper Chains Studied with Scanning Tunneling Microscopes

Dissertation
in fulfilment of the requirements for the degree of
doctor of natural sciences
of the Faculty of Mathematics and Natural Sciences
at Kiel University
submitted by
Neda Noei
Kiel, 2020

First Examiner: Prof. Dr. Richard Berndt

Second Examiner: Prof. Dr. Stefan Heinze

Date of oral examination: 27.10.2020

Declaration of Authorship

I hereby declare on oath that I have prepared this work independently under the advice of my supervisor and that I have not used any other aids except those specified in the text and the known reference works of the natural sciences. This work was not submitted in whole or in part elsewhere as part of an examination procedure. I have not made any previous attempts for a PhD study. The work was carried out in compliance with the rules of good scientific practice of the German Research Foundation. The following part of the thesis is published in scientific journal:

- Chapter 4

  Neda Noei, Alexander Weismann, Richard Berndt.
  Apparent tunneling barrier height and local work function of atomic arrays
  Beilstein J. Nanotechnol. **9**, 30483052 (2018).

Noei

“What one man calls God, another calls the laws of physics.”

Nikola Tesla

Abstract

Over the last decades, with the help of low-temperature scanning tunneling microscopy (STM) and scanning tunneling spectroscopy (STS), the magnetic and electronic properties of magnetic atoms were studied on metal substrates and insulating layers. Depending on the underlying substrates, scientists were able to focus on their physical phenomenon of interest. When a magnetic atom is in direct contact with a metallic substrate, its interaction with the bath of conduction electrons of the host metal leads to many-body quantum effects such as the Kondo effect [1]. Several experiments were performed to study the evolution of the Kondo effect with changing the atomic environment of a localized spin. Despite the great results obtained from these experiments, a fully understood picture still remains a challenge.

A practical way to simplify the study of adatoms on solids is to reduce the interaction of the deposited atom with the conduction electron bath by an insulating layer. Using decoupling layers such as Cu_2N, Al_2O_3, and MgO the magnetic behavior of Fe, Mn, and Co adatoms were studied [2–7]. Obtaining a large magnetic anisotropy energy (MAE) for these systems was a great achievement to tailor magnetism in the smallest levels. However, still one of the challenging tasks in magnetism is maximizing the MAE for transition metal systems.

In this work, by using the ability of STM to create dislocations in crystals, the difficult and time-consuming procedure of fabricating nano-structures by atom manipulation has been avoided. Long Cu chains up to 200 nm were fabricated and used to study the Kondo effect of Co adatom. By attaching Co atom to a monatomic Cu chain, its asymmetric Kondo resonance altered to a resonance symmetric with respect to Fermi energy. Further study of the observed symmetric resonance in the presence of an external magnetic field revealed its inelastic excitation origin. By choosing a proper atomic environment for Co adatoms, we were able to modify its quenched orbital momentum, demonstrate the effect of the spin-orbit coupling on its energy spectrum and obtain a noticeable MAE.

Moreover, among the fabricated dislocations, we also observed chains and vacancy lines with different widths. They provided the opportunity to study the apparent tunneling barrier height (Φ_{app}) in scanning tunneling microscopy. The variation of experimental Φ_{app} for these nano-structures was not as expected by theory. A kinetic energy contribution to the tunneling process is proposed to be the reason of the unexpected experimental Φ_{app} trend.

Furthermore, by means of atom manipulation and STS, the role of surface state electrons in the Kondo effect of Co adatoms has been investigated; a topic with contradictory experimental observations. Using a step edge of a crystal to modulate the surface local density of states, we observed a negligible variation of the Kondo resonance width. This shows a minor role of surface state electrons in this many-body process.

Zusammenfassung

In den letzten Jahrzehnten wurden mit Hilfe der Niedertemperatur-Rastertunnelmikroskopie (STM) und der Rastertunnelspektroskopie (STS) die magnetischen und elektronischen Eigenschaften magnetischer Atome auf Metallsubstraten und Isolierschichten untersucht. In abhängig der zugrunde liegenden Substrate konnten sich die Wissenschaftler auf die sie jeweils interessierenden physikalisches Phänome konzentrieren.

Wenn ein magnetisches Atom in direktem Kontakt mit einem metallischen Substrat steht, führt seine Wechselwirkung mit dem Bad der Leitungselektronen des Wirtsmetalls zu Vielteilchen-Quanteneffekten wie dem Kondo-Effekt [1]. Es wurden mehrere Experimente durchgeführt, um die Entwicklung des Kondo-Effekts bei Veränderung der atomaren Umgebung eines lokalisierten Spins zu untersuchen. Trotz der herausragenden Ergebnisse dieser Experimente bleibt ein vollständig verstandenes Bild eine Herausforderung.

Eine gängige Methode, um die Untersuchung von Adatomen auf Festkörpern zu vereinfachen, besteht darin, die Wechselwirkung des abgeschiedenen Atoms mit den Leitungsbandelektronen durch eine Isolierschicht zu reduzieren. Mit Entkopplungsschichten wie Cu_2N, Al_2O_3 und MgO wurde das magnetische Verhalten von Fe-, Mn- und Co-Adatomen untersucht [2–7]. Eine großen magnetische Anisotropieenergie (MAE) für diese Systeme zu erhalten, war eine große Errungenschaft, um den Magnetismus auf kleinstem Niveau zu kontrollieren. Eine der herausfordernden Aufgaben im Magnetismus ist jedoch die Maximierung der MAE für Übergangsmetallsysteme.

In dieser Arbeit wurde durch Nutzung der Möglichkeit, mit einem STM Versetzungen in Kristallen zu erzeugen, das schwierige und zeitaufwendige Verfahren zur Herstellung von Nanostrukturen durch Atommanipulation vermieden. Lange Cu-Ketten bis zu 200 nm wurden hergestellt und verwendet, um den Kondo-Effekt von Co-Adatom zu untersuchen. Durch die Bindung des Co-Atoms an eine einatomige Cu-Kette änderte sich seine zuvor asymmetrische Kondo-Resonanz in eine spektrale Signatur, die in Bezug auf die Fermi-Energie symmetrisch ist. Weitere Untersuchungen der beobachteten symmetrischen Resonanz in Gegenwart eines externen Magnetfelds ergaben, dass diese eine inelastische Anregung darstellt. Durch Auswahl einer geeigneten atomaren Umgebung für Co-Adatome konnten wir das durch die Oberfläche reduzierte Orbitalmoment modifizieren, den Effekt der Spin-Orbit-Wechselwirkung auf das Energiespektrum demonstrieren und eine messbare MAE erhalten.

Darüber hinaus beobachteten wir bei den hergestellten Versetzungen auch Ketten und Gräben mit unterschiedlichen Breiten. Sie boten die Möglichkeit, die scheinbare Tunnelbarrierenhöhe (Φ_{app}) in der Rastertunnelmikroskopie zu untersuchen. Die Variation der experimentellen Φ_{app} für diese Nanostrukturen war theoretisch nicht erwartet. Ein kinetischer Energiebeitrag zum Tunnelprozess wird als Grund für den unerwarteten experimentellen Befund vorgeschlagen.

Darüber hinaus wurde mittels Atommanipulation und STS die Rolle von Elektronen im

Oberflächenzustand beim Kondo-Effekt von Co-Adatomen untersucht; ein Thema mit bisher widersprüchlichen experimentellen Beobachtungen. Unter Verwendung einer Stufenkante eines Kristalls zur Modulation der lokalen Zustandsdichte der Oberfläche beobachteten wir eine vernachlässigbare Variation der Breite der Kondo-Resonanz. Dies zeigt eine untergeordnete Rolle der Elektronen im Oberflächenzustand an diesem Vielteilchenprozess.

Contents

Declaration of Authorship iii

Abstract vii

Zusammenfassung viii

Introduction xv

1 Fundamentals 1
- 1.1 Theory of Scanning Tunneling Microscopy . . . 1
  - 1.1.1 Bardeen's Approach . . . 2
  - 1.1.2 Tersoff and Hamann STM Theory . . . 4
  - 1.1.3 Inelastic Tunneling . . . 5
- 1.2 Scanning Tunneling Spectroscopy . . . 6
  - 1.2.1 Broadening in Scanning Tunneling Spectroscopy . . . 6
  - 1.2.2 Inelastic Tunneling Spectroscopy . . . 8
- 1.3 Magnetism at the Atomic Scale . . . 8
  - 1.3.1 A Free Atom . . . 9
  - 1.3.2 Magneto-Crystalline Anisotropy . . . 10
- 1.4 The Total Spin System Hamiltonian . . . 10
  - 1.4.1 Spin Correlation of Localized Spins and Surrounding Host Electrons 12
- 1.5 The Kondo Effect . . . 14
  - 1.5.1 Metals with Magnetic Impurities . . . 14
  - 1.5.2 Kondo Effect of Co Atoms . . . 17
- 1.6 Work Function and Apparent Tunneling Barrier Height . . . 18
  - 1.6.1 Barrier Height Spectroscopy . . . 19

2 Experimental Setup 21
- 2.1 Low-Temperature STMs . . . 21
- 2.2 Tip and Sample Preparation . . . 23
- 2.3 Cobalt Evaporation . . . 24
- 2.4 Results and Discussion . . . 25

3 Kondo Effect of Co Atoms at Long Cu Chains 29
- 3.1 Copper Chain Fabrication . . . 29
- 3.2 Atom Manipulation and Co_nCu_m Chains . . . 32

3.3 Magnetic Field Measurements on Co Atom at the Side of a Monatomic Chain 36
3.3.1 Magnetic Field in Z Direction 36
3.3.2 Magnetic Fields in X and Y Directions 38
3.4 Interaction Between Co Atoms at Long Cu Chain 39
3.4.1 Co Atoms at Chain with Large Separation 40
3.4.2 Co Atoms at Chain with Small Separation 42
3.5 Discussion 44
3.5.1 Selective Hybridization of $3d$ Orbitals 45

4 Apparent Tunneling Barrier Height of Atomic Arrays 49
4.1 Introduction 49
4.2 Experiment 50
4.3 Results and Discussion 51

5 Surface State Role in the Kondo Effect of Co Adatom on Cu(111) 55
5.1 Introduction 55
5.2 Kondo Effect of Co Adatoms Close to a Step Edge on Cu(111) 56
5.2.1 Distance Determination 57
5.3 Results and Conclusion 59

6 Conclusion and Outlook 63

A B-field Data Analysis 67
A.1 Tip Effect Removal 67
A.2 Noise Removal 69

Bibliography 71

List of Figures 82

List of Tables 89

Abbreviations 91

Acknowledgements 93

To Shahab

Introduction

Understanding the electric behavior of adatoms in different environments is the starting point to use them as the building blocks of electronic devices. Down at the atomic level, the manipulation of spin and orbital angular momenta showed their great potential as an alternative choice for achieving the size reduction demand for electronic devices. However, although these fundamental concepts can be studied conveniently in detail for a free particle, introducing an atomic environment to the picture complicates the subject matter.

When atoms and molecules are deposited on solids, their charge, spin and orbital angular momenta are affected by their underlying substrates. The electronic structure of the deposited atom is determined by the electric behavior and the crystallographic orientation of the substrate atoms. The direction and the strength of hybridization between the substrate and the impurity affect the orbital angular momentum of the impurity and create magnetic anisotropy. The magneto-crystalline anisotropy defines the orientation and stability of magnetization and is an essential factor in the design of magnetic materials.

In the present work, the magnetic behavior of Co adatoms on Cu(111) substrate has been investigated. For this purpose, two low temperature STMs were used; one operated at 4.6 K and the other at 350 mK and equipped with magnets. STS and inelastic electron tunneling spectroscopy (IETS) were used to detect the Kondo effect and magnetic excitations of the Co atoms. This thesis is presented as follows:

Chapter one is an introduction to the fundamentals. After explaining the theory and working principles of STM, the Kondo effect and magneto-crystalline anisotropy is introduced. The spin Hamiltonian which is a simple model to interpret the measured spin state in STM experiments is explained briefly. This chapter ends with introducing the concept of apparent barrier height in STM.

Chapter two gives a detailed description of the STM used in this project. The experimental procedure of preparing the Co/Cu(111) system is explained here.

In chapter three, we show the fabrication procedure of long copper chains with different widths on Cu(111). They were characterized and used as a perturbation to modify the quenched orbital momentum of Co adatoms. We used atom manipulation to build $\mathrm{Co}_n\mathrm{Cu}_m$ chains and investigate the magnetic behavior of single Co atoms. Afterward, the interaction between two Co atoms attached to different positions of Cu chains was studied. The obtained results show the energy barrier of the spin-flip process for Co atoms crucially depends on the hybridization of its $3d$ orbitals with the neighboring atoms. By attaching Co adatom to different positions of the chain, its spin-flip process was switched from an elastic to an inelastic process.

Chapter four reports measurements on the apparent tunneling barrier height (Φ_{app}) for the fabricated chains, vacancy lines (trenches), and deposited single Cu atoms. The unexpected trend of experimental Φ_{app} is interpreted as a kinetic-energy contribution in the tunneling process.

In chapter five the role of surface state electrons in Kondo effect of Co atoms on Cu(111) is investigated. We observed only a small and negligible dependence of the Kondo temperature to the variation of sample local density of states which shows that the measured Kondo resonance is mostly originated from the spin scattering of bulk conduction electrons with the Co localized spin.

Chapter 1

Fundamentals

In 1981, the invention of STM led to many possible experiments in surface science and nowadays it is a powerful instrument to investigate molecules and atoms on surfaces. This chapter starts with working principle of STM and STS. The theoretical background of mangeto-crystalline anisotropy and the Kondo effect will be addressed in sections (1.3), (1.4), and (1.5). The concept of local work function and apparent tunneling barrier height will be explained briefly at the end of this chapter.

1.1 Theory of Scanning Tunneling Microscopy

The basic model of tunneling phenomena in STM is a one-dimensional description where the vacuum is modeled by a potential barrier V_0 and tip and sample are the two electrodes at the left and right of this potential barrier. The states for $E < V_0$ are

$$\begin{cases} \psi_s(z) = e^{ikz} + ae^{-ikz} & z \leq 0 \\ \psi_b(z) = be^{\kappa z} + ce^{-\kappa z} & 0 \leq z \leq a \\ \phi_t(z) = de^{ikz} & z \geq a \end{cases} \tag{1.1}$$

with $k = \sqrt{2mE}/\hbar$ and $\kappa = \frac{\sqrt{2m(V_0-E)}}{\hbar}$ where m is the electron mass, $\hbar$ is Plank constant, and E is the electron energy at the Fermi level. These solutions describe the scattering of a plane wave e^{ikx} traveling in one direction and being partially transmitted through the potential barrier. κ is the decay constant and describes the attenuation strength of the wave functions of electrons with energy E through the barrier. For a high barrier, the barrier transmission coefficient (T) which is the ratio between the transmitted current density and the incident current density depends exponentially on the barrier width (a) and the square root of the effective barrier height ($\sqrt{V_0 - E}$)

$$T \propto e^{-2\kappa a}. \tag{1.2}$$

Since the wave functions are not zero in the barrier region and rather decrease exponentially, when the tip is brought close enough to a sample surface, there will be an overlap of the wave functions of the electrons in the tip and the sample. Therefore, the transmission probability of electrons to tunnel the potential barrier will be nonzero.

1.1.1 Bardeen's Approach

Bardeen modeled this one-dimensional potential barrier as three independent subsystems [8]. In his model, all the electron-electron interactions were ignored and the tunneling event was treated as a one-particle process. A single electron traveling through the barrier is described by the Hamiltonian

$$H = H_{sam} + H_{tip} + H_T \tag{1.3}$$

where H_{sam} and H_{tip} are the unperturbed sample and tip Hamiltonians as

$$H_{sam}\psi_s = -\frac{\hbar^2}{2m}\frac{d^2}{dz^2}\psi_s(z) + V_{sam}(z)\psi_s(z) \tag{1.4}$$

$$H_{tip}\phi_t = -\frac{\hbar^2}{2m}\frac{d^2}{dz^2}\phi_t(z) + V_{tip}(z)\phi_t(z) \tag{1.5}$$

and H_T is Bardeen's transfer Hamiltonian. The eigenfunctions of sample and tip Hamiltonians, ψ_s and ϕ_t, result from the above Schrödinger equations for two independent subsystems and are not an eigenfunction of the complete system. The state of combined tip and sample subsystems, ψ, can be expressed as a linear combination of their individual eigenfunctions (including their time evolution terms) as

$$\psi = a(t)\psi_s e^{-iE_s t/\hbar} + \sum_i^{\infty} c_i(t)\phi_t^i e^{-iE_t^i t/\hbar}. \tag{1.6}$$

In Bardeen's approach, time evolution is treated as a perturbation: at time $t \to -\infty$, the tip was out of the picture and the electron state was described only by the sample Hamiltonian. As time evolves, the tip is brought slowly towards the sample and the electron in sample experiences the potential of the tip in advance. This time-dependent potential can be expressed as

$$V_{tip}(t) = V_{tip}\ e^{\eta t/\hbar} \tag{1.7}$$

where V_{tip} is a constant and η is a small positive value. Before the perturbation has been added, $V_{tip}(-\infty)$ is zero, and at the end of perturbation when the tip is fixed close to sample, $\eta \rightarrow 0$ and $V_{tip}(t) = V_{tip}$. The time-dependent Schrödinger equation for the whole system is

$$i\hbar\frac{\partial\psi}{\partial t} = \bigg(- \frac{\hbar^2}{2m}\frac{\partial^2}{\partial z^2} + V_{sam} + V_{tip}(t)\bigg)\psi. \tag{1.8}$$

Inserting equations (1.6) and (1.7) into equation (1.8) results in

$$i\hbar\frac{dc_i(t)}{dt} = \left\langle \phi_t^i \left| V_{tip} \right| \psi_s \right\rangle\ e^{-i(E_s - E_t + i\eta)t/\hbar}. \tag{1.9}$$

$\left\langle \phi_t^i \left| V_{tip} \right| \psi_s \right\rangle$ is defined as the tunneling matrix element M, and describes how the transformer V_{tip} projects the initial state ψ_s into the final state ϕ_t.

Solving equation (1.9) will give us

$$c_i(t) = \frac{1}{E_s - E_t + i\eta}\ M\ e^{-i(E_s - E_t + i\eta)t/\hbar} \tag{1.10}$$

$\left|c_i(t)\right|^2$ which is the transition probability from ψ_s into ϕ_t is

$$\left|c_i(t)\right|^2 = \frac{e^{2\eta t/\hbar}}{(E_s - E_t)^2 + (\eta)^2}\ \left|M\right|^2 \tag{1.11}$$

. By calculating the time derivative of $\left|c_i(t)\right|^2$, we can obtain the rate at which an electron initially in the sample state ψ_s scatters into the tip state ϕ_t:

$$P(t) = \frac{d}{dt}\left|c_i(t)\right|^2 = \frac{2\eta}{(E_s - E_t)^2 + (\eta)^2}e^{2\eta t/\hbar}\frac{1}{\hbar}\left|M\right|^2. \tag{1.12}$$

Defining $\delta(x) = \frac{1}{\pi}lim_{\eta\rightarrow 0}\frac{\eta}{x^2+\eta^2}$, we can conclude that after the tip is stable and close to the sample or when the perturbation is off ($\eta \rightarrow 0$):

$$P(t) = \frac{2\pi}{\hbar}\delta(E_s - E_t)\left|M\right|^2. \tag{1.13}$$

As it can be seen, there is a nonzero rate only when the energy of electron does not change during the tunneling process, $E_t = E_s$ (elastic tunneling).

Multiplying electron transfer rate with the electric charge and sum over all the single-electron tunneling events results in the tunneling current formula.

However, since not all the states in the tip and the sample are vacant to scatter into, the occupation probabilities of them also need to be considered. Bardeen based his model on some assumption which amongst, he considered the occupation probabilities of the tip and the sample are independent of each other and they are in electrochemical equilibrium. Thus, their occupation probabilities follow the Fermi-Dirac distribution:

$$f_T(\epsilon) = \frac{1}{e^{\,\epsilon/k_BT} + 1} \tag{1.14}$$

where k_B and T are Boltzmann constant and temperature, respectively. Considering the fact that an electron can only tunnel from an occupied state of one electrode to the unoccupied state of the other electrode, the tunneling current from the sample to the tip is:

$$I_{s\to t} = \frac{4\pi e}{\hbar} \sum f(E_s - E_F^s)\big[1 - f(E_t - E_F^t)\big]\,|M|^2\,\delta(E_t - E_s - eV) \tag{1.15}$$

where E_F^s and E_F^t are the Fermi energies of the sample and the tip, respectively. The reverse interpretation for electrons scatter from occupied tip states to vacant sample states results in the tunneling current from the tip to the sample as:

$$I_{t\to s} = \frac{4\pi e}{\hbar} \sum f(E_t - E_F^t)\big[1 - f(E_s - E_F^s)\big]\,|M|^2\,\delta(E_t - E_s - eV) \tag{1.16}$$

The total tunneling current which is the difference between these two tunneling events is

$$I = \frac{4\pi e}{\hbar} \sum \big[f(E_s - E_F^s) - f(E_t - E_F^t)\big]\,|M|^2\,\delta(E_t - E_s - eV). \tag{1.17}$$

Finally, by replacing the sum with an integral and approximating the Fermi-Dirac distribution with a step function at low temperatures, the tunneling current will be simplified as

$$I = \frac{4\pi e}{\hbar} \int_0^{eV} \rho_s(E_F^s + E)\rho_t(E_F^t - eV + E)\,|M|^2 \tag{1.18}$$

where V is the bias voltage and ρ_s and ρ_t are the sample and the tip local densities of states (LDOS), respectively. In conclusion, it was shown that the tunneling current is mostly sensitive to the electronic structure of the sample and the tip.

1.1.2 Tersoff and Hamann STM Theory

Shortly after the invention of STM in 1981, Tersoff and Hamann used Bardeen's tunneling theory to calculate tunneling current as a function of sample and tip densities of states [9, 10]. They modeled the electronic structure of the tip with a spherically symmetric s-wave function $\phi_k \approx A_k e^{-\kappa_j r}/r$. The theory was made under the assumption of small bias voltages (lower than 10 mV) [10]. However, many STM measurements are conducted at much higher bias voltages.

To interpret such high bias voltage experiments, the Wentzel-Kramers-Brillouin (WKB) approximation is useful [9–14]. Within this approximation, the tunneling transmission probability T(z,E,eV) is given by

$$T(z,E,eV) = exp\left(\frac{-2z\sqrt{2m}}{\hbar}\sqrt{\frac{\phi_s+\phi_t}{2}+\frac{eV}{2}-E}\right) \tag{1.19}$$

where m is the electron mass, E is the electron energy with respect to the Fermi level, z is the tunneling barrier width, and ϕ_s and ϕ_s are the work functions of the sample and the tip, respectively. At T=0 K, the tunneling current can be written as [14, 15]:

$$I(z,V) \propto \int_0^{eV} \rho_s(E)\rho_t(E-eV)T(z,E,eV)dE \tag{1.20}$$

The tunneling electrons arise from the states within eV above the Fermi level of electrode with negative bias voltage polarity. The Tersoff-Hamann formula predicts that at low temperatures and low bias voltages STM measurements, the tunneling conductance (dI/dV) is proportional to the local density of sample states at the center of the tip at the Fermi energy.

1.1.3 Inelastic Tunneling

Electrons in STM can tunnel through the barrier in two ways: elastically or inelastically. In the elastic tunneling process, the energy of the tunneling electron is conserved, while in inelastic tunneling, due to the interaction of the electron with the environment, its energy changes. Earlier, we observed that the tunneling conductance is proportional to the sample and the tip density of states. Considering an atom with a vibrational or a spin excitation mode deposited on a substrate, the potential of the sample is $V_s + V_0\cos(\omega t)$. V_s is the potential of the sample while both adatom-related and tip-related perturbations are off [16]. The time-dependent term originates from for example vibrations of the adatom. V_0 is the amplitude and ω is the frequency of the vibration. Replacing the constant V_{sam} in equation (1.8) with its modified version, $V_s(t)$, we obtain

$$i\hbar\frac{dc_i(t)}{dt} = Me^{-i(E_s-E_t+i\eta)t/\hbar} + M_{in}cos(\omega t)\ e^{-i(E_s-E_t)t/\hbar}. \tag{1.21}$$

$M_{in} = \left\langle \phi_t^i \left| V_0 \right| \psi_s \right\rangle$ is the inelastic matrix element. Then, the rate of the inelastic tunneling probability is

$$P_{in}(t) = \frac{2\pi}{\hbar}\delta(E_s - E_t \pm \hbar\omega)\left|M_{in}\right|^2 \tag{1.22}$$

and total tunneling current is resulted from the both elastic and inelastic events.

1.2 Scanning Tunneling Spectroscopy

Scanning tunneling spectroscopy is an experimental method to probe the sample local density of states (LDOS). As seen from equation (1.20), the tunneling current is proportional to LDOS of the tip and the sample. Differentiating equation (1.20) gives

$$\begin{aligned}\frac{dI}{dV}(V) \quad \propto \quad & \rho_s(V)\rho_t(0)T(z,V,V) \\ & + \int_0^{eV} \rho_s(E)\frac{\rho_t(E-eV)}{dV}T(z,V,E)dE \\ & + \int_0^{eV} \rho_s(E)\rho_t(E-eV)\frac{T(z,V,E)}{dV}dE.\end{aligned} \tag{1.23}$$

Assuming a constant LDOS for the tip and a small variation of the tunneling transmission probability with the bias voltage, the last two terms can be neglected [17]. So the variations in the dI/dV signal can be assigned to the changes in the sample density of states. In practice, a small high-frequency sinusoidal modulation superimposed on a voltage ramp is applied to the sample. Then, the tunneling current is measured as a function of the voltage with a lock-in amplifier. The lock-in output gives information about the density of states as a function of energy.

1.2.1 Broadening in Scanning Tunneling Spectroscopy

dI/dV signals obtained from STS can be influenced by two broadening mechanisms: Thermal broadening and instrumental broadening [18]. So far, it was assumed that the tunneling current does not depend on the temperature. By assuming a constant tip density of states, the tunneling current will have the form

$$I(V) = C\int_{-\infty}^{+\infty} \rho_s(E)[f_t(E-V) - f_s(E)]dE \tag{1.24}$$

where C is a constant and $f_t(E)$ and $f_s(E)$ are the tip and the sample Fermi-Dirac distributions which depend on temperature as in equation (1.14). This temperature dependency leads to the broadening of the dI/dV signals and needs to be considered for the small spectroscopic features. Inserting $f_t(E)$ and $f_s(E)$ as equation (1.14) in (1.24) and derivating it results

$$\frac{dI}{dV}(V) = C\int_{-\infty}^{+\infty} \rho_s(E)\frac{\beta}{4[cosh(\beta(E-eV)/2)]^2}dE \propto \int_{-\infty}^{+\infty} \rho_s(E)\chi_{kT}(E-eV)dE \tag{1.25}$$

where $\beta = 1/k_B\mathrm{T}$ and χ_{kT} is the thermal broadening function as [18, 19]

$$\chi_{kT} = \frac{\beta}{4} cosh^{-2}(\beta(E - eV)/2) \tag{1.26}$$

The measured dI/dV ($\overline{\frac{dI}{dV}}$) is the convolution of the intrinsic dI/dV ($\frac{dI}{dV}$) with χ_{kT}

$$\overline{\frac{dI}{dV}} = \frac{dI}{dV} * \chi_{kT} \tag{1.27}$$

The thermal broadening can be estimated by $\Delta\mathrm{E_T} \approx 3.5\ k_B\mathrm{T}$ [20–22]. ΔE_T is the full-width at half-maximum of the thermal-broadening function. Experiments in the present work were conducted at temperatures around 4.4 K and 350 mK ($\Delta\mathrm{E_T} \approx 1.3$ meV and $\Delta\mathrm{E_T} \approx 0.1$ meV, respectively).

The second broadening mechanism is an instrumental effect from the lock-in amplifier. It can be calculated by the convolution of the intrinsic dI/dV spectrum with the lock-in broadening function $\chi_{Lock-in}$ as

$$\overline{\frac{dI}{dV}} = \frac{dI}{dV} * \chi_{Lock-in}. \tag{1.28}$$

where $\chi_{Lock-in}$ can be described as follow [18]

$$\chi_{Lock-in}(V) = \begin{cases} \frac{2\sqrt{{V_m}^2 - V^2}}{\pi {V_m}^2} & |V| < |V_m| \\ 0 & \text{otherwise} \end{cases} \tag{1.29}$$

V_m is the modulation voltage amplitude. In this work, Kondo effect (introduced in the next section) is the feature of interest which for Co atoms on Cu(111) occurs at ≈ 3.3 meV with respect to Fermi energy. Since most of the STS measurements were performed using 1 mV_{rms}, the broadening effects were considered in our data analysis.

Important parameters of the Kondo effect such as the resonance width were obtained using a fit function. In order to extract the not-broadened width or the intrinsic width of dI/dV signals, we applied the broadening effects to our fit function as follow:

1. First, the fit function, $F(V)$, was convolved with the two broadening functions χ_{kT} and $\chi_{Lock-in}$
$$\overline{F}(V) = F(V) * \chi_{kT} * \chi_{Lock-in}. \tag{1.30}$$
The result is a broadened fit function $\overline{F}(V)$.

2. Then, the measured dI/dV, $\overline{\frac{dI}{dV}}$, was fitted with the broadened fit function, $\overline{F}(V)$. With this method, we were able to extract the intrinsic width of our dI/dV signals.

1.2.2 Inelastic Tunneling Spectroscopy

The tunneling electrons can excite vibrational or magnetic modes of atoms and molecules on surfaces [2, 23–25]. These inelastic excitations open up additional tunneling channels which lead to a change in the differential conductance. There is a threshold voltage for which the tunneling current consists of only elastic electrons. When the voltage difference between the tip and the sample is larger than the excitation energy, the inelastic events also contribute to the tunneling process. The inelastic tunneling appears as steps in the differential conductance (dI/dV). These steps occur at defined voltages and are symmetric with respect to Fermi energy.

The experimental process of measuring these excitations is known as inelastic tunneling spectroscopy. In 1967, Scalapino and Marcus used WKB approximation to study the effect of inelastic tunneling in a planar junction [26]. In their model, the molecular dipole field was considered as an interaction potential perturbing the vacuum potential barrier height. A year after, another theoretical and experimental work was done by Lambe and Jaklevic to study the inelastic tunneling process in a metal junction with molecules [20]. According to these studies, the inelastic contribution to the tunneling current can be expressed as

$$\begin{aligned} I_{ine} = C \int_{-\infty}^{\infty} & \left[f(E - eV + \hbar\omega)(1 - f(E)) + f(E)(1 - f(E - eV - \hbar\omega)) \right] \\ & \times \rho_s(E)\ \rho_t(E - eV)\ T(E, eV)\ dE \end{aligned} \tag{1.31}$$

where C is a constant and $\hbar\omega$ is the energy the tunneling electron loose in the inelastic process.

Since then, many interesting experiments on molecules and single atoms were done by STM to study such excitations. In our project, we are interested in the magnetic excitation of single atoms attached to the fabricated nano-structures on a host metal.

1.3 Magnetism at the Atomic Scale

Understanding and being able to control magnetism on the atomic scale is the basic step to use it in the data storage technology. There are two important factors to design a stable atomic magnet: first, the magnetic anisotropy, which determines the direction and stability of the magnetic moment, and second, the size of the magnetic moment. The required energy to change the magnetic state to the opposite alignment is called the anisotropy barrier. Shrinking the size of data storage devices led to magnets at the atomic scale, and at such scales, quantum effects can significantly change the stability of the states. Thus, a detailed knowledge of magnetism at the atomic scale is required.

STM can be an excellent tool for probing the spin states of single atoms. It allows precise manipulation of the atoms surrounding environment and measuring the tunneling current through individual atoms. The technique in which inelastic tunneling spectroscopy is used to investigate the spin state of localized spins is called spin excitation spectroscopy (SES).

1.3.1 A Free Atom

A single atom can have a spin as a result of its partially-filled orbitals. Its total magnetic moment consists of orbital, $\vec{L}$, and spin, $\vec{S}$, angular momenta ($\vec{J} = \vec{L} + \vec{S}$). As long as the atom is in the gas phase and there is no external magnetic field, its spin can be oriented in any spatial direction.

When a particle with magnetic moment m is placed in a uniform external magnetic field, it feels a torque, which tends to align its magnetic moment parallel to the field. The energy associated with this torque is $H = -m \cdot \vec{B_{ext}}$, with $\vec{B_{ext}}$ as the external magnetic field. Treating the same effect for a single electron system (hydrogen atom) with the first-order perturbation theory ends up to an extra term in the total Hamiltonian as

$$H_z = \frac{e}{2m}(\vec{L} + 2\vec{S}) \cdot \vec{B}_{ext} \tag{1.32}$$

which leads to the shift and splitting of the energy levels. This effect is known as the Zeeman effect [27].

Moreover, by looking from the electron rest frame, the electron also experiences a second torque in the magnetic field originating from the orbiting proton. This interaction between $\vec{L}$ and $\vec{S}$ is called the spin-orbit coupling [27]. Using first-order perturbation theory for the single electron system gives the relation

$$H_{so} \propto \frac{1}{r^3}\, \vec{S} \cdot \vec{L}. \tag{1.33}$$

This electromagnetic interaction changes the energy spectrum of the atom and including H_{so} in the total Hamiltonian results the complete fine structure of the atom.

Despite the straightforward interpretation of this intrinsic interaction for a free particle, it becomes more complicated in solids and specifically in nano-structures with distinctive spatial geometries. The oriented chemical bonds fix the orbital momentum in a particular direction and the resulted energy increase in the system is equal to the energy difference between the favored and unfavored spin directions.

1.3.2 Magneto-Crystalline Anisotropy

When a free atom is located on a solid, its orbital angular momentum is affected by the spatial environment and aligns itself to a specific direction, accordingly. The crystal field, originating from the lattice potential can strongly reduce the orbital momentum. Therefore, the total magnetic moment depends mostly on the spin part [28, 29].

The magneto-crystalline anisotropy, MCA, is the result of the anisotropy of the atomic environment in solids. The difference in the spin-orbit energy (H_{so}), when the magnetization of the atom has been changed between two different crystallographic directions, namely "hard" and "easy" magnetization directions is called the magneto-crystalline anisotropy energy. The direction in which H_{so} is maximum is called hard axis and the one with minimum H_{so} is the easy axis. The idea of the spin-orbit interaction as the origin of MCA was first proposed by Vleck [30]. The magneto-crystalline anisotropy energy can be expressed as

$$\Delta E_{so} = \langle H_{so} \rangle_{hard} - \langle H_{so} \rangle_{easy} \approx \big(\langle L \cdot S \rangle_{hard} - \langle L \cdot S \rangle_{easy} \big) > 0. \tag{1.34}$$

In 1989, Bruno in his theoretical model derived the relation of this energy to the orbital momentum as [31, 32]

$$\Delta E_{so} \approx (m_o^{easy} - m_o^{hard}) > 0 \Rightarrow m_o^{easy} > m_o^{hard}. \tag{1.35}$$

It states that the spin-orbit coupling energy is approximately equal to the difference between the orbital momenta along the easy and the hard directions. Also, the orbital momentum is larger along the easy direction than the hard direction. Later, Néel suggested that due to the dangling bonds on the surface of the crystals, the orbital momentum is not completely quenched and a different magnetic anisotropy with respect to the bulk is expected [33].

1.4 The Total Spin System Hamiltonian

The first step to understand the experimental data is to define a proper Hamiltonian for the localized spin systems. The simplest method is to decompose the whole system into its subsystems:

$$H = H_t + H_s + H_a + H_i \tag{1.36}$$

where H_t and H_s are the tip and the sample Hamiltonians, H_a is the spin Hamiltonian representing the state of the spin system, and finally H_i is the interaction Hamiltonian which is responsible for the energy associated to the coupling of spins in the systems with more that one spin site [34].

The spin Hamiltonian is a simplified picture to interpret the measured spin state in STM experiments. It is used in many systems such as molecular magnets [5, 29, 35–38]. In the spin Hamiltonian, instead of using spin and orbital momenta individually, they are replaced by an effective spin momentum. This approximation is based on the orbital momentum quenching of the magnetic center.

A convenient procedure to construct the spin Hamiltonian (H_a) is to use g-factor to present the orbital momentum contribution in the total angular momentum. By definition, g-factor is the deviation of electron magnetic moment from the classical expectation [27]. In Dirac's theory, it is equal to 2. Introducing the orbital momentum as a deviation in the g-factor is a practical approach to only work with the spin momentum [39]. In this way, the experimentally obtained magnetic moment can be directly related to its spin part.

Using the Zeeman and the spin-orbit coupling terms as equations (1.32) and (1.33), the spin hamiltonian is

$$H_a = H_{so} + H_z = \lambda \vec{S} \cdot \vec{L} + (\vec{L} + 2\vec{S}) \cdot \vec{B}_{ext} \tag{1.37}$$

Both spin-orbit and Zeeman terms contain the orbital momentum, $\vec{L}$, and the goal is to transfer its effect in the g-factor. The effective spin Hamiltonian, H_{eff}, is a substitute for H_a which contains only the spin operators. Following the procedure in [39], by using the perturbation theory we can remove the orbital basis functions and the resulted first-order energy correction is

$$H_{eff}^{(1)} = \langle \Psi_0 \left| H_a \right| \Psi_0 \rangle = 2\mu_B \sum_{i=x,y,z} S_i B_i \tag{1.38}$$

with B_i as the applied magnetic field in direction i.

The second order energy correction is

$$H_{eff}^{(2)} = \sum_{i,j=x,y,z} \big[-2\lambda\mu_B B_i \Lambda_{ij} S_j - \lambda^2 S_i \Lambda_{ij} S_j - \mu_B^2 B_i \Lambda_{ij} B_j \big] \tag{1.39}$$

where

$$\Lambda_{ij} = \sum_n \frac{\langle \Psi_0 \left| L_i \right| \Psi_n \rangle \langle \Psi_n \left| L_j \right| \Psi_0 \rangle}{E_n - E_0} \tag{1.40}$$

and n represents the excited state number. Then, the total expression for the effective spin Hamiltonian will be

$$H_{eff} = H_{eff}^{(1)} + H_{eff}^{(2)} = \sum_{i=x,y,z} 2\mu_B (1 - \lambda\Lambda_{ii}) S_i B_i \; - \; \lambda^2 \sum_{i=x,y,z} \Lambda_{ii} S_i^2 \tag{1.41}$$

Interestingly, when the external magnetic field is zero ($B_i = 0$), there is still a non-zero value (the second term) in H_{eff}. This zero-field term can be expanded as

$$H_{zf} = -\lambda^2 \sum_{i=x,y,z} \Lambda_{ii} S_i^2 = -\lambda^2 \big(\Lambda_{xx} S_x^2 + \Lambda_{yy} S_y^2 + \Lambda_{zz} S_z^2 \big). \tag{1.42}$$

It is more common to write the zero-field term in the form of

$$H_{zf} = DS_z^2 + E(S_x^2 - S_y^2) \tag{1.43}$$

with

$$D = -\frac{\lambda^2}{2}(2\Lambda_{zz} - \Lambda_{xx} - \Lambda_{yy}) \tag{1.44}$$

and

$$E = -\frac{\lambda^2}{2}(\Lambda_{xx} - \Lambda_{yy}). \tag{1.45}$$

Finally, the effective spin Hamiltonian for a single spin system in the presence of an external magnetic field (we assumed the field is in the *z*-direction, perpendicular to the surface) can be expressed as

$$H_{eff} = -g\mu_B B_z S_z + DS_z^2 + E(S_x^2 - S_y^2). \tag{1.46}$$

For the physical interpretation, from the equations (1.44) and (1.45), D and E are both proportional to Λ_{ii} and according to the equation (1.40):

$$\Lambda_{ii} = \sum_n \frac{|\langle \Psi_0 \, |L_i| \, \Psi_n \rangle|^2}{E_n - E_0} \tag{1.47}$$

which represents the amount of orbital angular momentum projected in direction i ($i = x, y, z$).

The parameter D, named axial anisotropy, is the difference between the unquenched orbital angular momentum along *z*-direction and the sum of the unquenched orbital angular momenta along the other two in-plane x and y directions ($\Lambda_{zz} - (\Lambda_{xx} + \Lambda_{yy})$).

With the same interpretation, the parameter E, named transverse anisotropy, is the difference between the unquenched orbital angular momentum along x and y directions ($\Lambda_{xx} - \Lambda_{yy}$).

The axial component varies the gap between the energy levels with different spins. The transverse term is an anisotropy in the xy-plane.

1.4.1 Spin Correlation of Localized Spins and Surrounding Host Electrons

In spin excitation spectroscopy, the number of the conductance steps, their position, precise form and magnetic field dependence can give us important information about the magnetic states of the atomic system. They can appear as a result of magneto-crystalline anisotropy in the absence of any external magnetic field. The crystal asymmetry of the system and the spin-orbit coupling can cause this anisotropy, and as a result, the degenerate spin states can be split and lifted to non-degenerate states. The experimentally observed magnetic excitations vary up to tens of meV. However, not all the conductance steps are due to the magnetic excitations. There are low-energy mechanical vibrations that can result in a similar fingerprint in the spectroscopy. Therefore, to find out the source of such features in the spectrum, whether they are magnetic or vibrational excitations, an investigation them in the presence of an external magnetic field is a useful way.

When a magnetic atom is adsorbed on a surface, its interaction with the underlying atoms depends on the electronic properties of the substrate. A decoupling layer, such as Cu_2N, reduces interactions with the bulk electrons. For example, Co and CoH_x (x=1-3) complexes on graphene on top of a Pt(111) substrate showed a spin of 1 for Co and CoH_3 and a high magnetic anisotropy for the Co adatom [37].

Not only on top of decoupling layers, but also on bare metal substrates, spin excitations have been reported for magnetic adatoms in the absence of external magnetic fields. However, in such systems, the strong coupling of the localized spin with the conduction electrons of the host metal leads to the reduction of the spin lifetime. Spin excitations of Co and Fe adatoms on Pt(111) have been measured at $T \approx 6$ K and $T \approx 300$ mK [40, 41]. Fe adatoms showed spin excitations also on other metal surfaces namely Cu(111) [42] and Ag(111) [43]. Moreover, despite the strong localization of $4f$ wave functions to the nuclei and their small spatial dimensions, there are also traces of magnetic excitations for Gd atoms on Pt(111) and Cu(111) in their spectroscopy signals [44].

For the interpretation of such magnetic interactions, scattering models have been introduced and developed [45–48]. A straightforward model to interpret the exchange interactions between an isolated spin and tunneling electrons has been introduced by Markus Ternes [3]. His model covers the effect of magneto-crystalline anisotropy and considers the strength of coupling to the substrate. It is based on a simple scattering event: the tunneling electron scatters with the localized spin on the substrate. Two main parameters contribute in this scattering process; the potential scattering parameter U and the exchange scattering parameter J. The basic idea was introduced for the first time by Anderson [49]. His model was for a single impurity with a half-filled atomic orbital interacting with the host metal electrons. After that, Schrieffer and Wolf were able to define the scattering parameters more precisely as [50]:

$$J = \frac{2}{\pi}\Delta^2\left(\frac{1}{\epsilon_d} - \frac{1}{\epsilon_d + U_d}\right) \tag{1.48}$$

$$U = \frac{2}{\pi}\Delta^2\left(\frac{1}{\epsilon_d} + \frac{1}{\epsilon_d + U_d}\right) \tag{1.49}$$

where ϵ_d is the one-electron energy of the localized orbital with respect to Fermi energy, and U_d is the Coulomb repulsion between electrons of opposite spin in the d orbital. The negative sign of the scattering parameter J shows the anti-ferromagnetic coupling between the localized spin and the substrate electrons.

1.5 The Kondo Effect

The conduction electrons in metals act as weakly coupled quasi-particles. The theory of Fermi liquid developed by L. Landau provides a good description for the electric resistivity of normal metals containing impurities [51, 52]. It was shown that the electric resistivity of the metal drops when its temperature decreases and saturates at low temperatures due to static defects in the material. The electric resistivity can be expressed as

$$\rho = \rho_0 + \rho_{\textit{el-ph}} \tag{1.50}$$

where ρ_0 is the zero-temperature residual resistivity originated from the conduction electrons scattering with the nonmagnetic impurities and is temperature-independent. The second term arises from other types of scattering processes, mainly electron-phonon interaction [53]. It depends on temperature as [54]

$$\rho_{\textit{el-ph}} = \alpha_{\textit{el-ph}} \left(\frac{T}{\Theta_R} \right)^2 \int_0^{\Theta_R/T} \frac{x^n}{(e^x - 1)(1 - e^{-x})} dx \tag{1.51}$$

where $\alpha_{\textit{el-ph}} \propto \lambda_{tr} \omega_D / {\omega_p}^2$ with λ_{tr} the electron-phonon coupling constant, ω_D the Debye frequency, and ω_p the plasma frequency [55]. n is a constant which can be equal to 2, 3 or 5. For Cu, Ag, and Au, $n = 5$ [56]. Θ_R is the Debye temperature which for bulk Cu with $n = 5$, $\Theta_R \approx 300$ K [57]. Although the exact value of the low-temperature resistance depends mostly on the number of defects in the metal, the temperature characteristic remains the same. In this work we focus on metals with magnetic atoms.

1.5.1 Metals with Magnetic Impurities

The magnetic impurities in metals cause a drastic change in their low-temperature resistivity. Impurities such as Co, Fe, and Mn have partially filled outer d or f shells and may have a nonzero net magnetic moment. In 1937, Hildebrand discovered an interesting characteristic change in the electrical resistivity of these systems [58]. He observed an initial decrease in resistance with temperature reduction and an unexpected increase when further reduced the temperature leading to a resistivity minimum. This behavior was observed only when the metal contained magnetic impurities.

Another important experimental observation was the existence of the resistivity minimum for metals with an impurity concentration even less that 0.1%. The results showed the proportionality of the residual resistance to the impurity concentration. Regardless of the impurity concentration, the resistance increases as the temperature is lowered.

The origin of this phenomenon remained unclear until 1964 when it was explained by Jun Kondo [1]. He explained it via a scattering model. A scattering process with nonmagnetic impurities can be treated like a one-particle problem with a potential

$$\sum_i \upsilon(r - \boldsymbol{R_i}) \tag{1.52}$$

and each conduction electron scatters from the same, steady potential. But if the scatterer can change its state, by e.g. having a spin or orbital degree of freedom, then each scattering may change the state of the scatterer. In a such system, the spin of the magnetic impurities paired themselves with many conduction electrons of the bulk continuum. They can flip from up to down state, or vice versa, and a singlet ground state will be generated. This spin flip process is called Kondo effect. The Kondo resonance lies close to Fermi energy and the characteristic temperature around which the minimum resistivity occurs is called Kondo temperature, T_K.

To understand this spin flip process, the single-impurity model by Anderson simplifies the picture to a magnetic atom with one electron in its single d orbital [34, 49, 50]. When the magnetic atom is deposited on top of a metal surface, its half-filled d orbital (d^1) is located below the Fermi level at binding energy ϵ. Upon adding a second electron to this d-orbital and occupying it with opposite spins (d^2), its energy increases by the Coulomb repulsion energy, U. This situation is illustrated in figure 1.1(a). The spin flip process between the electron in the singly occupied d state and a conduction electron with an opposite spin forms the Kondo resonance. Flipping can either happen by emptying the d orbital ($d^1 \to d^0$) and then refilling it (path 2 in figure 1.1(b)) or by putting the second electron in the d orbital, making it doubly occupied ($d^1 \to d^2$) and then removing one electron (path 1 in figure 1.1(b)).

As a second electrode (probing tip) is brought close to the adatom and the substrate (figure 1.1(c)), the electrons from the tip can tunnel into the sample via three possible channels. Electrons can (1) tunnel into the empty states of the substrate, (2) tunnel into the Kondo resonance, or (3) tunnel indirectly into the localized state of the magnetic adatom. The first two spin-conserving paths have tunneling probabilities t_1 and t_2 in the tunneling matrix, and the tunneling current is proportional to the interference between these two channels ($q \propto t_2/t_1$).

STS measurements are used to detect the Kondo resonance of magnetic atoms. This resonance appears as a narrow dip or peak feature around zero energy. The line-shape of the

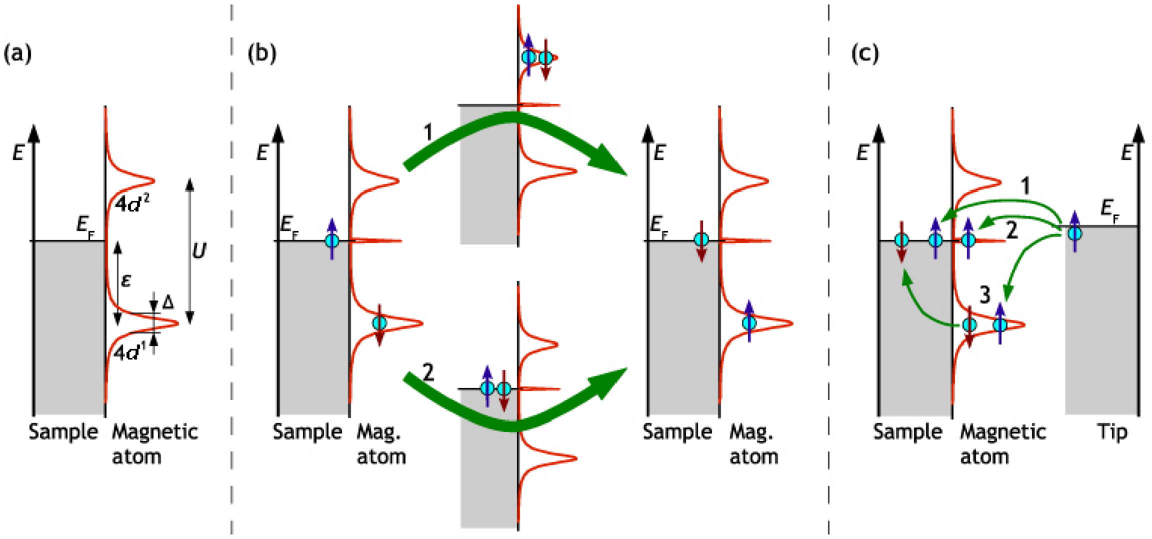

FIGURE 1.1: (a) Sketch of the energy-dependent DOS for a single d orbital on a metal surface. (b) Electron in d orbital can flip its spin with a bulk electron of opposite spin. The spin flip process can occur in two ways: d orbital of the adatom is filled with two electrons (process 1) or it is empty (process 2). Kondo resonance is generated close to the Fermi energy through this process. (c) Tunneling process from the probing tip to the metal. Adapted from Ref [34].

resonance crucially depends on the lateral distance between the tip apex and the impurity [59]. Lateral movement of the tip from the impurity's top position decreases tunneling probability of electrons to the adatom (they will tunnel more to the empty states of the bulk). The symmetric line-shape of the resonance changes to an asymmetric line-shape [59]. Important quantitative information such as the width and the energy position of the Kondo resonance can be obtained from its line-shape in the dI/dV measurement. The Kondo temperature is proportional to the half-width at half-maximum (HWHM) of the resonance, Γ, as [34]

$$T_K \propto \frac{\Gamma}{k_B} \approx \Gamma \times 11.6\ \mathrm{KmeV}^{-1} \tag{1.53}$$

In order to extract the resonance HWHM, different fits namely Fano and Frota were proposed and used. Fano described the interference of the tunneling channels with the Fano equation [60]

$$Fano(V) \propto \frac{(q+\epsilon)^2}{1+\epsilon^2} \tag{1.54}$$

with $\epsilon = (eV - E_K)/\Gamma_{Fano}$, V as the sample voltage, and q as the asymmetry parameter which defines the resonance line-shape. It depends on the ratio of the direct and the indirect tunneling process at the energy E_K [61].

Years later, for the simulation of the Kondo resonance, a different line-shape was introduced

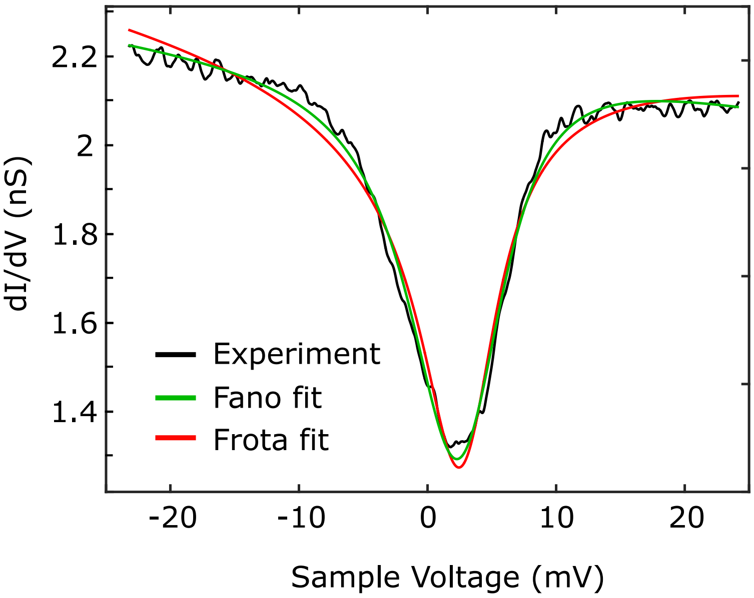

FIGURE 1.2: Kondo resonance of Co adatom on Cu(111) measured with $V_{mod} = 1$ mV$_{rms}$ at T = 4.6 K fitted by Fano and Frota functions. Fano fit reproduces the Kondo resonance more accurately. The current feedback was opened at V = 250 mV and I = 440 pA.

by Frota which has the functional form as [62–64]

$$\frac{\Delta dI}{dV} = A\ Im\left[ie^{i\Phi}\sqrt{\frac{i\Gamma_{Frota}}{eV - e_k + i\Gamma_{Frota}}}\right] + BV + C. \tag{1.55}$$

The Frota parameter Γ_{Frota} is related to the actual HWHM of the resonance by HWHM $\sim 2.54\ \Gamma_{Frota}$. e_k is the position of the resonance and A is its amplitude.

Depending on the used voltage range and the system under investigation, one of these fits matches the data better [18]. We applied both Fano and Frota fits to the measured resonances of more than 20 adatoms. A single resonance of Co on Cu(111) with its Fano and Frota fits are shown in figure 1.2. Although the theory and some experiments showed a better agreement of Frota line-shape with the experimental resonance, we observed Fano fit reproduces the resonance of Co on Cu(111) with a better precision. This disagreement might be an indication of an alternative origin of this zero bias anomaly as proposed by L. Samir very recently [65].

1.5.2 Kondo Effect of Co Atoms

Co adatoms on different noble metal surfaces were reported to be Kondo systems, and have been studied to a good extent with STM. Studies on single Co atoms on Ag(100), Ag(111), one monolayer of Ag on Cu(111), and on Cu(111) reveal different positions of the resonance minimum and different Kondo temperatures [66, 67]. The dependence of the Kondo temperature on the supporting host metal triggered the idea of tuning the Kondo resonance by manipulating the impurities neighbor atoms which led to interesting experiments over the past years. CoCu_n clusters were fabricated by atom manipulation on Cu(111) and the evolution of the Kondo resonance with respect to the number of neighboring Cu atoms were investigated in [68]. It was observed that the Kondo effect of Co atoms crucially depends on the detailed geometric structure of its environment.

The simplest system to study the non-local correlations for distant atoms is two deposited magnetic adatoms. In an experiment done by Néel et al., the interaction between two Co atoms was studied [69]. He built chains of copper atoms with lengths up to four atoms and added two Co atoms to the ends of the chain. He observed an oscillatory behavior of the Kondo resonance width for chains with more than three Cu atoms. This observation was interpreted as non-local correlation between magnetic sites induced by the Cu atoms of the chain. His measurement arose interesting questions regarding the position and the length of the prepared chains: What could be expected when Co atoms are attached from the side to the chain? And is it possible to measure this correlation on long Cu chains?

Exploring the answers of these questions was the main goal of my PhD project.

1.6 Work Function and Apparent Tunneling Barrier Height

The work function is in principle the energy difference between a neutral crystal and the same crystal with one electron removed. It is the minimum energy required to move one electron from a metal to infinity [70, 71]. It can be written as the potential difference between Fermi energy of the metal and the vacuum potential:

$$W = V_e - E_F. \tag{1.56}$$

Since the potential difference between the metal and vacuum depends on the charge distribution at the surface, the work function varies for different crystallographic arrangement of the surface atoms. Taking an electron from more densely-packed surfaces requires more energy. This phenomenon is known as the anisotropy of the work function and creates the concept of local work function [72].

Another important concept arising from the image potential contribution is the apparent barrier height. When an electron is placed close to a metal surface, a polarization charge is generated on the surface. The effect of this polarization charge is equivalent to the presence of a positive image charge inside the metal. The image charge is at the same distance from the surface as the original charge from the surface. Due to the attractive force between the charge and the image charge, an image potential is generated close to the surface. This image potential decreases with increasing the distance from the surface and vanishes at infinity.

Due to the small gap between the tip and the sample in STM, the image charge contribution to the tunneling gap potential needs to be considered. The potential barrier a tunneling electron has to overcome in STM is called apparent barrier height.

1.6.1 Barrier Height Spectroscopy

In tunneling spectroscopy, the tunneling current is recorded as a function of the applied voltage. The height and the width of the tunneling barrier are two unknown quantities that influence the transmission probability of the tunneling electron. Another spectroscopy mode is measuring the tunneling current as a function of the tip-sample separation at a constant applied voltage. It is called barrier height spectroscopy or IZ spectroscopy.

At low bias voltages, the tunneling transmission probability equation (1.19) can be simplified as

$$T(z) = exp\left(\frac{-2z\sqrt{2m}}{\hbar}\sqrt{\frac{\phi_s + \phi_t}{2}}\right). \tag{1.57}$$

If we assume DOS contributions to the tunneling current do not change with the tip-sample separation, then $I(z) \propto T(z)$ and

$$\frac{d\ lnI}{dz} = \frac{1}{I}\frac{dI}{dz} = \frac{2\sqrt{2m}}{\hbar}\sqrt{\frac{\phi_s + \phi_t}{2}} \Rightarrow \frac{d\ lnI}{dz} = \frac{2\sqrt{2m\Phi_{app}}}{\hbar} \tag{1.58}$$

with

$$\Phi_{app} = \frac{\phi_s + \phi_t}{2}. \tag{1.59}$$

By applying a small modulation to the z-piezo of the tip and measuring the resulting modulation in the tunneling current (dI/dz), the average work function of the sample and the tip can be determined. Then the apparent barrier height can be extracted as

$$\Phi_{app}\ [\mathrm{eV}] = \frac{\hbar^2}{8m}\left(\frac{d\ lnI}{dz}\right)^2 = 0.952\left(\frac{d\ lnI}{dz[\mathrm{Å}]}\right)^2. \tag{1.60}$$

If the atomic structure of the tip does not change during the measurement process, any change in the measured apparent barrier height can be related to the local sample work function.

Chapter 2

Experimental Setup

The goal of this work was to prepare long atomic chains on surfaces and use them to investigate the evolution of the Kondo resonance of magnetic atoms in different electronic environments. In this section, the instruments and the experimental procedure of preparing the sample and the tip are explained.

2.1 Low-Temperature STMs

The first part of the experiments presented in this thesis were conducted using a home-built scanning tunneling microscope operated at 4.5 K in ultrahigh vacuum (UHV). The UHV system consists of three vacuum chambers separated from each other by gate valves. A load-lock chamber provides the capability of inserting samples and tips from ambient to low pressure environment without venting the complete vacuum system. Samples can be cleaned in a preparation chamber (base pressure 1×10^{-10} mbar) by heating via electron bombardment (annealing) and sputtering cycles. Sputtering can be done through a leak valve in the preparation chamber from which noble-gas ions can be directed to the sample surface via an ion gun. Moreover, the preparation chamber was equipped with an electron-beam evaporator, an evaporation station, and a mass spectrometer. The evaporation rates of molecules from a Knudsen cell can be monitored by a quartz balance. A rotatable manipulator is used to align the sample surface to the sputter ion source or the evaporation station.

All the analysis were done in the analysis chamber. After preparation cycles, sample and tip were transferred into the microscope stage. A bath cryostat is mounted on the microscope chamber with a capacity of four liters of liquid helium and fifteen liters of liquid nitrogen. The whole machine can be lifted by a pneumatic damping system. The base plate

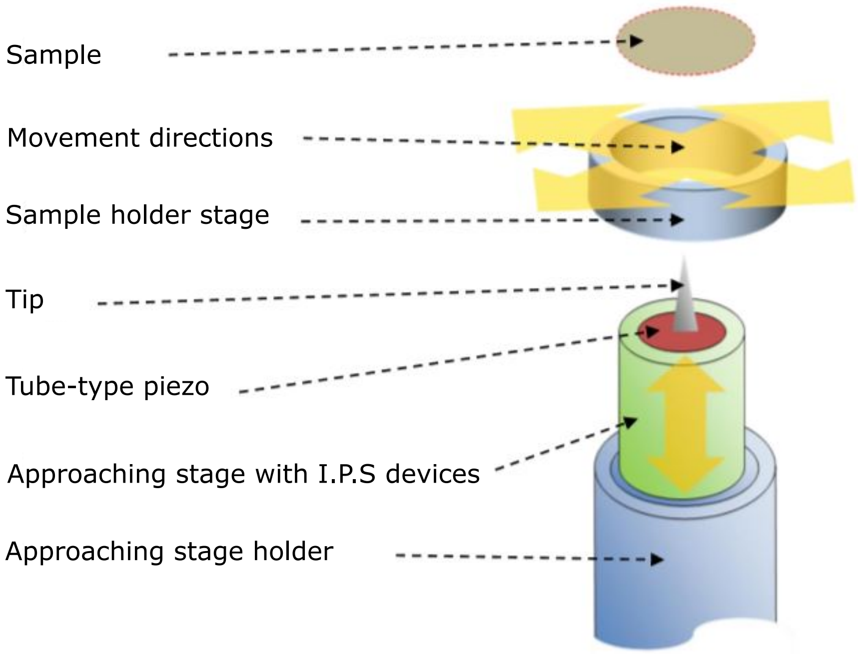

FIGURE 2.1: Scanning tube-type piezo driver in mK STM machine [74].

of the STM stage was vibration isolated via three springs. A more detailed description of the STM stage design is described in [73]. A SPM1000 electronic from *RHK Technology* is used to control the STM. The tunneling current amplification is done by a DLPCA-200 transimpedance amplifier from *FEMTO Messtechnik GmbH*. Differential conductance dI/dV is recorded using a SR830 Lock-In amplifier from *Stanford Research Systems* while a sinusoidal modulation is added to the sample voltage.

In this project, we conducted further measurements with a STM equipped with superconductive magnets operating at a base temperature of 350 mK. The refrigerator of the USM1300-He-3 is able to cool the sample down to 350 mK with He3. The superconductive magnets can provide magnetic field up to 9 T in out-of-plane direction (Z) and 2 T in in-plane directions (X and Y). A single tube piezo located in an approach stage and driven by 6 piezo stacks is used for the scanning process. For measurements, the approaching stage is approximately 5 mm away from the crystal in z direction and the sample stage can move 0.5 mm in X and Y directions. The directions are shown in Figure 2.1.

An overview of the chamber components in mK STM is illustrated in figure 2.2. STM stage is placed in an insert chamber which consists of a long stainless steel cylindrical chamber and a Cu cylinder. The insert chamber is thermally isolated by a vacuum chamber which is called Thermal-isolation chamber (TIC). During the pre-cooling process, the exchange gas (e.g. He) was introduced into TIC for enhancing the cooling progress. For that purpose, the magnets were cooled down to 77 K by liquid nitrogen (LN2). Then, the LN2 was replaced with liquid helium (LHe) to cool the sample down to 4.2 K. LHe was vaporized by reducing

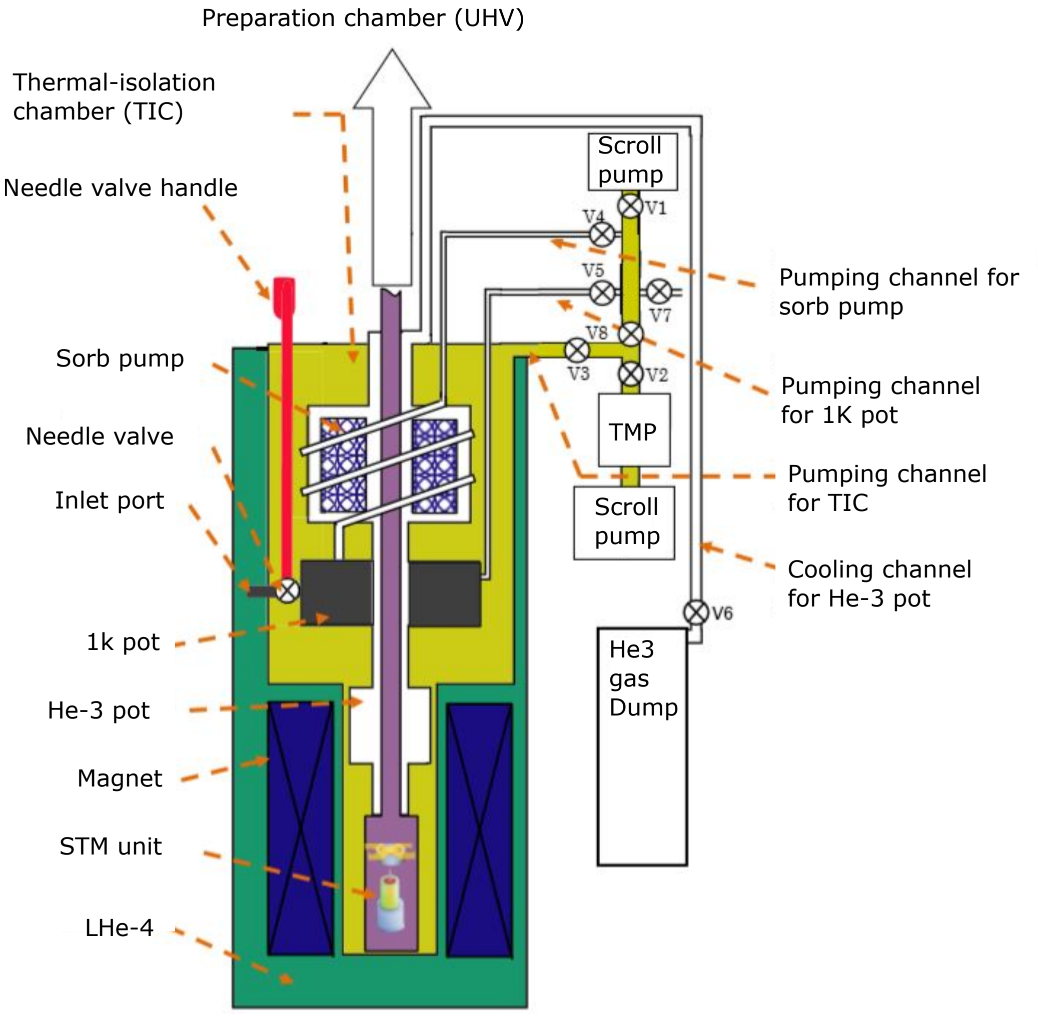

FIGURE 2.2: The overview of insert chamber components in mK STM machine [74].

the pressure of the 1 K pot which cooled down the sample to approximately 1.5 K. After a short temperature stabilization time, He-3 gas was introduced into the He-3 pot. By using the 1 K pot to reduce the temperature of He-3 pot to approximately 2 K, He-3 is liquidized. Finally, the liquid He-3 in the He-3 pot was vaporized using the sorb pump which enabled to cool the sample down to 350 mK.

In this thesis, STM imaging was acquired in constant current mode. The bias voltage is referenced to the sample electrode and the tip is virtually grounded. All topographs were processed using WSxM [75].

2.2 Tip and Sample Preparation

To conduct a reliable surface experiment, the first step is to reach a contaminant-free surface. This means large and atomically flat terraces free of residual impurities. The sample and the tip preparation was carried out in the preparation chamber. During the preparation cycles, due to the inlet of Argon ion gas and also removal of contaminants from tip and sample, the pressure of the chamber rose up to approximately 1×10^{-6} mbar. STM tips were electrochemically etched from tungsten wire, cleaned by short cycles of annealing, and further prepared in-situ by gentle tip-sample contacts. The Cu(111) single crystal was prepared by repeated cycles of Ar^+-ion sputtering and subsequent annealing. The ion-beam with the energy of 1 keV resulted in $\approx 20\ \mu$A ion current at the sample. The number of cycles depends on whether the crystal was exposed to the air or not. If it was kept in UHV environment, three to four sputtering cycles with duration of 20 minutes would result in a sufficiently clean surface.

To smooth the rough morphology of the surface caused by Argon ion bombardment, and to produce large atomically flat terraces, each sputtering cycle was followed by an annealing cycle. For this, a tungsten filament was placed close to the sample and thermionic-emitted electrons were accelerated to the sample. With filament current of 3 A, sample current of 7.5 mA and voltage of 1 kV, the crystal temperature rose up to $\approx$ 700 K for 30 minutes in each cycle. In the sample preparation process in mK STM, we also used electron bombardment for annealing. Here, one filament was placed on the sample holder. The sample holder had three connections; two for applying the current for the filament and one for providing the high voltage for the sample. The prepared sample and tip were transferred to analysis chamber.

2.3 Cobalt Evaporation

While layer growth of molecules and atoms can be done in the preparation chamber, single atom depositions have to be performed on the cold sample to prevent thermal diffusion. The design of 4 K STM allowed us to evaporate single Co atoms on the cold sample in analysis chamber via an electron beam evaporator. A high positive voltage ($V_E = 1$ kV) was applied to the evaporant which was in the form of a rod. Emitted electrons from a tungsten filament were accelerated to the cobalt rod and heated it. Evaporated Co atoms were ionized by an electron beam and their flux was monitored by an electrode outside of the evaporator. Thermionic emission current, I_{em}, was used as a parameter to reach the desired flux. Before the deposition, to remove contamination of the Co rod, we out-gassed it for several hours by slowly increasing the emission current to reach a flux slightly higher than the desired value and decreasing it after a while to reach a stable flux. $I_{em} \approx 12$ mA, $I_{flux} \approx 3.8$ nA and $V_E = 1$ kV were adjusted. Evaporation duration was 12 seconds.

Depositing single Co atoms with mK STM was more challenging. As shown in figure 2.1, the tip and the sample are positioned vertically leaving us two options for evaporation.

The first option was moving the sample out of the cryostat to the exchange chamber as fast as possible and after a short time of evaporation, inserting it back down into the STM stage. We observed that the transfer was not fast enough to avoid thermal diffusion; the temperature of STM stage rose up to ≈ 30 K, and all Co atoms moved to step edges and formed clusters. We concluded that the Co atoms need to be evaporated from the exchange chamber through the long stainless steel cylindrical chamber (length ≈ 1 m and diameter ≈ 5 cm) down on the crystal surface. Evaporation from the top was also not possible with the initial design of STM stage because the surface of the crystal was faced down. Therefore, we redesigned the tip holder and the sample holder and switched their positions. In this way, we were able to evaporate from the top on the cold sample. To make the crystal surface available for the evaporation, the tip needed to be transferred up to the exchange chamber (room temperature) and inserted again after the evaporation was finished. Introducing the tip close to the sample increased its temperature. To avoid this temperature rise, we pre-cooled the tip for 30 minutes on the 1K pot and He-3 pot before re-inserting it in the STM stage. Finally, after numerous attempts we were able to obtain single atoms with the mK STM machine.

2.4 Results and Discussion

A STM constant current topograph of the prepared Cu(111) surface prior to the Co evaporation is shown in Figure 2.3(a). From the cross-section of the topograph, the step height of 208 pm was extracted which was in agreement to the previously reported value [76]. Moreover, STS measurement done on a terrace showed the surface state of the Cu(111) at ≈ -430 mV (figure 2.3(c)).

Upon deposition of cobalt on Cu(111), isolated atoms with the apparent height of ≈ 60 pm were observed (Figure 2.4). Depending on the shape of the tip (blunt or sharp) their height had ≈ ±10 pm tolerance. There are two possible adsorption sites for the evaporated Co atoms on Cu(111) surface: fcc site and hcp site. The fcc site is more energetically favored over the hcp site for Co adsorption because there is no Cu atom in the lower layer. In the absence of the tip, the calculated energy barrier for Co adatom to hop from fcc to the nearest hcp site is approximately 37 meV [77]. Bringing the tip close to the surface affects the potential profile of the environment. Positioning the tip above either hcp or fcc site at tip-surface separations lower than 4.1 Å reduces the energy barrier between the sites and make it possible for Co atom to hop to its nearest adsorption sites [77]. For that reason, we observed unstable and mobile Co atoms even during normal surface scanning. To avoid that, one has to minimize tip-sample interaction by adjusting the tip sufficiently far from the sample.

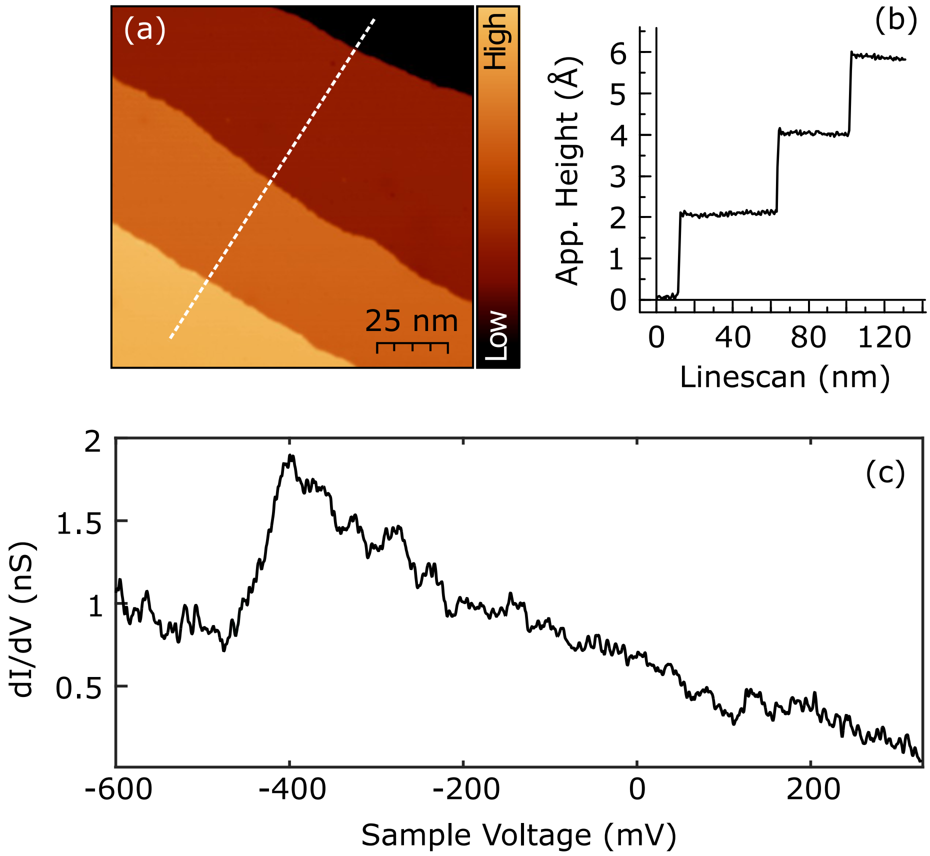

FIGURE 2.3: (a) Constant current STM image of prepared Cu(111) with steps acquired at V = 100 mV and I = 36 pA (124.7 nm×124.7 nm). (b) The height profile along the dashed line in (a). It shows the step height of ≈ 200 pm. (c) STS data obtained on a Cu(111) flat terrace with its surface state at $V \approx -430$ mV. Current feedback was opened at V = 600 mV and I = 320 pA.

To investigate the electric properties of the deposited adatoms, differential conductance spectra were measured. Figure 2.5 shows typical spectra acquired atop the Co adatoms. They all exhibited a narrow resonance close to the Fermi energy with offset of ≈ 3.3 meV [34]. This shift to slightly positive values remains an unsolved puzzle, as the Kondo resonance should be centered at slightly negative values for more than half-filled orbitals [78]. In March 2020, an alternative interpretation for the observed zero bias anomalies of Co adatoms on Cu(111) was proposed which was calculated to be at positive voltages and could also be the reason for the disagreement between the measured resonances and Frota line-shapes [65]. However, as this is still an ongoing discussion in the surface science community, we will term the observed spectroscopic feature a Kondo resonance throughout this thesis.

The observed small differences in the slope, strength and line-shape of the spectra may resulted from different phenomena. In figure 2.5(a), we measured the Kondo resonance of Co adatom at different positions on a large terrace (black lines). Measurements were also done at the same positions on surface in the absence of the Co atoms (blue lines). As shown, the

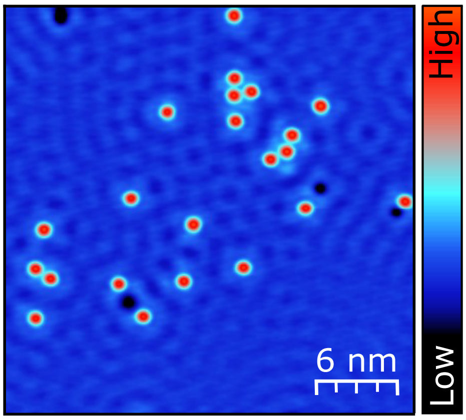

FIGURE 2.4: STM image of evaporated Co adatoms with apparent height of ≈ 60 pm on Cu(111) substrate. The image was acquired at V = 30 mV and I = 30 pA.

Kondo resonances have the same slope as the spectra obtained on the bare surface. This indicates that the slope is mainly originated from the surface LDOS variations.

Also, it was reported that the resonance line-shape depends on the ratio between the probability of tunneling into the Kondo resonance and the probability of tunneling directly into the empty states of the host metal [34]. The lateral position of the tip affects this ratio. Experiments showed when the tip is positioned directly above the Co atom, the Kondo resonance has its maximum amplitude and there is an overshoot in the line-shape at positive energies. Small lateral displacements of the tip from the topmost position of the adatom weakens the strength of the Kondo resonance and the resonance dies off over a lateral length scale of ∼ 10 Å[59].

In addition to different background slopes for the Kondo resonances, in some cases we also observed small overshoot in the line-shape at positive energies. We interpreted the different line-shapes of our Kondo resonances as the variations in the surface LDOS and the lateral position of the tip with respect to the adatom. To assure the measurement process has not changed the tip, before and after every STS measurement on Co atoms, a spectrum was acquired on the bare Cu(111) terrace.

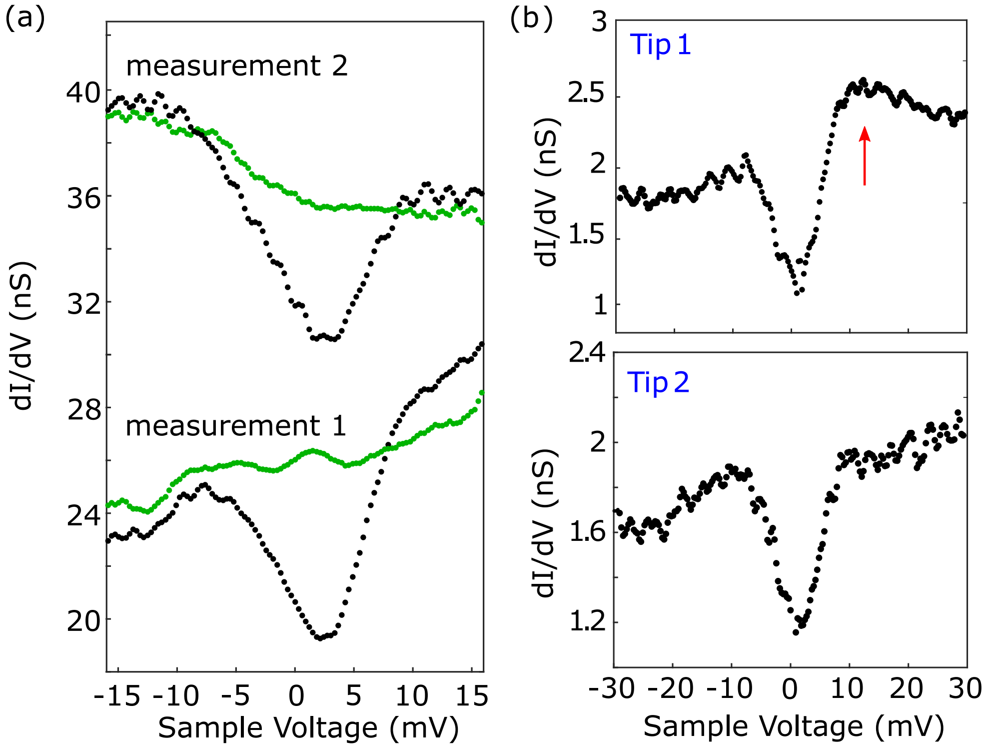

FIGURE 2.5: (a) Two measurements representing the Kondo resonances of two Co adatoms on different positions of a large Cu(111) terrace (black lines) and spectra at the same position of the surface in the absence of Co adatoms (green lines). The Kondo resonances show the similar background slopes as their corresponding spectra on the bare surface. Current feedback was opened at V = 20 mV and I = 500 pA. The spectra of measurement 2 are offset by 10 nS for clarity. Same tip was used for both measurements. The surface spectra are subjected to low-pass FFT-filtering for noise removal. (b) Kondo resonances of two Co adatoms measured with two different tips. The small overshoot of the resonance obtained with Tip 1 (red arrow) is interpreted as the higher tunneling probability of the electrons from the tip into the Kondo resonance.

Chapter 3

Kondo Effect of Co Atoms at Long Cu Chains

In this chapter the unique part of this project will be described: fabrication of long atomic chains and investigating the Kondo resonance of cobalt atoms attached to these chains. Firstly, the fabrication procedure of atomic chains on Cu(111), their characterization, and manipulation of cobalt atoms to build $\mathrm{Co}_n\mathrm{Cu}_m$ are explained. Secondly, the results of STS measurements on cobalt atoms at different positions of the chain in the absence and the presence of an external magnetic field are showed and analyzed.

3.1 Copper Chain Fabrication

The Cu(111) surface is formed by a hexagonal arrangement of atoms with lattice constant of 2.54 Å. An external force can induce shear motion and change the material geometry. Depending on the type of lattice, different slip systems exist in the materials. A dislocation is a boundary between the slipped and the unslipped parts of the crystal lying over a slip plane [79]. Slip in fcc crystals occurs along the close-packed plane and close-packed directions, because they have the most number of atoms per area (or per length) and the energy required to move them is minimum. Long chains of Cu atoms were fabricated following the procedure of Sperl et al. [80]. Dipping of the STM tip into the crystal surface leads to the formation of different kinds of dislocations. Figures 3.1(a,b) illustrate the indention area and the produced dislocations close to the indention area. One of the most observed dislocations was screw dislocation (shown in figure 3.1(b)). Among different kinds of dislocations, we also observed straight and long (lengths up to 200 nm) atomic chains of various widths (figure 3.1(c)). These atomic structures can be used to investigate the evolution of

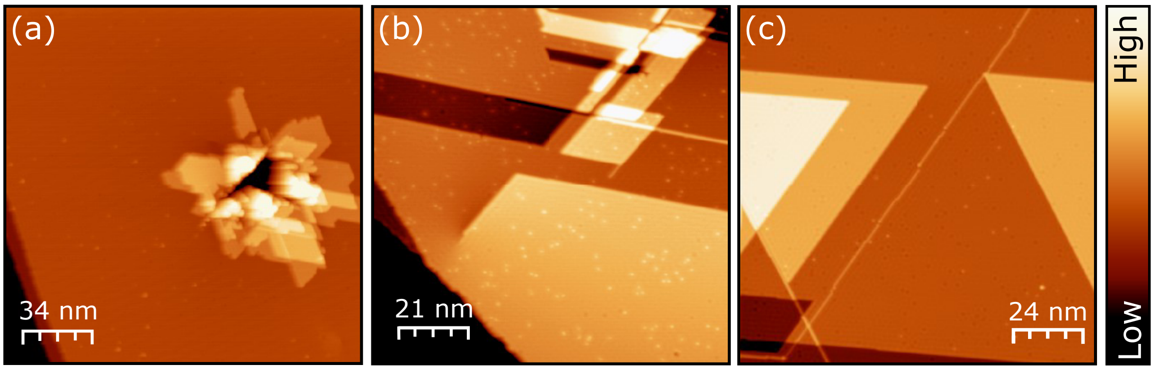

FIGURE 3.1: Constant current images of (a) the tip indention area, (b) generated dislocations close to the indention area, and (c) fabricated long (up to 200 nm) copper chains on Cu(111).

the Kondo effect and also to study the spin interaction between magnetic atoms.
To characterize these atomic chains, dI/dV measurements were performed on top of them. Figure 3.2(b) shows the result of STS measurements along a line perpendicular to a monatomic chain. By getting close to the chain, the Cu(111) surface state gets weaker and a state at $\approx$ 1.5 V appears. Using atom manipulation Fölsch et al. showed long Cu chains on Cu(111) exhibit an unoccupied state at 1.5 eV above Fermi energy [81]. In addition to the cross-section in topographs, we used this state to discriminate chains of single-atom width from wider chains. The apparent height of monatomic chain is approximately 100 pm.

Besides monatomic chains, we also observed chains with two or three atoms in width.

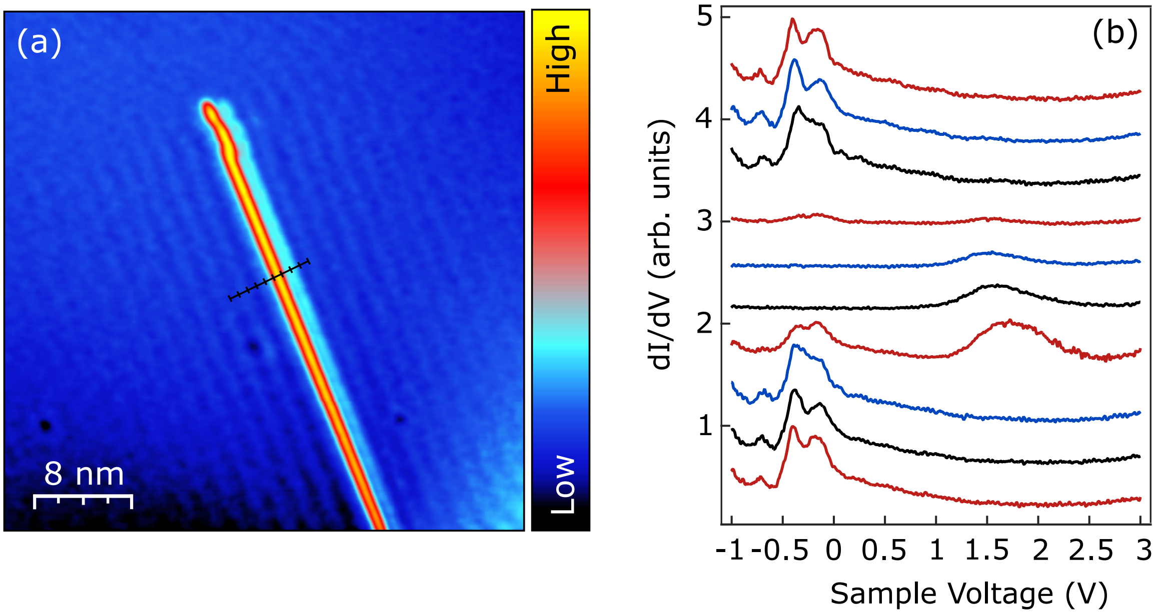

FIGURE 3.2: (a) Constant current image (41.1 nm×41.1 nm) of a monatomic Cu chain on Cu(111) (V = 50 mV, I = 42 pA). (b) dI/dV spectra along a line perpendicular to the chain. Current feedback was opened at V = 3 V and I = 1.27 nA.

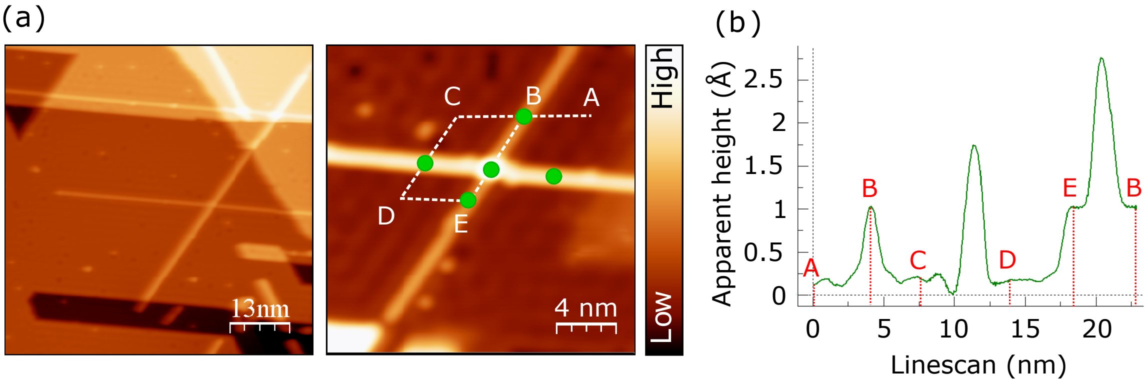

FIGURE 3.3: (a) Constant current image of two crossing chains with different widths on Cu(111) surface (left topograph: 65 nm×65 nm, V = 100 mV, I = 50 pA. Right topograph: 19.3 nm×19.3 nm, V = 60 mV, I = 47 pA). Green dots represent the STS measurement positions shown in figure 3.4. (b) Height profile along the white dashed-line in the right topograph. The two-atom wide chain has ≈ 175 pm apparent height and the crossing point has the apparent height of ≈ 275 pm.

Figure 3.3 shows two crossing chains with different widths. According to the height profile along the white contour, the two-atom wide chain has ≈ 175 pm apparent height and the crossing point has the maximum height of ≈ 275 pm in this structure. The dI/dV measurements on three different positions of the crossing structure, namely the monatomic chain, the wide chain, and the crossing point are shown in figure 3.4. Each dI/dV spectrum in figure 3.4 is the average of two measurements which were performed at different positions of the same chain (shown by green dots in figure 3.3(a)). We observed that for the two-atom wide chain the unoccupied state at ≈ 1.5 V decreases in intensity and shifts

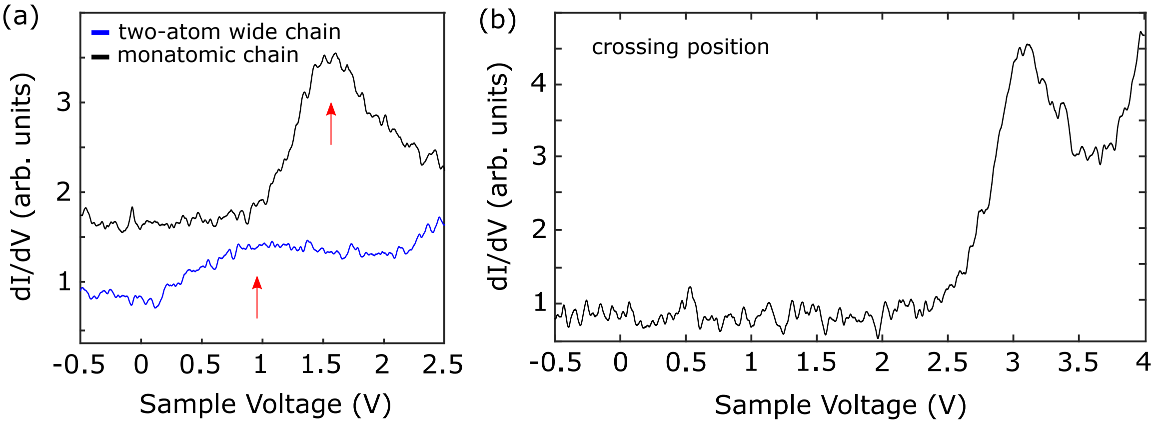

FIGURE 3.4: STS data obtained on different positions of the structure shown in figure 3.3, namely on (a) the monatomic chain, the two-atom wide chain, and (b) the crossing position (measurement positions are shown as green dots in figure 3.3(a) right topograph). For the two-atom wide chain, the unoccupied state of the monatomic chain at ≈ 1.5 eV decreases in intensity and shifts downwards in energy (shown by red arrows). A sharp state at ≈ 3 eV was also observed for the crossing position. Current feedback was opened at V = 2.5 V and I = 800 pA for the monatomic and the two-atom wide chain and at V = 4 V and I = 800 pA for the measurement on the crossing position.

downwards in energy (shown by red arrows). The crossing point showed a constant LDOS up to ≈ 2.5 V and by further increase of energy, we observed an unoccupied state at ≈ 3 V interestingly similar to the data of Cu adatom on Cu(111) [81]. These results correspond to a confinement of the 2D surface state to one (chains) and zero (crossing point) dimensions, respectively.

3.2 Atom Manipulation and Co_nCu_m Chains

To move a cobalt atom, the tip was brought close to it. The adatom was trapped in the highly localized potential well under the tip. Moving the tip laterally while maintaining constant current kept the adatom trapped in the potential well. Finally the adatom can be released at the destination by increasing the junction resistance to values used in normal imaging.

For atom manipulation, we used a reduced tunneling resistance (V = 30 mV, I = 1 μA) and moved the Co atoms to either side of the chain and at one of its ends. Figure 3.5 and figure 3.6 show topographs of the manipulation process where Co atoms were attached to the side and the end of a monatomic chain, respectively.

Before investigating the effect of the second Co atom attachment to the Kondo resonance of the first Co at the chain, we started our study by the basic measurement: the Kondo

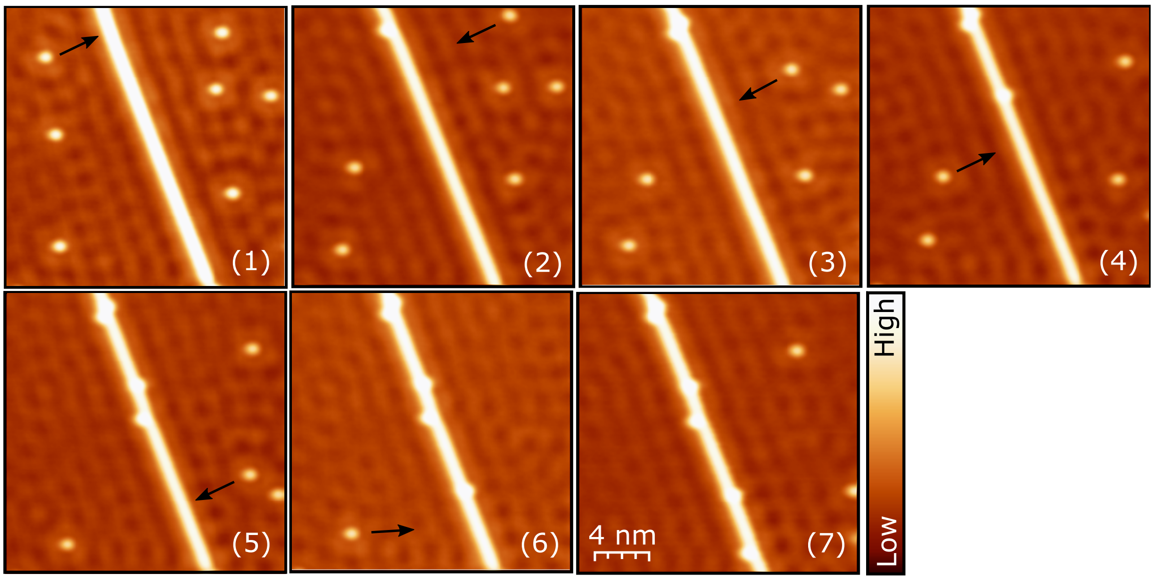

Figure 3.5: Manipulation process of Co adatoms to a monatomic chain. The manipulation directions are shown by arrows. Six Co atoms were attached to the chain from different sides and at different distances from each other. STM images were acquired at V = 30 mV and I = 30 pA (image size 19.8 nm×19.8 nm).

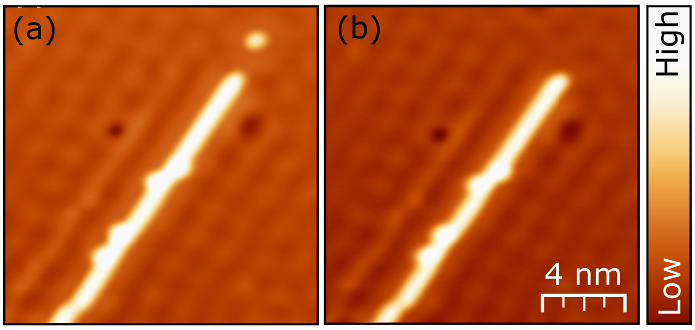

FIGURE 3.6: (a) Before and (b) after topographs of Co atom manipulation to the end of a Co_4Cu_m chain. Images were acquired at V = 30 mV and I = 54 pA (image size 15.2 nm×15.2 nm).

effect of a single Co atom attached to the side of a long monatomic chain. For that purpose, we made sure that there are no other Co atoms or dislocations such as kinks nearby at the chain. The possible adsorption sites for Co at the side of the chain are illustrated in figure 3.7(a). Repp et al. showed that Cu atoms assembled by atom manipulation in monatomic chains at 5-21 K are stable with the Cu atoms residing on fcc sites [82]. If we also consider the fcc adsorption site is more energetically favored for the long monatomic chains, then there are three likely sites for a Co atom to sit at the side of the chain. It can be positioned at fcc site or two possible hcp sites. We assumed one of the possible hcp sites (position B) is far from the chain and the adatom is not attached. The other hcp site (position C) also appears "too close" to the chain. In the manipulation process, we tried to change the position at which the Co atom was released from the tip to see whether it is possible to create both fcc and the "too close" hcp configurations. But we observed no difference in their distances from the chain and also in their dI/dV signals (figure 3.7(b)).

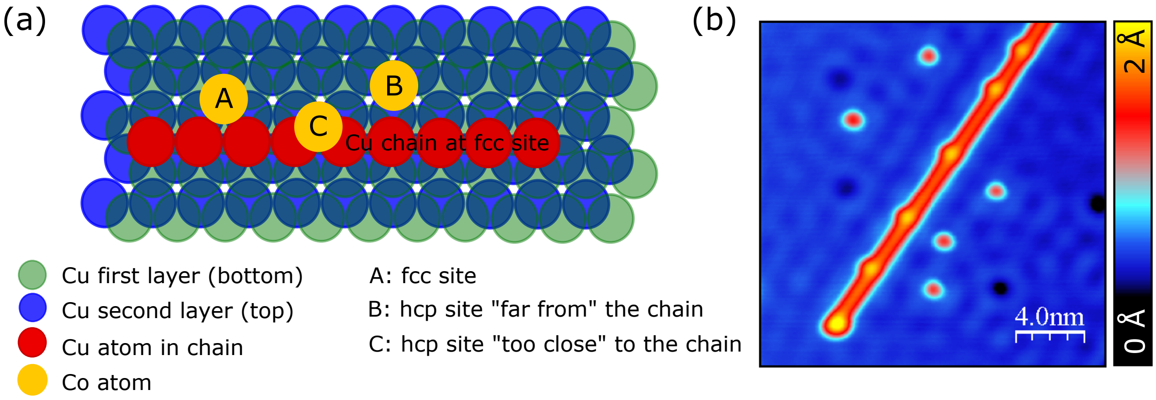

FIGURE 3.7: (a) Sketch of the Cu(111) surface illustrating the three different adsorption sites for a Co atom at the side of a fcc Cu chain. (b) Topograph of a monatomic Cu chain with Co atoms attached to its side (V = 30 mV, I = 28 pA, 20 nm×20 nm). During the manipulation, Co atoms were released at slightly different distances from the chain to study the possibility of obtaining the configurations shown in (a).

We assumed the fcc site is the energetically favored site for Co atoms at the fcc chain. The Cu substrate and the chain provide different environments for Co atoms. The Co atoms were probed by spectroscopy with the tip centered above them. The dI/dV signals of the Co atoms attached to the right and left of the chain showed no reproducible differences. However, we observed clear spectroscopic differences between three Co positions, namely on the (111) terrace, at the side, and at the end of a monatomic chain (figure 3.8). When the Co atom was attached from the side to the central part of a monatomic chain, its dI/dV spectrum exhibits a complicated structure, which neither matches a Fano nor Frota line-shape. It exhibits a small resonance at Fermi energy with depressions at $\approx \pm 10$ mV (red arrows). The amplitude of the resonance is $\approx 60\%$ lower than the Kondo resonance of Co on the (111) terrace and its width is reduced by $\approx 30\%$. Results obtained with different tips revealed the step height of depressions at $\approx \pm 10$ mV varies for different tips. However, they were always interestingly symmetric with respect to Fermi energy.

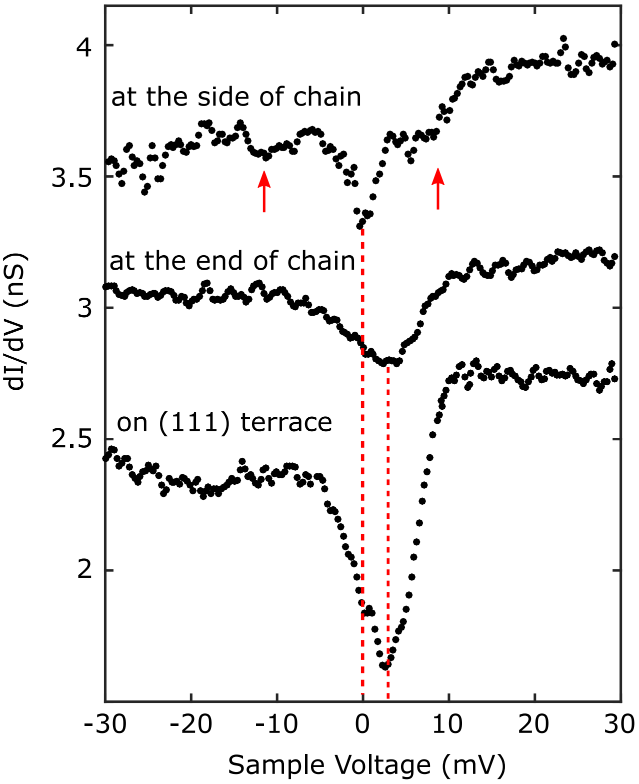

FIGURE 3.8: dI/dV spectra of Co atoms at three different positions namely on the (111) terrace, attached to the end of a Cu chain, and attached to the central part of a Cu chain. The data of Co at the central part of the chain exhibits depressions at $\approx \pm 10$ mV indicated by arrows. While the energy of the resonance minimum for the end configuration is similar to the Co on terrace (≈ 3.3 mV), it was shifted to Fermi energy for the side configuration. For the spectroscopy on Co atom on terrace and at the end of the chain, the current feedback was opened at V = 30 mV and I = 70 pA and for Co atom attached to the side of the chain, it was opened at V = 30 mV and I = 110 pA. The spectrum from the end of the chain is offset by 0.5 nS for clarity.

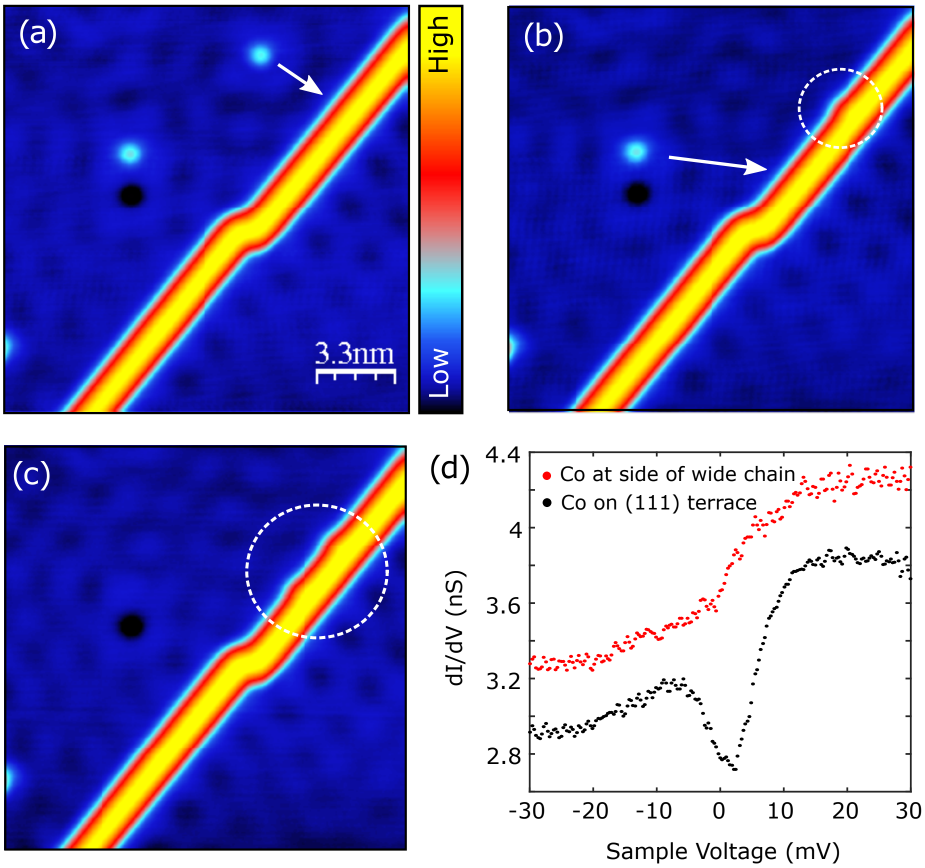

FIGURE 3.9: (a-c) STM images of manipulating two single Co atoms to a two-atom wide Cu chain (V = 30 mV, I = 100 pA). White dashed circles show the positions of Co attachment. (d) dI/dV spectra acquired above the Co atom on (111) terrace and attached to the side of the wide chain.

For Co atoms at the end of monatomic chains, a reduction of ≈ 55% in the resonance amplitude and an increase of 10% in the resonance width with respect to its Kondo resonance on the terrace was observed. In contrast to the shift of the central resonance to Fermi energy for Co atom at the chain side, the weakened resonance of Co at the end had it's minimum at approximately 3.3 mV; same as the Kondo resonance on the bare terrace.
We did the same experiment on wider chains. Figure 3.9(a-c) shows the manipulation process of attaching two Co atoms to a two-atom wide chain. The dI/dV signals of Co atoms at wide chains revealed a step-like line-shape (figure 3.9(d)). This result was reproduced with two tips on two different chains and four attached Co atoms.

3.3 Magnetic Field Measurements on Co Atom at the Side of a Monatomic Chain

As mentioned before, spin excitations represent themselves as symmetric steps with respect to Fermi energy in differential conductance. The position of the central resonance at Fermi energy and the symmetry of the observed steps at ±10 mV for Co at the side of the chain gave us the idea of spin excitations as their origin. The change of the conductance due to spin excitations is usually 10 to 50 percent of the average conductance [6].

To understand the origin of the observed features, we studied them in the presence of an external magnetic field. The key approach was to observe the Zeeman shift of the excitation in the presence of an external magnetic field. For that purpose, $\mathrm{Co}_n\mathrm{Cu}_m$ chains were reproduced in the STM operated at millikelvin temperatures. All the spectra were recorded using a lock-in detection at 812 Hz with 200 μV peak-to-peak modulation amplitude. The B-field data analysis is explained in Appendix.

3.3.1 Magnetic Field in *Z* Direction

Figure 3.10 illustrates the evolution of the measured spectra for a Co atom at the central part of the chain in the presence of an external magnetic field perpendicular to the crystal surface. While the step-like features at ±10 mV showed a small variation in their energies at different field values, we observed a significant broadening of the zero-centered resonance by increasing the magnetic field strength.

In order to analyze the splitting and the amplitude of the resonance quantitatively, we used four Fermi functions as a fit to our resonances [3]:

$$\begin{aligned} F(x) = & \frac{A_{11}}{e^{-(x-\Delta_1-x_1)/k_B T_1}+1} + \frac{A_{12}}{e^{(x+\Delta_1-x_1)/k_B T_1}+1} \\ & + \frac{A_{21}}{e^{(x+\Delta_2-x_2)/k_B T_2}+1} + \frac{A_{12}}{e^{-(x-\Delta_2-x_2)/k_B T_2}+1} \end{aligned} \tag{3.1}$$

where A_{11} and A_{12} are amplitudes of the inner steps, Δ_1 is the step position, x_1 is its energy shift with respect to Fermi energy, and T_1 is the extracted effective temperature for the inner steps. A_{21}, A_{22}, Δ_2, x_2, and T_2 are their equivalents for the outer steps.

Obtained fits shown as red lines in figure 3.10 reproduce the experimental data very well. The extracted values are listed in Table (3.1). When the magnetic field was increased up to 9 T, the central resonance was broadened by ≈ 44% and weakened in amplitude by ≈ 43%. Second derivative of dI/dV spectra are shown in figure 3.11. The changes in the energy position and the step height are more visible in the second derivative. Magnetic field dependence of the Δ_1 for three individual Co atoms at chains are illustrated as an

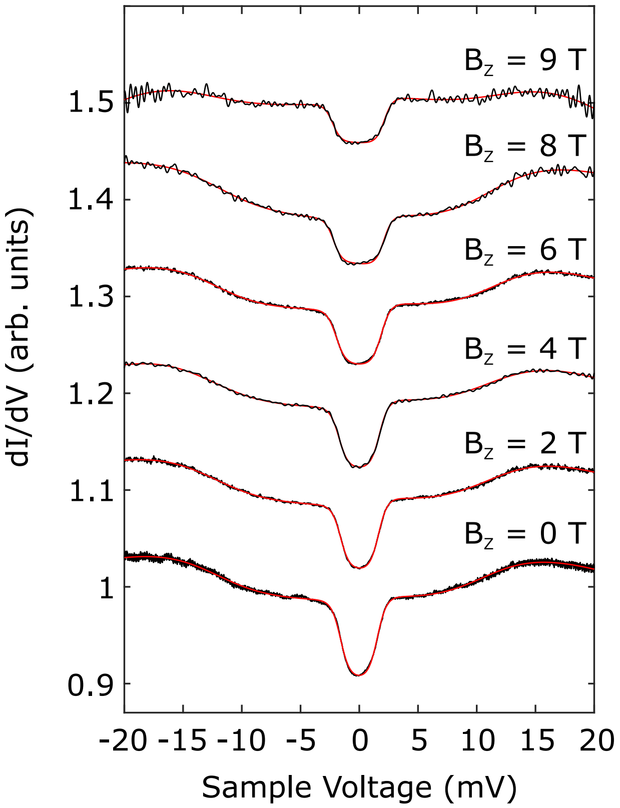

FIGURE 3.10: dI/dV spectra of Co atom at the central part of a Cu chain in the presence of applied out of plane magnetic field, B_Z. A significant shift of the symmetric low energy steps by increasing the magnetic field was observed. The spectra were fitted by four Fermi functions shown as red lines. Current feedback was opened at V = 20 mV and I = 5 nA. The spectra of B_Z equal to 4, 8, and 9 T are subjected to FFT-filtering for noise removal.

TABLE 3.1: Extracted values from the fits for the resonance of Co atom at the side of a monatomic chain in the presence of external out-of-plane magnetic field.

	$B_Z = 0$ T	$B_Z = 2$ T	$B_Z = 4$ T	$B_Z = 6$ T	$B_Z = 8$ T	$B_Z = 9$ T
A_{11} (nS)	0.21	0.19	0.19	0.17	0.13	0.13
A_{12} (nS)	0.2	0.16	0.16	0.15	0.13	0.10
Δ_1 (mV)	1.57	1.57	1.81	1.87	2.14	2.27
T_1 (K)	3.4	3.4	3.9	4.0	3.5	3.7
A_{21} (nS)	0.23	0.20	0.25	0.25	0.20	0.25
A_{22} (nS)	0.23	0.20	0.22	0.25	0.28	0.25
Δ_2 (mV)	11.9	12.0	12.5	12.6	12.1	13.6
T_2 (K)	23	23	22	23	23	24

inset in figure 3.11. They showed a hyperbolic dependence on the field strength. The outer steps shifted slightly to higher energies by increasing the field up to 9 T (with exception of 8 T) and their amplitude did not alter in a systematic manner.

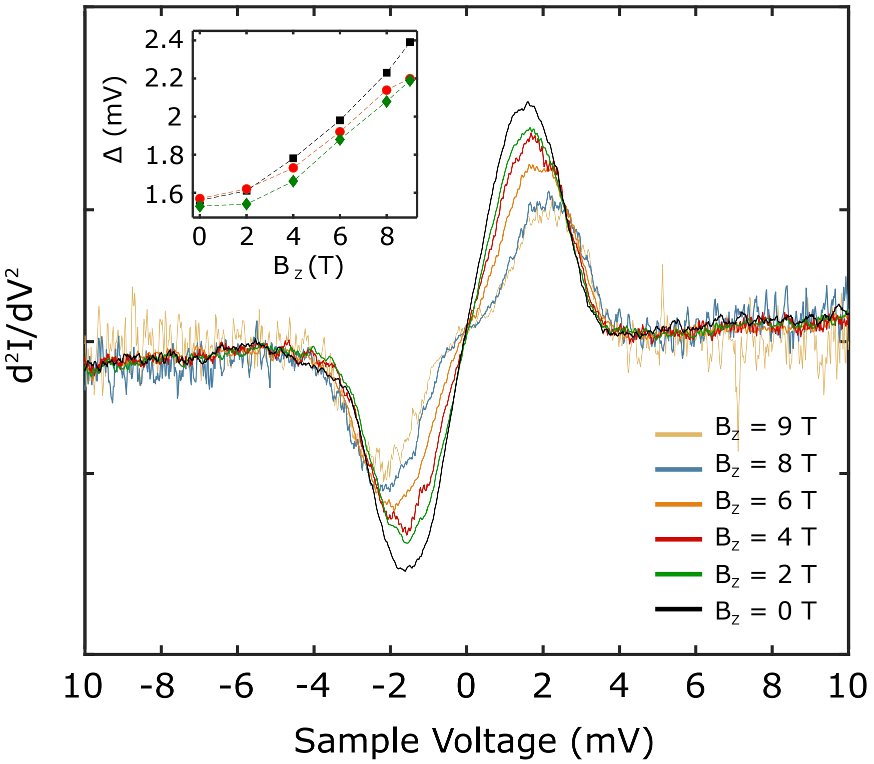

FIGURE 3.11: Derivative of the dI/dV spectra in figure 3.10 for Co atom at the central part of a Cu chain in the presence of applied out-of-plane magnetic field, B_z. The inner steps positions in the dI/dV signal (Δ) appears as extrema in d^2I/dV^2. Its variation as a function of the magnetic field is shown in the inset.

3.3.2 Magnetic Fields in X and Y Directions

Same measurements were performed with the applied magnetic field in two in-plane directions: parallel (X) and perpendicular (Y) to the chain. Obtained dI/dVs are shown in figure 3.12. When the magnetic field is parallel to the chain (X direction), same energy positions of the inner steps and an amplitude reduction of $\approx 10\%$ were observed compared to the spectrum with no applied magnetic field.

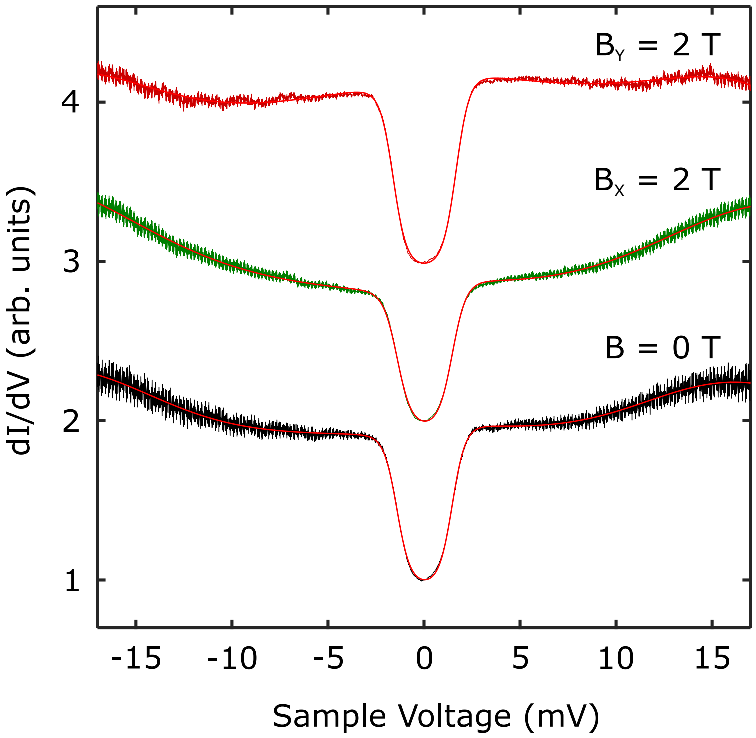

FIGURE 3.12: dI/dV spectra of Co atom at the central part of a Cu chain in the presence of no external magnetic field, and applied magnetic field in the in-plane directions, B_x and B_y. Current feedback was opened at V = 20 mV and I = 5 nA. For the B_x direction, no change in the width of the resonance was observed, while its amplitude decreased by ≈ 10%. An increase of ≈ 13% in the width and ≈ 19% in the amplitude of the zero-centered resonance was observed when the magnetic field B_y =2 T was applied.

However, despite the small variation of the steps energy positions in the B_x field, when the magnetic field was perpendicular to the chain (Y), the width and the amplitude of the zero-centered feature increased by ≈ 13% and ≈ 19%, respectively.

3.4 Interaction Between Co Atoms at Long Cu Chain

Several experiments were conducted to understand the short-range or indirect long-range interactions between spins in magnetic structures [83–87]. Interaction between two individual Co atoms was studied on Au(111) [88]. For distances less than 6 Å, a disappearance of the Kondo resonance was reported.

We also investigated the interaction between two individual Co atoms via the long monatomic copper chain. To do that, they were attached to the chain from the same side or the opposite sides of the chain with different separations. Figure 3.13(a) illustrates a Co_6Cu_n chain where Co atoms were attached from both sides to the chain. The bulge of Co atoms at the chain indicates the side of its attachment. Co_3 and Co_4 atoms were attached close to each other in a way that it was neither possible to see individual atoms in

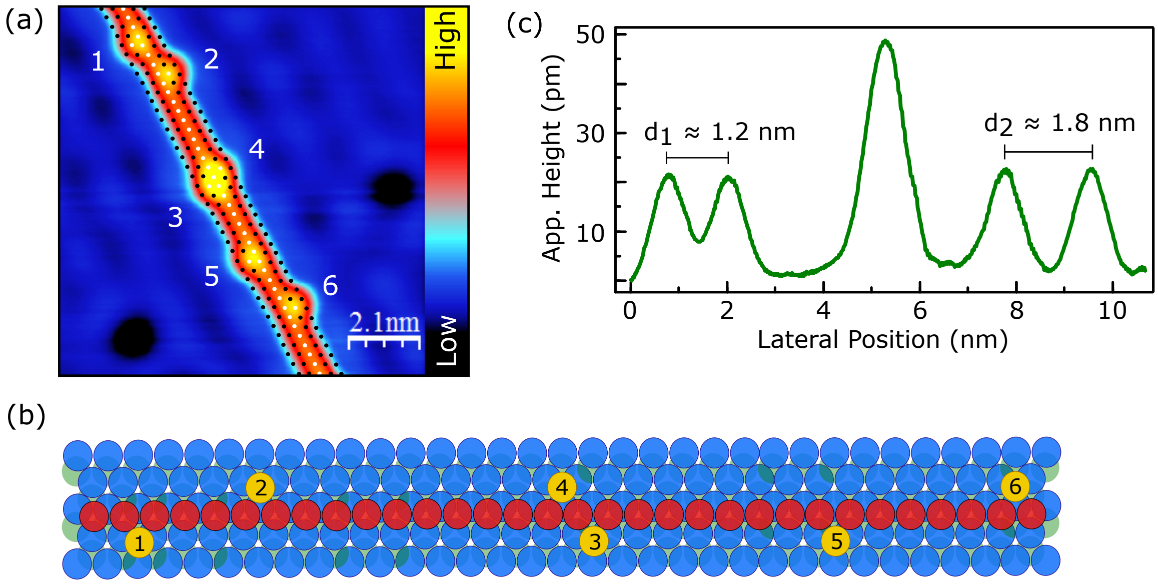

FIGURE 3.13: (a) Topograph of a monatomic Co_6Cu_n chain acquired at V = 30 mV, I = 30 pA and T = 4.6 K. Co atoms were attached to the Cu chain from different sides with separations ≈ 1.2 nm, ≈ 1.8 nm, and less than 6 Å. Dots represent the simulation for the adsorption sites of Cu chain and Co atoms at chain. Both Cu atoms of the chain and attached Co atoms are assumed to be at fcc sites of the surface. (b) Schematic plot of the simulation (dots in (a)) for adsorption sites of the Cu chain and the attached Co atoms. (c) Height profile along the white dots shown in (a). The closely attached Co_3 and Co_4 appeared as one single peak with an apparent height of approximately two times larger than the pairs with large separations.

the topograph nor in the height profile. The large bulge in the middle of the chain shows the closely-attached Co atoms. The smallest distance between Co atoms on Au(111) at which they can be resolved individually was reported 6 Å [88].

To determine the distance between Co atoms, we superimposed the atomic arrangement of a Cu(111) surface. First, the maximum apparent height of the chain was found (white dotted-line in figure 3.13(a)). Cu atoms of the chain and attached Co atoms were assumed to be at fcc sites of the surface. By considering lattice constant of Cu(111) and the scanning piezo constant, we defined two rows of fcc adsorption sites parallel to the chain (black dots in figure 3.13(a)). According to this procedure, we obtained the schematic plot shown in figure 3.13(b). The height profile along the white dots is shown in figure 3.13(c). The apparent height of the closely attached pair is approximately two times larger than the pairs with large separations. The separation between Co atoms in the other two Co pairs, (Co_1, Co_2) and (Co_5, Co_6) were ≈ 1.2 nm and ≈ 1.8 nm, respectively.

3.4.1 Co Atoms at Chain with Large Separation

To see whether there is a coupling between Co atoms via the chain and whether this coupling depends on the distance between them, we varied their separations up to 10 nm. dI/dV

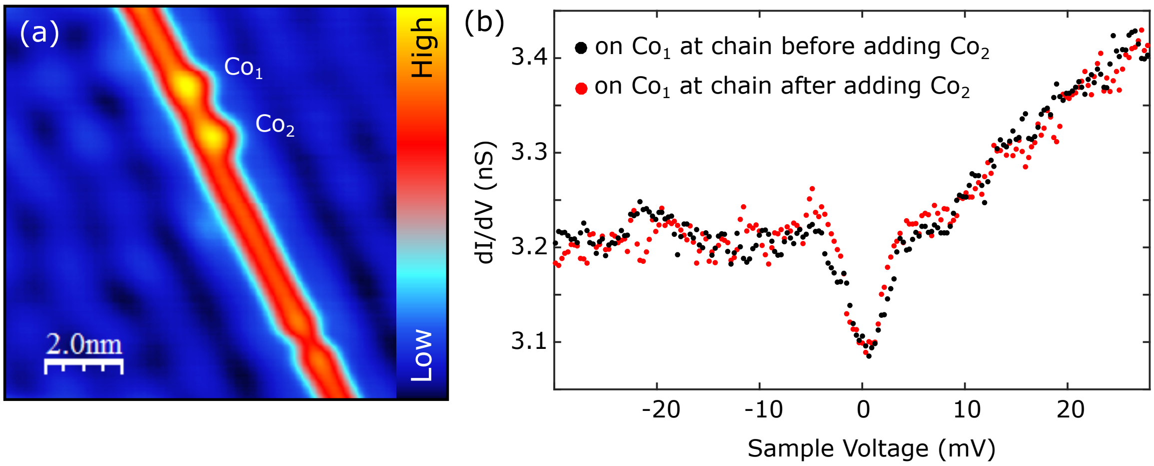

FIGURE 3.14: (a) Constant current image of a monatomic Cu chain with two Co atoms attached to the same side of the chain with separation ≈ 1.5 nm (V = 30 mV, I = 40 pA). (b) dI/dV spectra of Co_1 before and after attaching Co_2 to the chain. No change of the Co_1 resonance line-shape was observed after attaching Co_2 to the chain. The current feedback was opened at V = 30 mV and I = 100 pA.

spectroscopy was performed on the first Co atom at the chain before and after adding the second Co atom to the chain.

Figure 3.14(a) shows a topograph of Co_2Cu_n chain fabricated using the 4 K STM. dI/dV signals were obtained on the first Co atom (Co_1) before and after attaching the second Co atom (Co_2) to the same side of the chain at ≈ 1.5 nm distance from Co_1 (figure 3.14(b)). We observed no indication of coupling between Co atoms regardless of their attachment sides. The dI/dV signals for both Co atoms were similar to the resonance of single Co atom at chain showing a small resonance at Fermi energy with depressions at ≈ ±10 mV. Measurements were performed on more than twenty Co_2Cu_n chains with different large separations between Co atoms. They all showed no evidence of coupling between Co atoms. We also fabricated the Co_2Cu_n chains in mK STM and repeated the measurement at a lower temperature with applied magnetic field in Z direction (figure 3.15). The observed steps in the resonance of Co atoms at these chains also evolved in the same manner as a single Co atom at a monatomic Cu chain in the presence of magnetic field. By increasing the magnetic field strength up to 7 T, the central resonance of both Co atoms were broadened by ≈ 38% and weakened in amplitude by ≈ 46%.

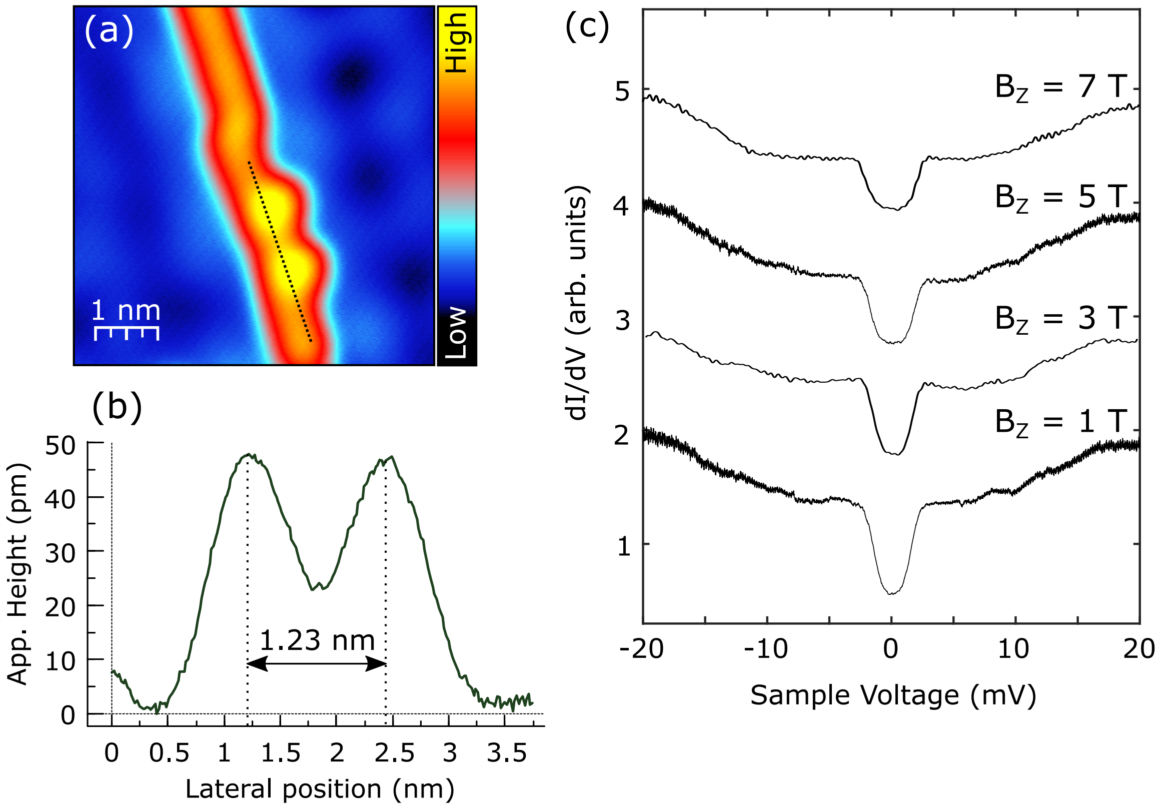

FIGURE 3.15: (a) Topograph of a Co_2Cu_n chain acquired at V = 20 mV, I = 1 nA, and T ≈ 400 mK. (b) Height profile along the dashed line in (a). The distance between Co atoms was ≈ 1.23 nm. (c) dI/dV spectra obtained on top of the Co atom in (a) in the presence of applied B_Z magnetic field up to 7 T. The current feedback was opened at V = 20 mV and I = 5 nA. Despite the presence of a second Co atom at the distance ≈ 1.23 nm at chain, both Co atoms showed the same behavior as a single Co atom at chain in the presence of an external B_Z field. At B_Z=7 T, the width of the central resonance increased by ≈ 38% and its amplitude decreased by ≈ 46% with respect to B_Z=1 T. The spectra of B_Z equal to 3 T and 7 T are subjected to FFT-filtering for noise removal.

3.4.2 Co Atoms at Chain with Small Separation

Figure 3.16(a) illustrates a Co_4Cu_n chain. Co_1 and Co_2 were attached to the chain from opposite sides close to each other. In contrast to the Co_2Cu_n chains with large separations between Co atoms, we observed a different resonance line-shape for the two closely-attached Co atoms. The amplitude of the central resonance increased by ≈ 130% and it broadened by ≈ 61% (figure 3.16(b)).

In the presence of the out-of-plane magnetic field, by increasing the field strength up to 7 T, the width of the central resonance did not change and its amplitude decreased by ≈ 10% with respect to B_z = 1 T (figure 3.17).

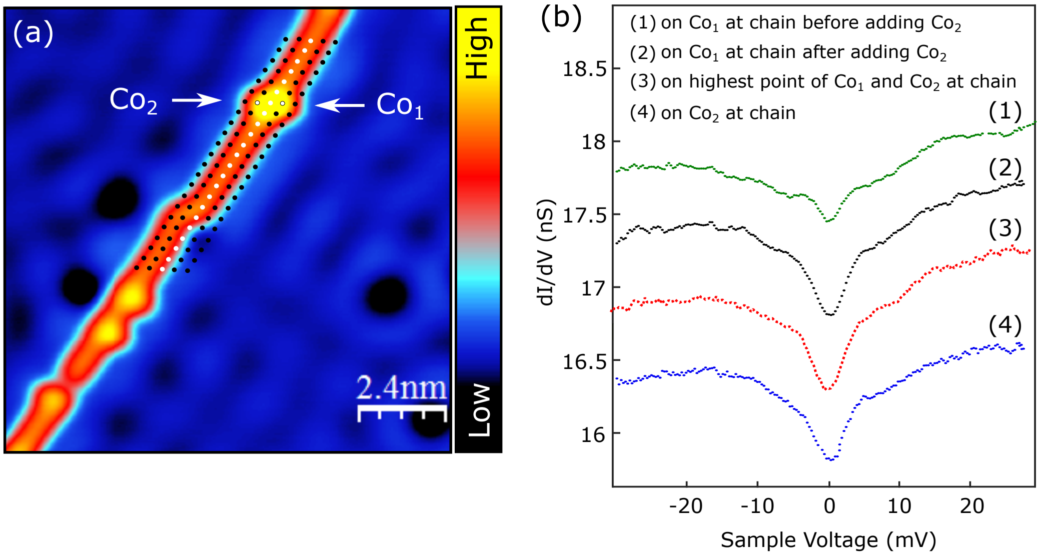

Figure 3.16: (a) STM image of a monatomic Co_4Cu_n chain acquired at V = 58 mV and I = 50 pA. Co_1 and Co_2 were positioned similar to the (Co_3,Co_4) configuration in figure 3.13(c). (b) *dI/dV* spectra on Co_1 before and after attaching Co_2 to the chain. Current feedback was opened at V = 30 mV and I = 490 pA. For the closely-attached configuration, we observed a significant increase of the width and the amplitude of the central resonance by ≈ 61% and ≈ 130%, respectively. Spectra labeled as (1), (2), and (3) were shifted by 1.5, 1, and 0.5 nS for clarity.

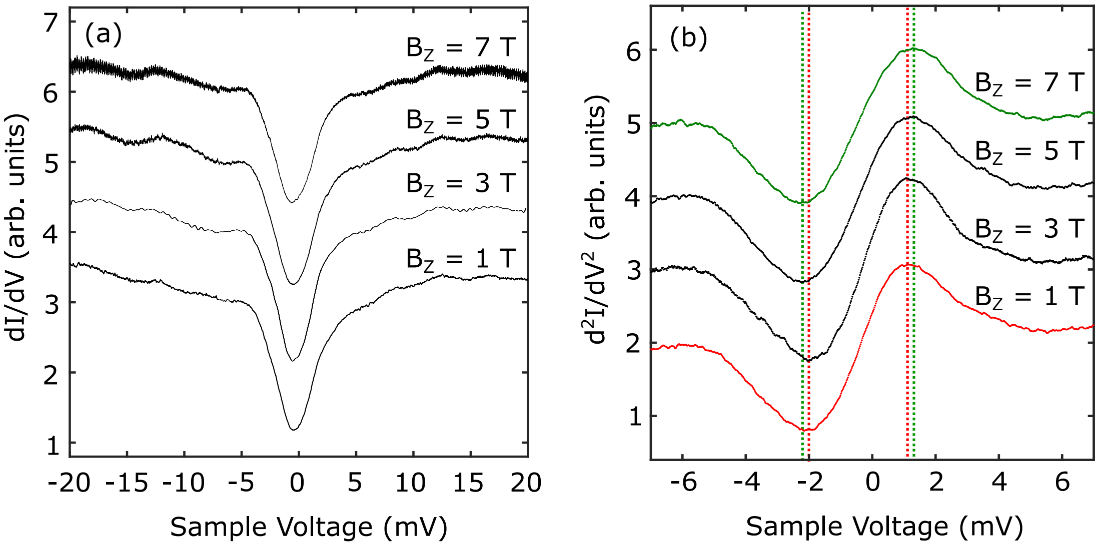

Figure 3.17: (a) *dI/dV* spectra obtained on top of Co atom in the closely-attached configuration (figure 3.16(a)) in the presence of applied magnetic field in *Z* direction up to 7 T. The current feedback was opened at V = 20 mV and I = 5 nA. (b) Derivatives of *dI/dV* signals shown in (a). By applying magnetic field up to B_Z=7 T, the amplitude of the central resonance decreased by ≈ 10% and its width increased only by ≈ 0.6%. The spectrum of B_Z=3 T is subjected to FFT-filtering for noise removal.

3.5 Discussion

A simple model for the directional quenching of *d*-orbital momentum of an atom on a surface is shown in figure 3.18. In the gas phase, the atom has five degenerate *d*-orbitals. When this atom is deposited on a surface, the electrons of the *d*-orbitals pointing towards the sample will experience an energy shift due to the crystal potential of neighboring atoms. The electric field originated from the surrounding charge distribution (crystal field) aligns the *d*-orbitals into favored directions and defines a quantization axis. The electrons in the aligned d-orbitals closer to the nearest neighbor atoms experience a higher crystal field. This breaks the degeneracy of *d*-orbitals and they split in energy. This phenomenon is known as the crystal-field splitting of the energy levels and the orbital momentum in the aligned directions is "quenched" [89].

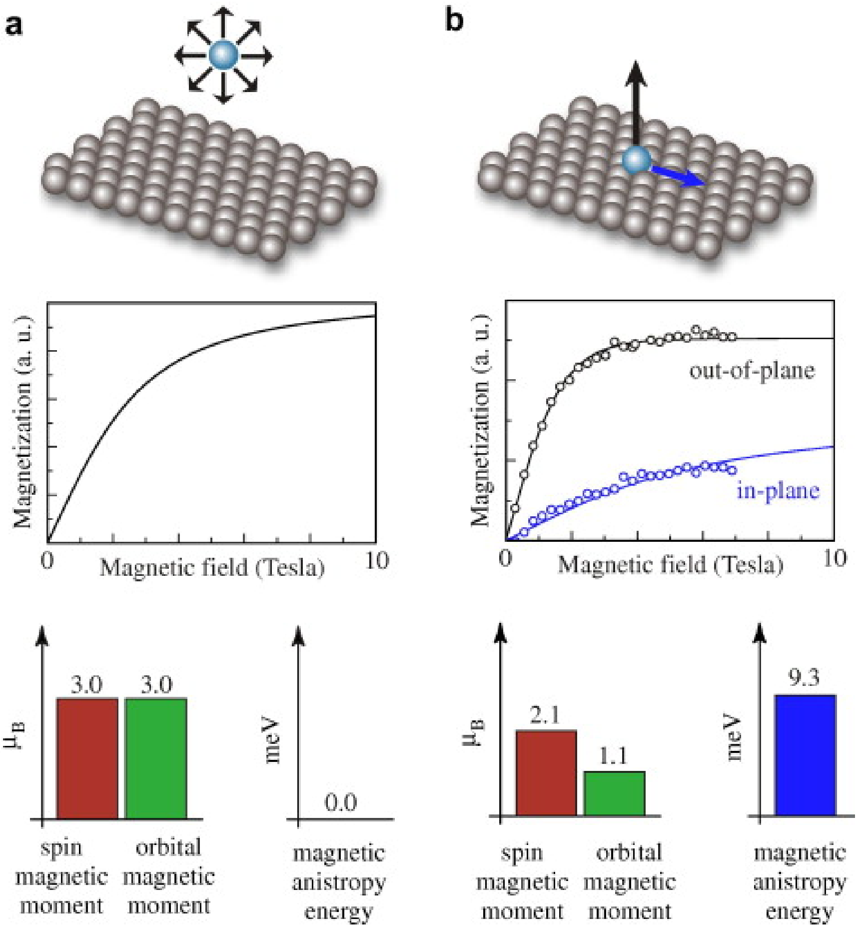

FIGURE 3.18: Orbital and spin magnetic moment of Co atom with d^7 electronic configuration for (a) the gas phase, and (b) deposited on Pt(111) surface. Crystal field induced by the surface Pt atoms leads to a strong magnetization of the Co atom. Adapted from [90].

3.5.1 Selective Hybridization of $3d$ Orbitals

Many experiments have been performed to achieve the maximum magnetic anisotropy energy (MAE) and fabricate stable nano-magnets. The deposition of magnetic atoms on a surface results in orbital quenching and creation of magnetic anisotropy. To detect it, one has to eliminate other types of many-body scatterings such as the Kondo effect. In principle, the Kondo effect and the spin excitation are both based on the spin-flip process. The main difference is the energy cost of this flipping process. While the spin-flip scattering is an elastic process for the Kondo effect, in the spin excitation the energy of the system changes after the spin is flipped.

There are experimental methods for maximizing MAE. A decoupling layer can increase the spin-lifetime so that IETS signals become more pronounced. A good example is the experimentally measured IETS signals for Co and Fe adatoms deposited directly on Pt(111) and CuN decoupling layer on Cu(100). Despite a clear appearance of the excitation steps in the measurements on CuN/Cu(100), a second derivative was needed for a better observation of the IETS signals for Co and Fe adatoms on Pt(111) [5, 40].

Co atom with $L = 3$ has the highest orbital moment among the transition metals and is a good candidate to achieve a high MAE on metal surfaces [7]. We chose Cu(111) because the Kondo effect of Co on this substrate has been previously studied with STM in a good extend.

In collaboration with the group of Prof. Alexander Lichtenstein, multi-orbital many-body calculations in the framework of continuous-time Quantum Monte Carlo (QMC) are performed by Roberto Mozara for Co adatoms on a Cu(111) surface and at different positions of a Cu chain. According to the preliminarily results, for Co on the (111) terrace, the d_{z^2} orbital is mainly responsible for the Kondo resonance. The hybridization of d_{xy} and $d_{x^2-y^2}$ orbitals are the weakest among all d orbitals because their wave functions are oriented in the plane parallel to the surface and no adatoms on the surface are located nearby. The d_{xz} and d_{yz} orbitals have overlaps with the underlying lattice atoms and are expected to have a considerable hybridization with them [91].

By attaching the Co atom to the side or the end of a Cu chain, the hybridization of Co d orbitals alters. Figure 3.19 illustrates the coordinates of different d-orbitals of Co atom attached to the side (left column) and the end (right column) of a monatomic Cu chain. The Cu chain introduces more spatial asymmetry to the environment. This spatial asymmetry leads to anisotropy within the crystal field and modifies the hybridization of d-orbitals. When the Co atom is attached to the side of the chain, as shown in figure 3.19(d,e), d_{xy} and $d_{x^2-y^2}$ in-plane orbitals are directed to the Cu atom of the chain. Thus, an enhanced hybridization in that direction is expected. Specially, the two lobes of d_{xy} orbital are pointing nearly directly to two Cu atoms in the chain. So we expect a higher hybridization for

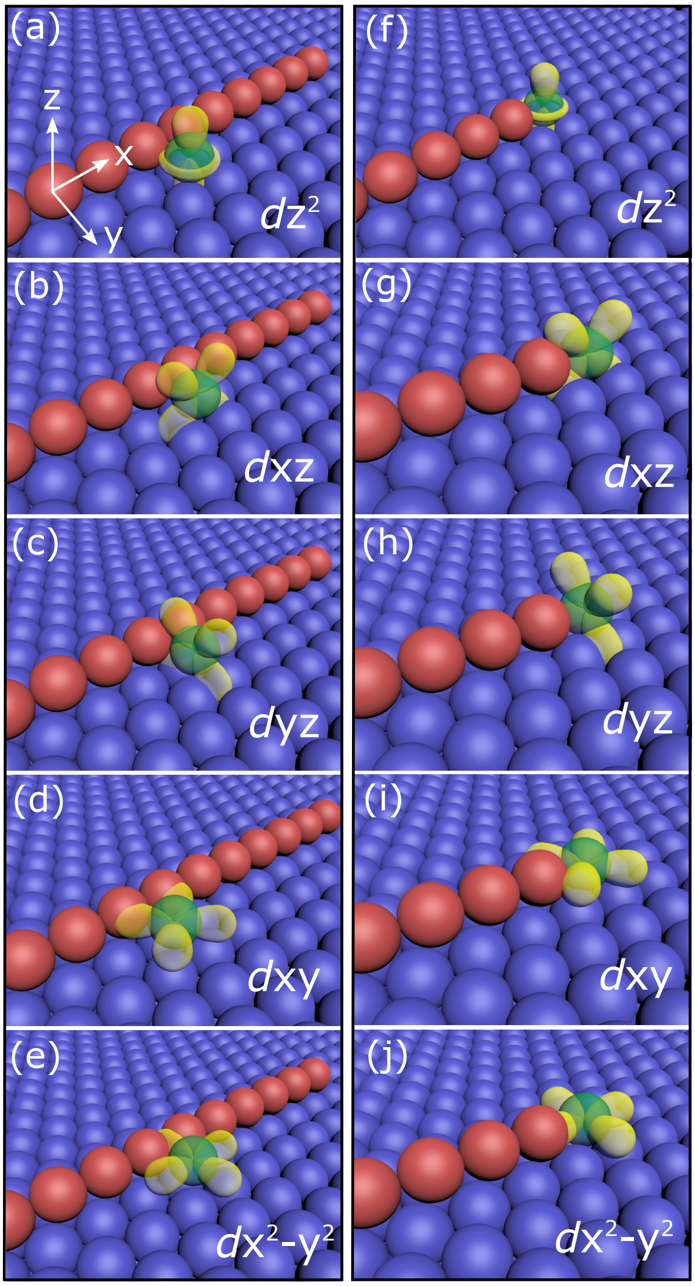

FIGURE 3.19: The ball model of a CoCu$_n$ chain with Co atom attached to the side (left column) and to the end (right column) of the chain. The contour representation of Co 3d orbitals illustrates the spatial dependence of their hybridization with the chain Cu atoms.

d_{xy} compared to $d_{x^2-y^2}$ with its only one lobe directed to the chain. Moreover, since d_{yz} is perpendicular to the chain, we expect a higher modification in its hybridization than d_{xz} which is parallel to the chain (figure 3.19(b,c)).

Considering the in-plane orbitals for the Co atom at the end of the chain (figure 3.19(i,j)), only one of $d_{x^2-y^2}$ lobes is pointing towards the chain. Also, the diagonal d_{xz}-orbital hybridized with the last Cu atom of the chain. By adding Co atom to the chain end, the spatial symmetry is less manipulated and Co orbital momentum is not as perturbed as when it is attached from the side. At the time of writing this thesis, further calculations are performed to include the SOC effect in the many-body Kondo calculations. The initial results show by considering SOC, which is needed for magnetic anisotropy, drastic changes arise in the orbital-resolved spectral function. These first theoretical results promise that the observed drastic changes at the tunneling spectra can be theoretically reproduced in the near future.

In conclusion, we used STM to create nano-structures and manipulate adatoms to modify the substrate-impurity hybridization controllably. Long Cu chains were fabricated in a much quicker way than atom by atom manipulation. The observed nano-structures such as wide chains, vacancy lines with different widths, and observed kink dislocations in chains can be used as perturbations introduced to the environment of the magnetic impurity. We were able to engineer the energy cost of the spin-flip process of Co atom deposited directly on a metal surface. This may eventually help us to fabricate systems with a large MAE in the presence of other many-body scattering phenomena.

Chapter 4

Apparent Tunneling Barrier Height of Atomic Arrays

The results presented in this chapter were published in 2018 in the Beilstein Journal of Nanotechnology [92]. The coauthors are Alexander Weismann and Richard Berndt. Using STM, we experimentally showed that the apparent tunneling barrier height obtained from STM measurements is not a correct representation of the local work function. The text in this chapter is a modified version of the published work.

4.1 Introduction

The scanning tunneling microscope can be used to study local work function [93, 94]. On the crystal surfaces, the spill-out of electrons results to a modified surface potential and leads to an increase in Φ [95, 96]. This electric charge spill-out can be influenced by the atomic concentration and arrangement. The spill-out of electrons from a more densely-packed (111) facet of crystals resulted in a stronger electric field on these surfaces and a larger increase in the Φ is expected for them compared to other facets of the crystal (origin of local work function concept). In 1941, Smoluchowski suggested a variation of local work function for the atomic steps [97]. A step and a flat terrace differ in the available surface area for the electrons to spill-out. Considering a constant charge distribution, a step provides a larger area for electrons to spill-out and it has a lower charge density compared to a flat terrace. As a result, the generated electric field at steps are weaker compared to terrace. This effect is known as Smoluchowski effect and according to it, a lower local work function is expected at the steps compared to terrace. Kelvin probe technique [98] and photo-electron spectroscopy were used to probe this effect experimentally [99].

To study local work function with STM, the most simple one-dimensional model was used. According to that, at low bias voltages the tunneling current is proportional to the average of the tip and the sample work functions [15, 100]. However, for a more precise study of the local work function with STM, other phenomena such as image potential and Smoluchowski effect need to be included [101–104]. In practice, the concept of apparent barrier height is introduced to include all the possible quantum effects in the potential barrier an electron sees when tunneling from one electrode to the other. The tunneling current varies exponentially with z, and Φ is replaced with the apparent barrier height Φ_{app} [105]. In STM measurements the unknown electronic structure of the tip introduces complications in relating Φ_{app} to the local work function of the sample Φ. However, similar changes of the local work function and apparent barrier height for different atomic structures is expected [106–109].

It was proposed that the lateral confinement of the tunneling current in STM may cause an increase in the barrier height [105]. The spatial geometries of nano-structures affect the extension of the electron wave function [110]. Limot in Ref. [111] discussed the effect of lateral confinement in the apparent barrier height in single-atom contacts. Au contacts of two (001) surfaces, in a planar form or with an adatom or with a five-atom pyramid configurations were subjected to the atomistic transport calculations [112]. The extracted values of apparent barrier heights were 5.7, 6.7, and 6.8 eV, respectively. The deviation of the calculated value of the flat terrace from the experimentally obtained value was attributed to a systematic calculation error in the local density approximation [112, 113]. Aside this quantitative deviation, the trend of the barrier height increase for more laterally confined tunneling paths is expected to be true. According to these results, the barrier height is expected to be of the order of 1 eV larger for the electrons tunneling in a strongly confined path.

Here we used fabricated nano-structures on Cu(111) to study the apparent barrier height. Their unique atomic structures led us to decompose them into steps and compare the experimentally obtained Φ_{app} values with the expected theoretical trend.

4.2 Experiment

Cu(111) sample and tip were cleaned with the same procedure explained in section (2.2). Atomic chains with different widths were also fabricated as described in section (3.1). Among the fabricated dislocations, we also observed long vacancy lines (trenches) with different widths. They have apparent depth same as the apparent height of the chains. A clean Cu(111) surface with the fabricated nano-structures, namely monatomic chains, a wide chain, and trenches with single-atom or wider widths are shown in figure 4.1. Also,

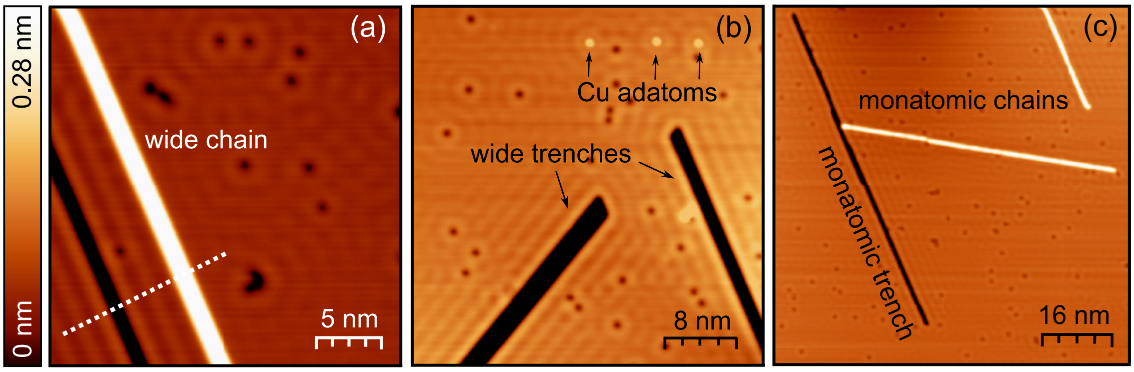

FIGURE 4.1: STM images of a Cu(111) surface with chains and trenches of monolayer height. (a) A Cu chain approximately two atoms wide and a parallel trench. (b) Two wide trenches (approx. 2 and 3 atoms) with deposited single Cu atoms. (c) Monatomic chains and trenches. The images were acquired at (a) V = 20 mV and I = 3 nA and (b, c) V = 100 mV and I = 5 nA [92].

single Cu adatoms were transferred from the tip to the surface [111]. To perform IZ spectroscopy, the current feedback was opened at a sample voltage of V = 20 mV and a current of I = 200 pA. The tunneling current was monitored while the tip was brought close to the structure under investigation (excursion rate 1.7 nm/s). According to the formula

$$I \propto exp(-2\kappa z) \;\propto\; exp(-1.025\sqrt{\Phi_{app}}\Delta z) \qquad (\text{eV and Å}) \tag{4.1}$$

one can extract Φ_{app} from the slope of the current-distance ($I(\Delta z)$) data as

$$\Phi_{app} = 0.952\left(\frac{d\ln I}{dz}\right)^2 . \tag{4.2}$$

4.3 Results and Discussion

The obtained data from IZ spectroscopy on a clean Cu(111) surface and the fabricated nano-structures, namely a monatomic chain, a wide chain, and trenches with single-atom or wider width and the deposited single Cu atoms are shown in figure 4.2. The terrace data (black lines) is plotted with $I(\Delta z)$ data of each structure for an easy comparison. Using equation (4.2), the apparent barrier height of the fabricated nano-structures were calculated from the slopes of the $I(\Delta z)$ data (Table 4.1). To avoid any tip effect, all the measurements were performed with the same tip apex. The maximum slope belongs to single Cu atoms which results to the maximum apparent barrier height for them. Following them, the apparent barrier height of monatomic chains were also larger than the value of the (111) terrace. As the chain width increased, its Φ_{app} value becomes closer to the terrace Φ_{app}. This reduction trend of Φ_{app} was followed for the trenches and the minimum value

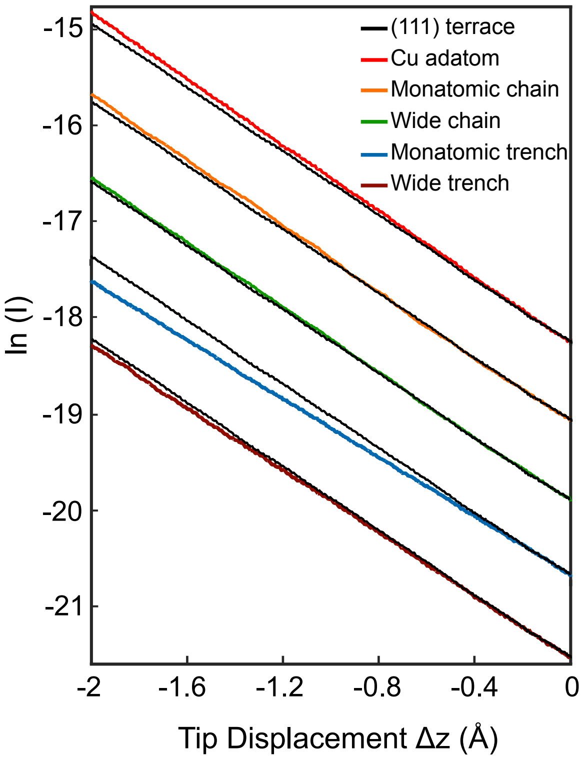

FIGURE 4.2: Current-distance data $I(\Delta z)$. Negative values of Δz indicate reduced tip-sample distances with respect to the initial separation defined by I = 200 pA and V = 20 mV. Data recorded from a (111) terrace (black), a Cu adatom, a monatomic chain, a wider chain ($\approx$ 2 atoms), and trenches of monolayer depth with single atom and wider width ($\approx$ 2 atoms) are displayed. The curves are arbitrarily offset along the ordinate for clarity. The terrace data are shown with each curve for comparison. Small undulations of the data are due to low-frequency vibration of the microscope [92].

was obtained for monatomic trenches. Measurements were also performed at a different low bias voltage (V = 10 mV). Regardless of the tip structure and the applied low bias voltage, we observed the same trend of Φ_{app} variation for the fabricated structures.

To interpret the observed Φ_{app} trend using Smoluchowski effect, the monatomic chain and the single Cu atom were decomposed to normal steps as figure 4.3. According to these simulations, the generated dipole moment on each step reduces the work function and since there are more than one step in each structure, an stronger reduction of the work function compared with a single step (and flat terrace) is expected for these bulges. However, an opposite trend of Φ_{app} was observed. Not only higher Φ_{app} values were observed for them compared to terrace, but also Cu adatom with more number of steps showed heigher Φ_{app} value to compare with monatomic chain with two steps in its simulation. Misalignment of the local surface normal with the z direction of the STM may also affect Φ_{app} [114]. Φ_{app} of atoms and chains were measured on the topmost position of them where $\alpha \approx 0$. However, even if there was α degree of misalignment, it is expected to reduce Φ_{app} by a factor $\cos^2\alpha$. Earlier theoretical works suggested the contribution of electrons kinetic energy in the Φ_{app}

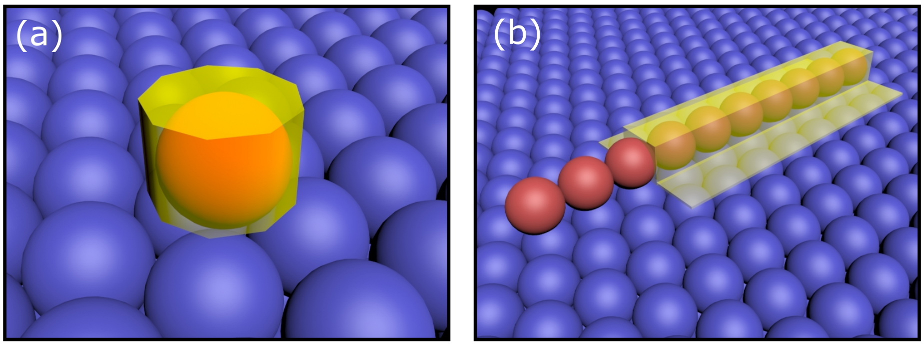

Figure 4.3: The ball model of (a) a single Cu atom and (b) a monatomic Cu chain on Cu(111). The Cu chain and the Cu atom are simulated by two parallel steps and a polygonal prism, respectively. According to Smoluchowski effect, a lower apparent barrier height is expected at the upper edge of the steps.

[105, 111, 112]. The geometry of the fabricated structures define the lateral extension of the tunneling current. For a Cu atom, the tunneling electrons are confined in a narrow path between the tip and the sample. This path becomes broader for the chains and further broader when one end of the tunneling path is a flat terrace. We observed the Φ_{app} for these nano-stuctures varies with the same trend as the tunneling current filament laterally extend in them which was also predicted theoretically in Ref. [112]. The fabricated structures manipulate the potential barrier in a way that an opposite trend of experimentally observed Φ_{app} variation was expected. This Contrary to expectation may be a consequence of kinetic-energy contribution in the local work function.

The local work function for the trenches needs a more detailed analysis. From the lateral extension point of view, when the tip is adjusted on top of a trench, the two sides terraces are closer to the tip than the trench bottom. As a result, a considerable part of the electrons are expected to tunnel to the edge atoms of the adjacent terraces and the tunneling path widens laterally. A decrease of Φ_{app} is expected from this widening. Moreover, there is a α degree between the z direction of the STM and these edge atoms of the adjacent terraces which leads to reduction of Φ_{app}. Unfortunately, the lack of theoretical data for these structures limits a more detailed analysis.

In conclusion, the atomic structure of the tip and the sample define the extension of the

Structure	(eV)
(111) terrace	3.9
adatom	4.2
monatomic chain	4.2
wide chain	4.0
monatomic trench	3.3
wide trench	3.8

Table 4.1: Apparent barrier heights Φ_{app} extracted from Fig. 4.2 [92].

tunneling current filament. The tunneling electron wave function is confined through the tunneling path with respect to the their atomic structures. This different lateral extension of the current add a kinetic-energy contribution to the Φ_{app} which was of the order of 1 eV for our investigated structures. To make the apparent barrier height a reliable representation of the local work function, the kinetic-energy contribution needs to be taken into account.

Chapter 5

Surface State Role in the Kondo Effect of Co Adatom on Cu(111)

5.1 Introduction

Many-body phenomena are the quantum correlations between particles in a system. In the case of the many-body Kondo effect, this correlation is between the magnetic atoms and the conduction electrons of the supporting substrate. According to the Coqblin-Schrieffer model, the Kondo temperature depends on the local density of states (LDOS), ρ, as [78]

$$T_K = De^{-1/2J\rho} \tag{5.1}$$

On the (111) surfaces of noble metals, in addition to bulk states, surface states extend parallel to the surface and are confined in the last few atomic layers. They are located in a gap of bulk band structure and have a free-electron like dispersion along the surface [115]. Techniques such as STM and angle-resolved photoemission spectroscopy (ARPES) are used to detect them [116–119]. According to the equation (5.1), ρ is the sum of surface and bulk LDOS. A fundamental and so far not clearly answered question is the contribution of surface state electrons (ρ_s) in the Kondo effect. Is the interaction mainly between the magnetic atom and bulk electrons of the host metal or do the surface state electrons also play a role in it?

This issue becomes more concerning when a magnetic atom is adsorbed on noble metal (111) surfaces [120, 121], where bulk and surface electrons both can be a source of this many-body interaction [120, 121]. Several experimental works were conducted to answer this fundamental question, but their research did not come to similar conclusions [59, 67, 121–129].

To study the role of surface state electrons in the Kondo effect, step edges of a (111) facet of noble metal crystals provide a convenient system. Inhomogeneities as step edges and point defects can cause scattering of these states. Their interference with the incident waves can be recorded as spatial oscillations of the LDOS in STM topographs close to steps [130–132]. This system can be treated as a two-dimensional electron gas scattered by a barrier. In the presence of a scatterer, the charge density $\rho(r)$ is the sum over all occupied states as

$$\rho(r) = e \sum_{|k|<k_F} |\Psi_k(r)|^2. \tag{5.2}$$

Friedel showed the result of this summation are standing waves known as Friedel oscillations [133]. The local density of states for this 2D gas at step edges has the form of [134]

$$\rho_{2D} = L_0\big[1 - rJ_0(2kx)\big] \tag{5.3}$$

where J_0 is the zero-order Bessel function, $k = \sqrt{2m^*E}/\hbar$, and $L_0 = m^*/\pi\hbar^2$ is the surface LDOS without any scatterer nearby.

In 2004, L. Limot measured the Kondo resonance of Co adatom at three different distances (8, 13 and 24 Å) from a step edge of Ag(111). Using equation (5.3), ρ_s varied in the order of three in his manipulation process. At the distance of $\approx$ 8 Å from the step edge, ρ_s was $\approx$ 0.5 increased to $\approx$ 1.5 for 24 Å. He observed the same Kondo temperature for the adatom at different distances from the step edge. He concluded the Kondo effect is mostly originated from the interaction between the magnetic adatom and bulk electrons of the host metal [127].

In 2018, the group of Q. Li measured the width of Kondo resonance for the same system. Their results showed a clear role of surface state electrons in the Kondo effect. According to their findings, the LDOS oscillations close to the step edge led to the variation of the Kondo resonance width in the order of three. Moreover, they observed the resonance width variation has the same oscillation period as the half Fermi wavelength of the Ag(111) surface state [129]. These contradictory observations motivated us to study this effect for the Co adatoms on Cu(111).

5.2 Kondo Effect of Co Adatoms Close to a Step Edge on Cu(111)

To compare our results with two previous contradictory observations, we also chose a step on Cu(111) surface to study the Kondo resonance of Co adatoms. Analysis of the spatial

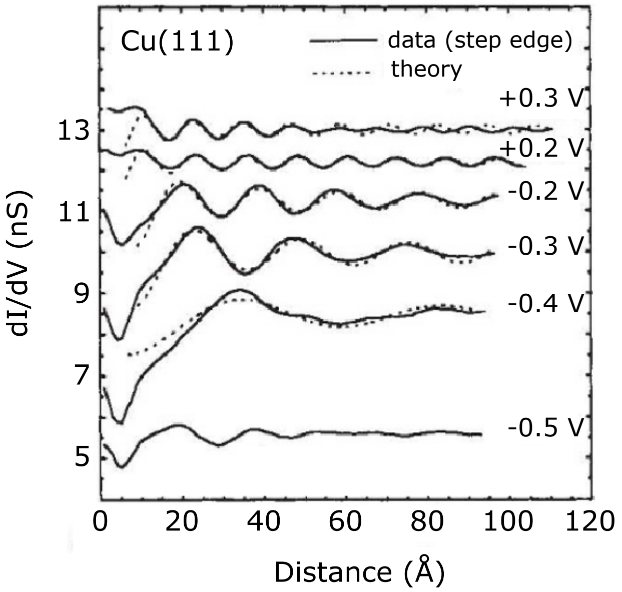

Figure 5.1: Measured (solid line) and calculated (dotted line) dI/dV as a function of distance from a Cu(111) step edge at different bias voltages. Adapted from [130].

LDOS oscillations for Cu(111) and other (111) metal surfaces were done previously. In 1993, using STM Crommie et al. observed these oscillations close to a Cu(111) step and measured dI/dV as a function of distance from the step edge at different bias voltages. He observed by increasing the energy above Fermi energy, the wavelength of the oscillations decreases (figure 5.1) [130].

In our experiment, the sample preparation and Co adatom evaporation were done as explained in sections (2.2) and (2.3). Figure 5.2 (a-i) shows topographs of nine manipulation processes where a Co adatom was positioned at different distances from a step edge. Figure 5.2 (j) is the top view of the same step region. From the height profile across the white dashed line in (j), the LDOS variation at the energy of 250 meV is visible (figure 5.2 (k)). Spectra of the differential conductance were measured using a lock-in modulation amplitude of 1 mV$_{\text{rms}}$. dI/dV spectra of Co atom at different distances from the step edge are shown in figure 5.2 (l). They showed the expected Kondo resonance close to the zero bias [66, 68, 69, 135]. To determine the intrinsic line-width of the resonances, we removed the broadening effects as explained in section (1.2.1) [18]. Fano fits were used to extract the resonance width which are shown as red lines in figure 5.2 (l).

5.2.1 Distance Determination

After each manipulation process, the distance of the Co atom from the step edge was determined. Since the step in the cross-section of the topographs was not straight, we used the mid-rise point (MR) to define its distance from the Co adatom. An example for the

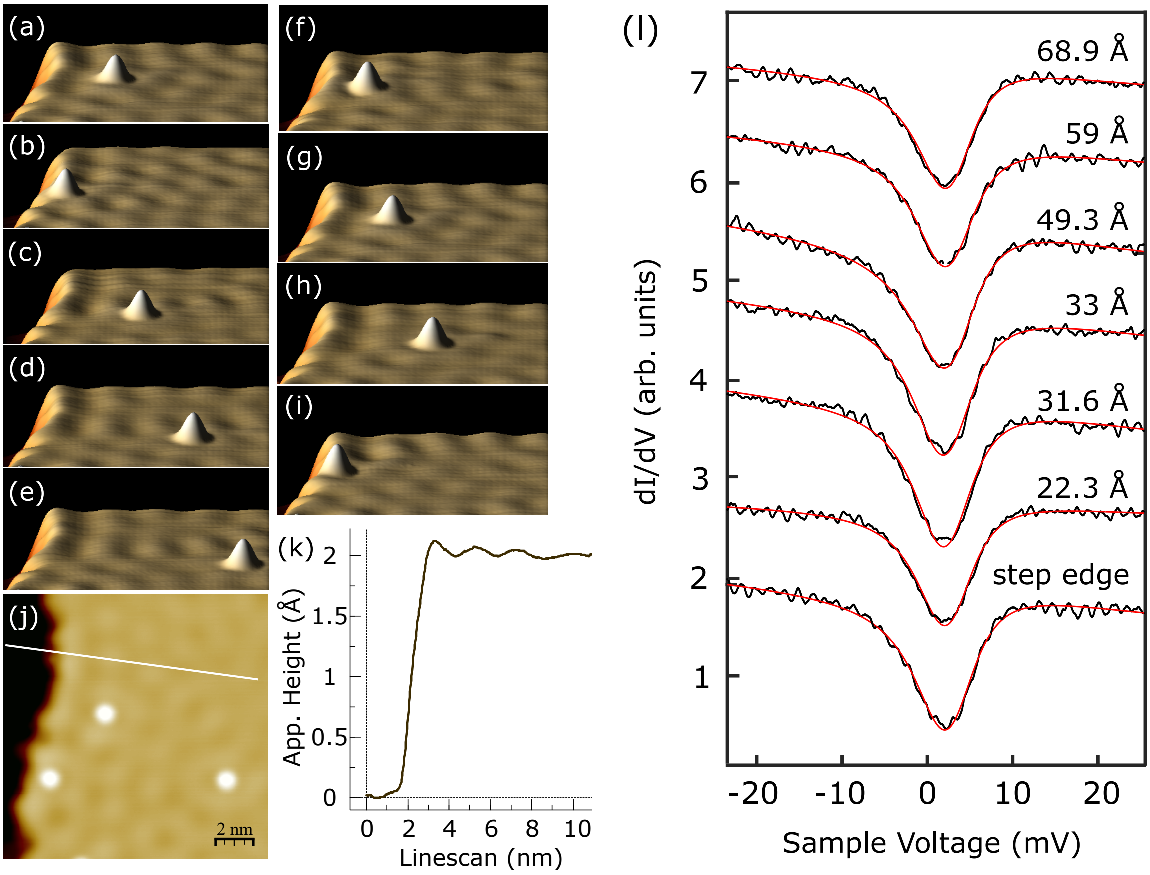

FIGURE 5.2: **(a-i)** STM images of a single Co atom manipulation process on Cu(111) (V = 250 mV and I = 30 pA). Co atom was positioned at different distances from the step edge and it has the apparent height of ≈ 60 pm. **(j)** Top view of the same step region (12.9 nm × 12.9 nm) to see the spatial oscillation of surface LDOS at 250 meV above Fermi energy. **(k)** Height profile across the white line in (j). **(l)** dI/dV spectra with their corresponding Fano fits (red lines) of the Co atom on Cu(111) terrace with different distances from the step edge. The current feedback was opened at V = 250 mV and I = 420 pA.

distance determination is shown in figure 5.3. Using the cross-section of the topograph in figure 5.3 (b), two lines were fitted with the lower and the upper terraces (horizontal green lines). A third line was adjusted with the rise of the step (red line). The intersections of the two horizontal lines (fitted with the terraces) and the third line were found (black dots). The middle point of these intersections was considered as the mid-rise point, MR (red dot). Finally, the adatom distance from the step edge was defined as the separation between the highest point of the adatom and the MR point. The obtained distances with this method were marked with red circles in figure 5.4.

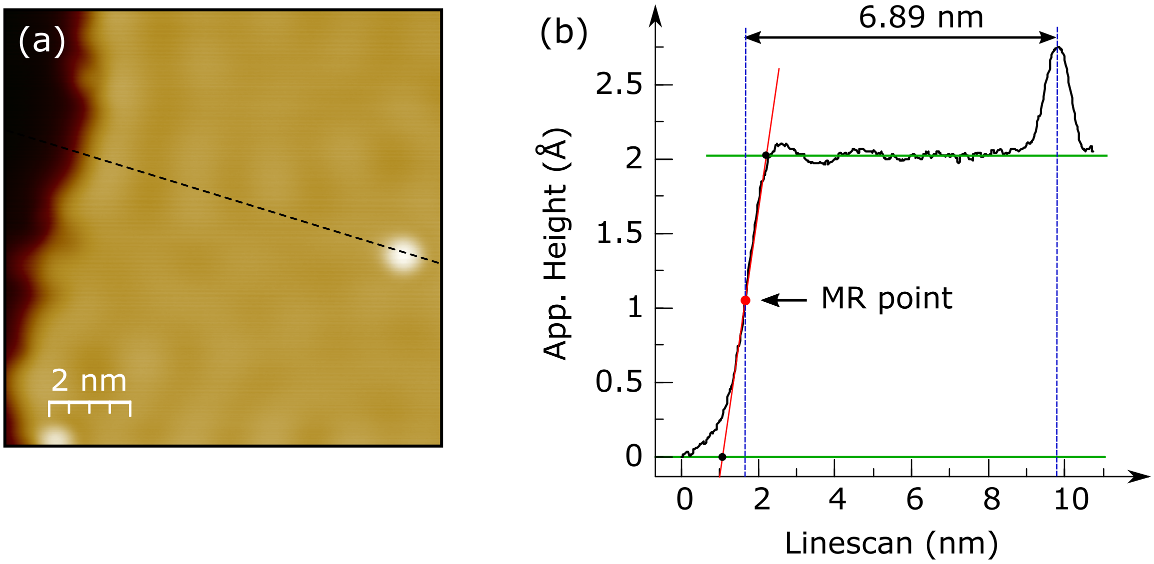

FIGURE 5.3: (a) STM image of Co adatom close to a step edge of Cu(111) surface (V = 250 mV and I = 30 pA). (b) cross-section along the dashed line in (a). The separation between the adatom and the step edge was measured from the maximum apparent height of the adatom to the mid-rise (MR) point of the step.

5.3 Results and Conclusion

The extracted resonance widths and the Kondo temperatures are listed in table (5.1). The maximum variation of the resonance width was found to be $\approx 10\%$. To find out the observed $\approx 10\%$ variation of resonance width corresponds to how much variation in LDOS, we need to see LDOS oscillation at the energy window of the effect under investigation (Fermi energy for the Kondo effect).

Considering the values $m^* = 0.412\ m_e$, $r = 0.5$, and $k_F = 0.215$ Å^{-1} for Cu(111) at the Fermi energy and using equation (5.3), the oscillations can be calculated as [134]

$$\rho \approx \frac{0.412\ m_e}{\pi \hbar^2}\left[1 - 0.5 \times \frac{Sin(2 \times 0.215\ x)}{2 \times 0.215\ x}\right] \tag{5.4}$$

which are shown in figure 5.4. The positions of the Co adatom extracted with the mid-rise definition are shown as red dots. We also shifted all extracted positions by ±1 Å and ±2 Å to consider a possible uncertainty in the distance determination. In our manipulation,

TABLE 5.1: Extracted values of the half width half maximum (Γ) and Kondo temperature for different distances from the step edge. The maximum variation of $\approx 10\%$ was observed in the width of the resonance.

d (nm)	step edge	1.65	2.4	2.6	4.15	5.9	7.6
Γ (mV)	4	3.7	3.9	4.1	4	4	3.7
T_K (K)	46	43	45	47.5	46	46	43

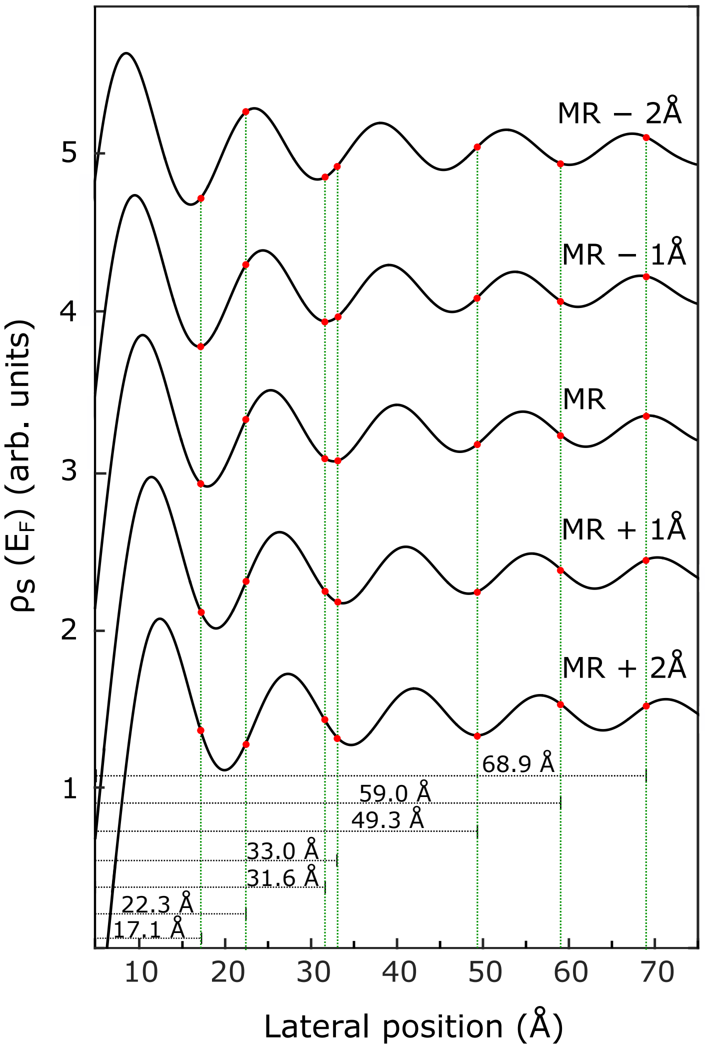

FIGURE 5.4: Simulated ρ_s oscillations at Fermi energy as a function of the distance from a Cu(111) step edge. Red dots show the Co atom positions in our experiment. The distances from the step were defined according to figure 5.3.

the first two points close to the step edge were the positions at which the Co adatom experienced the maximum ρ_s variation. In figure 5.4, for the MR oscillations, the Co atom at $x = 17.1$ Å was almost at a minimum of ρ_s and the atom at $x = 22.3$ Å was close to a peak. This observation is also true for the MR−1 Å and MR−2 Å cases.

For the MR+1 Å and MR+2 Å cases, ρ_s in the first two positions ($x = 17.1$ Å and $x = 22.3$ Å) does not vary like the other cases. However, in these cases the positions with $x = 49.3$ Å and $x = 59$ Å are close to a maximum and a minimum of the oscillations, respectively.

The Kondo resonance of the first two points close to the step edge in MR oscillations are plotted on top of each other in figure 5.5(a). They overlap each other with a good accuracy. To illustrate the resonance width variation in the order of three, we simulated the same resonance with the Fano fit (black solid line in figure 5.5(b)) and increased the width of the resonance up to three times. With this simulation, one can compare the experimental results and the simulation for the order of three resonance width variation.

In conclusion, we observed for the Co on Cu(111), the Kondo resonance is not sensitive to the ρ_s variations and the surface state electrons do not have a strong impact on this many-body phenomenon.

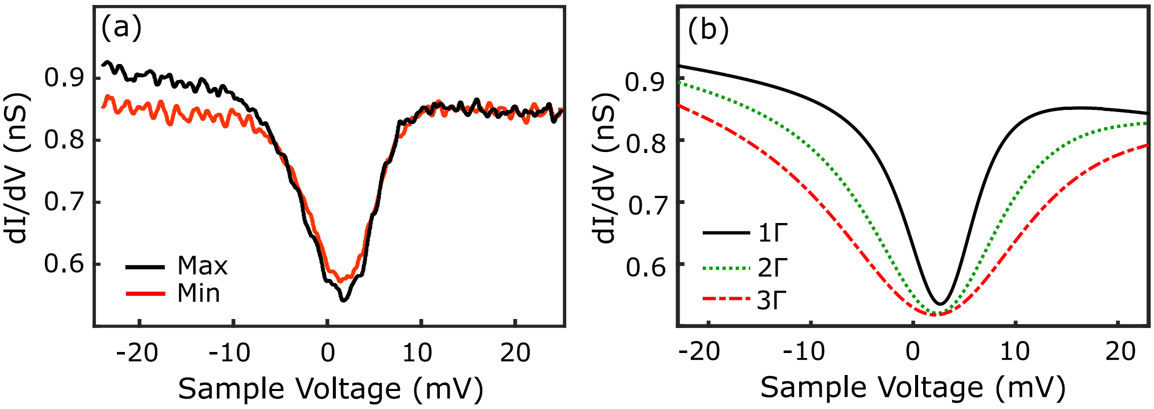

FIGURE 5.5: **(a)** Kondo resonances of Co atom positioned at a minimum and a maximum of ρ_s oscillations. Despite the maximum variation of ρ_s, the spectra overlay with a good accuracy. **(b)** Black solid line represents the simulated Fano fit for the resonance in (a). The width of resonance (Γ) was considered as the variable parameter and increased up to the order of three.

Chapter 6

Conclusion and Outlook

In summary, distinct line-shapes were observed in the tunneling spectra of Co atoms on Cu(111) flat terrace and attached to the Cu chains. The evolution of the observed feature for Co atom attached to the side of the chain in the presence of an external magnetic field demonstrates its inelastic origin. Breaking the symmetry of the adatom vicinity leads to anisotropy in the crystal field. DFT and QMC calculations predict a modified hybridization of the Co $3d$ orbitals upon its attachment to the chain. According to the calculations, the hybridization of the Co in-plane orbitals are modified by introducing the chain to its atomic environment. Further calculations are performing at the time of writing this thesis to include the SOC effect in the many-body calculations. The initial results demonstrate a significat effect of SOC in the orbital-resolved spectral function of Co adatom. These findings may provide a deeper insight into the spin-flip processes in such Kondo systems.

Usually due to the computational costs, the SOC is neglected in the many-body calculations of the Kondo systems such as QMC calculations [136]. Here, we showed how the SOC can compete with the Kondo effect to define the final spin state of the magnetic atom. The results demonstrate that a single orbital calculation of the Kondo effect without considering SOC may be unrealistic.

Mostly in STM measurements, nano-structures are fabricated by atom manipulation. Here we showed the potential of STM to fabricate interesting nano-structures in a much faster and reliable way. The fabricated chains and trenches provide an excellent playground to extend our understanding of the magnetic anisotropy and the Kondo effect. As a further outlook, other magnetic adatoms can be subjected to this spatial asymmetry. By a proper choice of the magnetic atom, it may be eventually possible to achieve a large magnetic anisotropy energy on metal surfaces.

Moreover, it is also interesting to investigate the interaction between molecules via these chains. Monatomic chains have an unoccupied state at approximately 1.5 eV. This state can

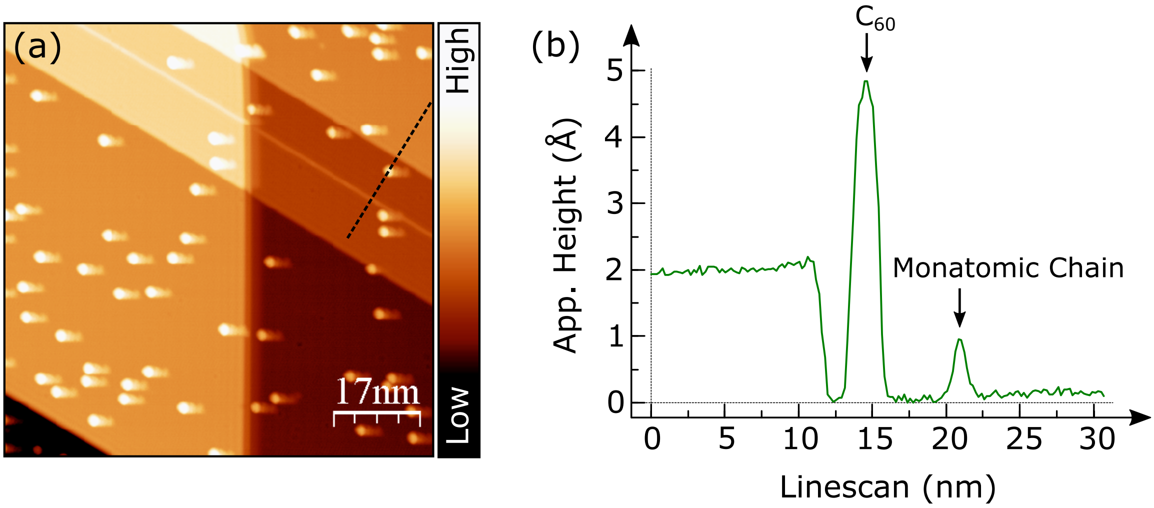

FIGURE 6.1: (a) STM topograph of deposited C_{60} molecules and a monatomic Cu chain on Cu(111) (V = 125 mV and I = 35 pA). The triplet image is due to the multiple tip asperities. (b) Height profile along the black dashed line in (a). The Monatomic Cu chain is approximately five time smaller than the C_{60} molecule in apparent height.

be used as a channel for coupling between molecules. Electronic and vibrational properties of C_{60} on Cu(111) were studied with STM [137]. Its STS spectrum has a broad peak at 1.8 eV which is attributed to its LUMO+1 molecular state. The overlap of this energy window with the relatively broad unoccupied state of the monatomic Cu chain at 1.5 eV offers the possibility of the coupling between C_{60} molecules mediated by these chains.

We had already fabricated $C_{60}Cu_m$ chains on Cu(111). Figure 6.1 (a) illustrates a topograph of a monatomic chain with deposited C_{60} molecules. The main experimental challenge was the manipulation of the molecules to these narrow chains. According to the height profile in figure 6.1 (b), C_{60} molecule is approximately five times larger in apparent height compared to the monatomic chain. This large difference makes the manipulation process less controllable.

As shown in figure 6.2, we were able to attach C_{60} to the wider chains. STS measurements were performed on a molecule on the (111) terrace, singly attached to the side of the wide chain, and after attaching two other C_{60} molecules to the chain. All the measurements were performed close to the center of the molecule. Upon attaching it to the wide chain, its unoccupied states at ≈ 0.8 eV and ≈ 2 eV were replaced with an state at ≈ 1.7 eV. Adding a second molecule to the chain weakened the 1.7 eV peak slightly. These initial results with C_{60} open promising perspectives for studying the coupling between other molecules via the chains with different widths.

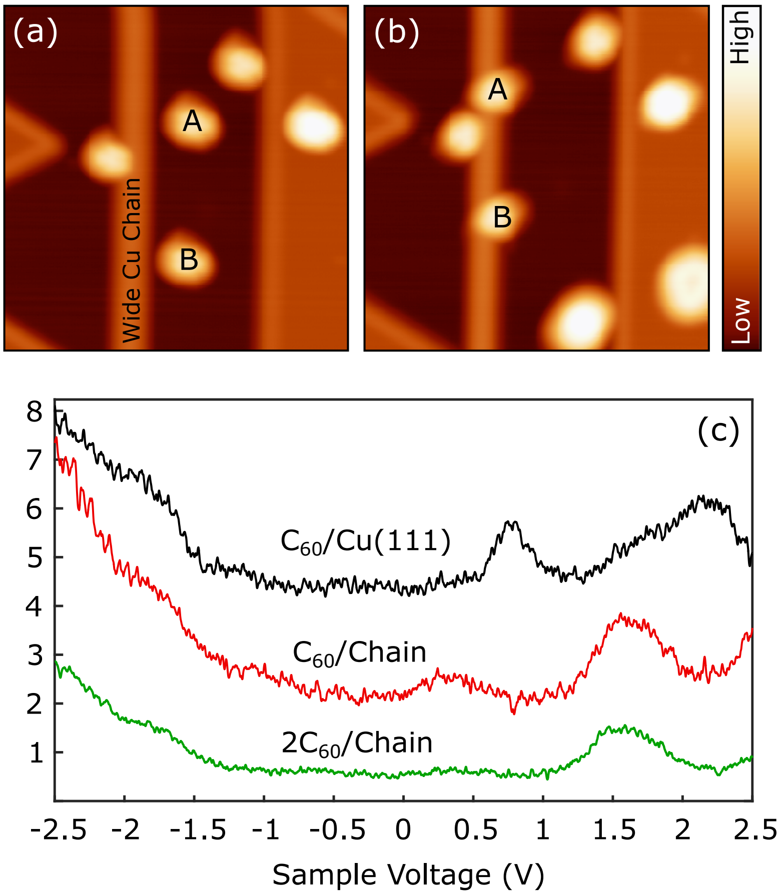

FIGURE 6.2: STM topographs of deposited C_{60} molecules and a wide Cu chain on Cu(111) (V = 10 mV and I = 25 pA). Molecules A and B were attached to the chain by atom manipulation (c) dI/dV spectra acquired on molecule A on (111) terrace, and attached to the chain before and after the molecule B attachment. The current feedback was opened at V = 2.5 V and I = 180 pA.

Appendix A

B-field Data Analysis

A.1 Tip Effect Removal

The tunneling current depends on the sample and the tip density of states (ρ_s and ρ_t). In most STS measurements, prior to recording dI/dV signals on the desired structure, in-situ tip preparation was performed to obtain a featureless dI/dV spectra on the bare surface. In this way, the features observed in the dI/dV spectra measured on the desired atomic structure can be attributed to that structure specifically.

However, in practice obtaining a completely featureless tip is a difficult task. The remaining features in the tip LDOS usually vary from tip to tip. They can even change during the measurement process. This becomes more concerning when the investigated feature is comparable with the remaining tip features. The inelastic excitations in the IETS spectra appear as steps of small intensity in a narrow energy window close to Fermi energy. To remove the tip effect from IETS signals, data treatment methods have been introduced. The tip LDOS can be approximated by the STS data obtained on a clean terrace. Its effect can be removed from the dI/dVs in two ways: subtraction or deconvolution of the tip LDOS from the measured signal on magnetic atom. The comparison between these two methods showed the recovered signals are almost identical and the discrepancy between the methods appears at high bias voltages (>300 mV) [138].

In our experiments with the 4 K STM, we removed large tip features by in-situ preparation. The small remaining features were in the range of mechanical noise level of the machine. Moreover, the Kondo resonances of Co adatoms on bare terrace were much stronger than the noise level. Due to the small intensity of the zero-centered resonance observed for Co atoms attached to the chain, we removed the tip effect from the measured dI/dV signals by the subtraction method. For each Co$_n$Cu$_m$ structure, we recorded the dI/dV signal on three different positions, namely on a clean area of the surface close to the chain, on the

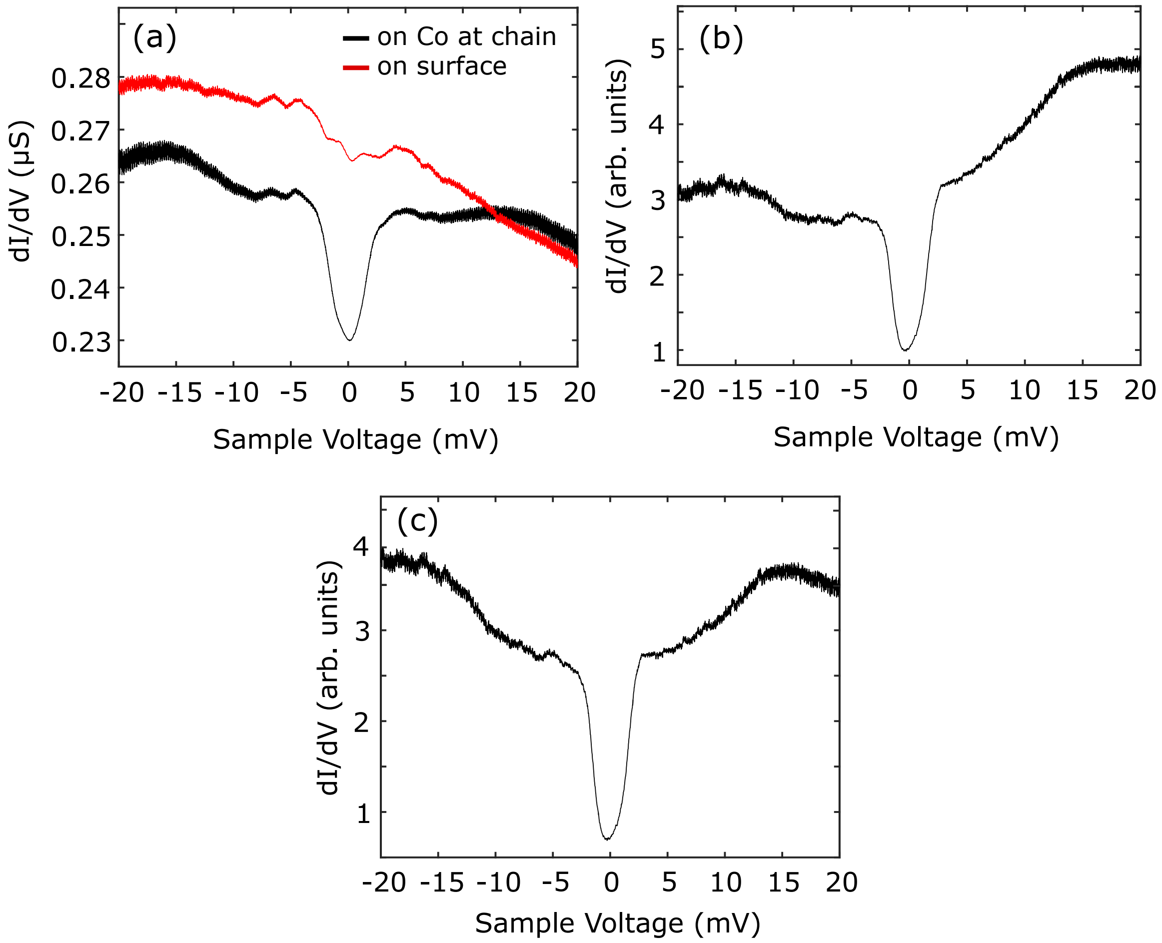

FIGURE A.1: (a) dI/dV spectra acquired on surface and on Co atom attached to a monatomic Cu chain. (b) dI/dV spectrum resulted from the subtraction of the surface spectrum and the spectrum of the Co at chain (subtraction of the two spectra in (a)). (c) Final spectrum after removal of the linear background from (b). The current feedback was opened at V = 20 mV and I = 5 nA.

chain, and on the Co atom attached to the chain. We observed no difference in the spectra of the clean surface and the chain (without Co atom). In our experiments with the mK STM, despite several tip in-situ treatments, the tip spectrum was often structured close to Fermi energy. To illustrate the background removal procedure of our data, we chose a measurement where the tip had clear features. Figure A.1(a) shows the spectra acquired on the surface and on the Co atom at the chain. The tip contribution was removed by subtracting the surface spectrum from the Co spectrum (figure A.1(b)). The two original spectra in figure A.1(a) were acquired on two different positions on the surface and as a result, they are tilted with different slopes (also for the Co adatoms on Cu(111) shown in figure 2.5(a)). These linear background slopes can be removed before or after the subtraction. Here we removed the linear background after subtraction (figure A.1(c)). The subtraction method was performed on spectra of more that 10 atoms measured with at least 4 tips and regardless of the tip structure, the resolved inelastic signals (figure A.1(c)) were always identical and reproducible.

A.2 Noise Removal

Despite the great instrumentation efforts to eliminate noise sources in STM, still mechanical vibrations may appear in the dI/dV signals. Most of the data presented in this thesis were obtained in low-noise conditions. However, in few cases we measured signals which were distorted by noise. To restore the noise-free signal from the original signal, we applied FFT-filtering. Figure A.2 illustrates an original spectrum and the FFT-filtered signal. The main features of the spectrum were not affected by the filtering and only the high frequency noise was removed from it. In the main text, the spectra subjected to FFT-filtering are pointed out in the figure captions.

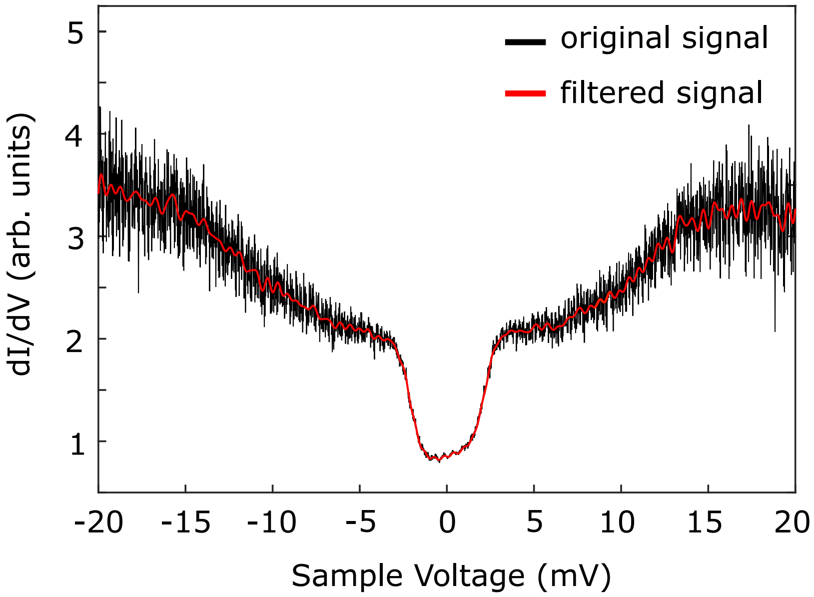

FIGURE A.2: dI/dV signal obtained on a Co atom attached to the side of a monatomic chain in the presence of applied out-of-plane magnetic field B_Z=8 T. Using FFT-filtering, the high frequency noise was removed from the original signal.

Bibliography

[1] J. Kondo. Resistance minimum in dilute magnetic alloys. *Prog. Theor. Phys.*, 32:37, 1964.

[2] A. J. Heinrich, J. A. Gupta, C. P. Lutz, and D. M. Eigler. Single-atom spin-flip spectroscopy. *Science*, 306:466–469, 2004.

[3] M. Ternes. Spin excitations and correlations in scanning tunneling spectroscopy. *New J. Phys.*, 17:063016, Jun. 2015.

[4] A. Otte, M. Ternes, K. von Bergmann, S. Loth, H. Brune, C. Lutz, C. Hirjibehedin, and A. Heinrich. The role of magnetic anisotropy in the Kondo effect. *Nat. Phys.*, 4:847–850, 2008.

[5] C. F. Hirjibehedin and et al. Large magnetic anisotropy of a single atomic spin embedded in a surface molecular network. *Science*, 317:11991203, 2007.

[6] S. Loth, C. P. Lutz, and A. J. Heinrich. Spin-polarized spin excitation spectroscopy. *New J. Phys.*, 12:125021, 2010.

[7] I. G. Rau, S. Baumann, S. Rusponi, F. Donati, S. Stepanow, L. Gragnaniello, J. Dreiser, C. Piamonteze, F. Nolting, S. Gangopadhyay, O. R. Albertini, R. M. Macfarlane, C. P. Lutz, B. A. Jones, P. Gambardella, A. J. Heinrich, and H. Brune. Reaching the magnetic anisotropy limit of a 3 d metal atom. *Science*, 344(6187):988–992, 2014.

[8] J. Bardeen. Tunnelling from a many-particle point of view. *Phys. Rev. Lett.*, 6(2):57–59, Apr. 1961.

[9] J Tersoff and D. R. Hamann. Theory and application for the scanning tunneling microscope. *Phys. Rev. Lett.*, 50:1998, 1983.

[10] J. Tersoff and D. R. Hamann. Theory of the scanning tunneling microscope. *Phys. Rev. B*, 31:805, Jan. 1985.

[11] D. Bonnell. *Scanning Probe Microscopy and Spectroscopy. Theory, Techniques, and Applications.* Wiley-VCH, New York, United States, 2nd edition, 2001.

[12] A. Selloni, P. Carnevali, E. Tosatti, and C. D. Chen. Voltage-dependent scanning tunneling microscopy of a crystal surface: Graphite. *Phys. Rev. B*, 31:2602, 1985.

[13] C. Chen. *Introduction to scanning tunneling microscopy.* Oxford University Press, New York, 2nd edition, 2008.

[14] M Ziegler, N. Néel, A. Sperl, J. Kröger, and R Berndt. Local density of states from constant-current tunneling spectra. *Phys. Rev. B*, 80, 2009.

[15] J. G. Simmons. Electric tunnel effect between dissimilar electrodes separated by a thin insulating film. *J. Appl. Phys.*, 34(9):2581, Sep. 1963.

[16] Samir Lounis. Theory of scanning tunneling microscopy. *arXiv preprint arXiv:1404.0961*, 2014.

[17] V. A. Ukraintsev. Data evaluation technique for electron-tunneling spectroscopy. *Phys. Rev. B*, 53:11176, 1996.

[18] M. Gruber, A. Weismann, and R. Berndt. The Kondo resonance line shape in scanning tunnelling spectroscopy: Instrumental aspects. *J. Phys.: Condens. Matter*, 30:424001, 2018.

[19] M. Ziegler. Exploring structural, electronic, magnetic, and vibrational properties of nanostructures with a scanning tunneling microscope. *PhD thesis, der Christian-Albrechts-Universität zu Kiel*, Dec. 2009.

[20] J. Lambe and R. C. Jaklevic. Molecular vibration spectra by inelastic electron tunneling. *Phys. Rev.*, 165:821, Jan. 1968.

[21] S. Kahle. Magnetic properties of individual molecules studied by scanning tunneling microscopy. *PhD. thesis*, Jan. 2013.

[22] J. Klein, A. Leger, M. Belin, D. Dfourneau, and M. J. L. Sangster. Inelastic electron-tunneling spectroscopy of metal-insulator-metal junctions. *Phys. Rev. B*, 7:2336, Mar. 1973.

[23] S. Katano, Y. Kim, Y. Kagata, and M. Kawai. Single-molecule vibrational spectroscopy and inelastic-tunneling-electron-induced diffusion of formate adsorbed on Ni(110). *J. Phys. Chem. C*, 114:3003–3007, Feb. 2010.

[24] W. Wang and C. A. Richter. Spin-polarized inelastic electron tunneling spectroscopy of a molecular magnetic tunnel junction. *Appl. Phys. Lett.*, 89:153105–3, Feb. 2006.

[25] J. P. Gauyacq, N. Lorente, and F. D. Novaes. Excitation of local magnetic moments by tunneling electrons. *Progress in Surface Science*, 87:63–107, 2012.

[26] D. J. Scalapino and S. M. Marcus. Tunnelling from a many-particle point of view. *Phys. Rev. Lett.*, 18:459, Mar. 1967.

[27] D. J. Griffiths. *Introduction to Quantum Mechanics*. Pearson Prentice Hall, 2nd edition, 2004.

[28] A. Abragam and B. Blaeney. *Electron Paramagnetic Resonance of Transition Ions*. Clarendon Press, Oxford, 1986.

[29] D. Gatteschi, R. Sessoli, and J. Villain. *Molecular Nanomagnets*. Oxford University Press, New York, 2006.

[30] J. J. van Vleck. On the anisotropy of cubic ferromagnetic crystals. *Phys. Rev.*, 52:1178, Dec. 1937.

[31] P. Bruno. Tight-binding approach to the orbital magnetic moment and magnetocrystalline anisotropy of transition-metal monolayers. *Phys. Rev. B*, 39:865, 1989.

[32] P. Bruno. Magnetismus von Festkrörpern und Grenzrächen Ferienkurse des Forschungszentrums Jülich. 1993.

[33] L. Néel. *J. Phys. Radium*, 15:225 – 239, 1954.

[34] M. Ternes, A. J. Heinrich, and W. D. Schneider. Spectroscopic manifestations of the Kondo effect on single adatoms. *J. Phys.: Condens. Matter*, 21:053001, 2009.

[35] A. A. Khajetoorians and et al. Current-driven spin dynamics of artificially constructed quantum magnets. *Science*, 339:55–59, Jan. 2013.

[36] N. Tsukahara and et al. Adsorption-induced switching of magnetic anisotropy in a single Iron(II) Phthalocyanine molecule on an oxidized Cu(110) surface. *Phys. Rev. Lett.*, 102:167203, Apr. 2009.

[37] F. Donati, Q. Dubout, G. Auts, F. Patthey, F. Calleja, P. Gambardella, O. V. Yazyev, and H. Brune. Magnetic moment and anisotropy of individual Co atoms on graphene. *Phys. Rev. Lett.*, 111:236801, Dec. 2013.

[38] B. Bryant, A. Spinelli, J. J. T. Wagenaar, M. Gerrits, and A. F. Otte. Local control of single atom magnetocrystalline anisotropy. *Phys. Rev. Lett.*, 111:127203, Sep. 2013.

[39] D. Dai, H. Xiang, and M. H. Whangbo. Effects of spin-orbit coupling on magnetic properties of discrete and extended magnetic systems. *J Comput Chem.*, 29:21872209, 2008.

[40] T. Balashov and et. al. Magnetic anisotropy and magnetization dynamics of individual atoms and clusters of Fe and Co on Pt(111). *Phys. Rev. Lett.*, 102:257203, Jun. 2009.

[41] A. A. Khajetoorians, T. Schlenk, B. Schweflinghaus, M. dos Santos Dias, M. Bouhassoune, S. Lounis, J. Wiebe, and R. Wiesendanger. Spin excitations of individual Fe atoms on Pt(111): impact of the site-dependent giant substrate polarization. *Phys. Rev. Lett.*, 111:157204, Oct. 2013.

[42] A. A. Khajetoorians, S. Lounis, B. Chilian, A. T. Costa, L. Zhou, D. L. Mills, J. Wiebe, and R. Wiesendanger. Itinerant nature of atom-magnetization excitation by tunneling electrons. *Phys. Rev. Lett.*, 106:037205, Jan. 2011.

[43] B. Chilian, A. A. Khajetoorians, S. Lounis, A. T. Costa, D. L. Mills, J. Wiebe, and R. Wiesendanger. Anomalously large g factor of single atoms adsorbed on a metal substrate. *Phys. Rev. B*, 84:212401, Dec. 2011.

[44] T. Schuh, T. Miyamachi, S. Gerstl, M. Geilhufe, M. Hoffmann, S. Ostanin, W. Hergert, A. Ernst, and W. Wulfhekel. Magnetic excitations of rare earth atoms and clusters on metallic surfaces. *Nano Lett.*, 12:4805–4809, Aug. 2012.

[45] M. Persson. Theory of inelastic electron tunneling from a localized spin in the impulsive approximation. *Phys. Rev. Lett.*, 103:050801, Jul. 2009.

[46] N. Lorente and J. P. Gauyacq. Efficient spin transitions in inelastic electron tunneling spectroscopy. *Phys. Rev. Lett.*, 103:176601, Oct. 2009.

[47] J. P. Gauyacq, F. D. Novaes, and N. Lorente. Magnetic transitions induced by tunneling electrons in individual adsorbed M-phthalocyanine molecules (M =Fe and Co). *Phys. Rev. B*, 81:165423, Apr. 2010.

[48] A. Hurley, N. Baadji, and S. Sanvito. Spin-flip inelastic electron tunneling spectroscopy in atomic chains. *Phys. Rev. B*, 84:035427, Jul. 2011.

[49] P. W. Anderson. Localized magnetic states in metals. *Phys. Rev.*, 124:41, 1961.

[50] J. R. Schrieffer and P. A. Wolff. Relation between the Anderson and Kondo Hamiltonians. *Phys. Rev.*, 149:491, Sep. 1966.

[51] L. D. Landau. The theory of a Fermi liquid. *Sov. Phys. JETP*, 3:920925, 1957.

[52] L. D. Landau. Oscillations in a Fermi liquid. *Sov. Phys. JETP*, 5:101108, 1957.

[53] J. M. Ziman. *Electrons and Phonons.* Clarendon Press, Oxford, 1960.

[54] J. Patterson and B. C. Bailey. *Solid-State Physics: Introduction to the Theory, Second Edition.* Springer-Verlag Berlin Heidelberg, 2010.

[55] J. R. Chelikowsky and S. G. Louie. *Quantum theory of real materials.* Kluwer Academic Publishers, Boston, 1996.

[56] A. Bid, A. Bora, and A. K. Raychaudhuri. Temperature dependence of the resistance of metallic nanowires of diameter $\geqslant 15$ nm: Applicability of Bloch-Grüneisen theorem. *Phys. Rev. B*, 74:035426, Jul. 2006.

[57] D. K. C. MacDonald. *Electrical conductivity of metals and alloys at low temperatures.* Springer, Berlin, 1956.

[58] E. Hildebrand. Zum Dia- und Paramagnetismus in metallischen Mischkristallreihen. Das Verhalten von gelöstem Kobalt und Rhodium. *Ann. d. Physik*, 30:593, 1937.

[59] H. C. Manoharan, C. P. Lutz, and D. M. Eigler. Quantum mirages formed by coherent projection of electronic structure. *Nature*, 403:512, Feb. 2000.

[60] U. Fano. Effects of configuration interaction on intensities and phase shifts. *Phys. Rev.*, 124:1866, 1961.

[61] M. Plihal and J. W. Gadzuk. Nonequilibrium theory of scanning tunneling spectroscopy via adsorbate resonances: nonmagnetic and Kondo impurities. *Phys. Rev. B*, 63:085404, Feb. 2001.

[62] H. O. Frota. Shape of the Kondo resonance. *Phys. Rev. B*, 45:1096, 1992.

[63] H. O. Frota and L. N. Oliveira. Photoemission spectroscopy for the spin-degenerate Anderson model. *Phys. Rev. B*, 33:7871–7874, 1986.

[64] Henning Prüser, Martin Wenderoth, Piet E. Dargel, Alexander Weismann, Robert Peters, Thomas Pruschke, and Rainer G. Ulbrich. Long-range Kondo signature of a single magnetic impurity. *Nat. Phys.*, 7:203, 2011.

[65] Juba Bouaziz, Filipe Souza Mendes Guimarães, and Samir Lounis. A new view on the origin of zero-bias anomalies of co atoms atop noble metal surfaces. *arXiv preprint arXiv:2003.01746*, 2020.

[66] P. Wahl, L. Diekhöner, M. Schneider, L. Vitali, G. Wittich, and K. Kern. Kondo Temperature of Magnetic Impurities at Surfaces. *Phys. Rev. Lett.*, 93:176603, 2004.

[67] M. A. Schneider, P. Wahl, L. Diekhöner, L. Vitali, G. Wittich, and K. Kern. Kondo effect of Co adatoms on Ag monolayers on noble metal surfaces. *Jpn. J. Appl. Phys.*, 44:5328, 2005.

[68] N. Néel, J. Kröger, R. Berndt, T. O. Wehling, A. I. Lichtenstein, and M. I. Katsnelson. Controlling the Kondo effect in CoCu_n clusters atom by atom. *Phys. Rev. Lett.*, 101:266803, 2008.

[69] N. Néel, R. Berndt J. Kröger, , T. O. Wehling, A. I. Lichtenstein, and M. I. Katsnelson. Two-site Kondo effect in atomic chains. *Phys. Rev. Lett.*, 107:106804, 2011.

[70] E. Wigner and J. Bardeen. Theory of the work function of monovalent metals. *Phys. Rev.*, 48:8487, Jul. 1935.

[71] J. Hölzl, F. K. Schulte, and Wagner H. *Work Function of Metals./ Physical and Chemical Properties of Stepped Surfaces*, volume 85. Springer, Berlin, Heidelberg, 1979.

[72] C. Fall. Ab initio study of the work functions of elemental metal crystals. *PhD. thesis*, 1999.

[73] J. U Kliewer. Dynamics and manipulation of surface states. *PhD thesis, RWTH Aachen, Germany*, Dec. 2000.

[74] *Operating manual for USM1300-He3.* Unisoku Co., Ltd.

[75] I. Horcas, R. Fernández, J. M. Gómez-Rodríguez, J. Colchero, J. Gómez-Herrero, and A. M. Baro. A software for scanning probe microscopy and a tool for nanotechnology. *Rev. Sci. Instrum.*, 78:013705, 2007.

[76] F. Thibaudau and J. Cousty. On the shape of monatomic steps of copper surface in STM images. *Ultramicroscopy*, 42-44:511–514, 1992.

[77] R. Huang, Y. Sun, C. Du, T. Gao, Y. Wu, and V. Stepanyuk. STM-mediated atom motion: a Co atom and mixed $CoCu_n$ chains on a Cu(111) surface. *Eur. Phys. J. B*, 86:429, 2013.

[78] A. C. Hewson. *The Kondo Problem to Heavy Fermions.* Cambridge University Press, 2008.

[79] D. Hull and D. J. Bacon. *Introduction to Dislocations.* Elsevier, 2011.

[80] A. Sperl, J. Kröger, N. Néel, H. Jensen, R. Berndt, A. Franke, and E. Pehlke. Unoccupied states of individual silver clusters and chains on Ag(111). *Phys. Rev. B*, 77:085422, 2008.

[81] S. Fölsch, P. Hyldgaard, R. Koch, and K. H. Ploog. Quantum confinement in monatomic Cu chains on Cu(111). *Phys. Rev. Lett.*, 92(5):056803, Feb. 2004.

[82] J. Repp, G. Meyer, K. H. Rieder, and P. Hyldgaard. Site determination and thermally assisted tunneling in homogenous nucleation. *Phys. Rev. Lett.*, 91:206102, Nov. 2003.

[83] I. Shim and K. A. Gingerich. Interaction between two Co atoms. An all electron ab initio HF-CI investigation. *J. Chem. Phys.*, 78:5693, 1983.

[84] H. Beckmann and G. Bergmann. Success and failure of the Friedel-Anderson resonance model for magnetic impurities: 3d impurities on the surface of Au. *Phys. Rev. B*, 54:368, 1996.

[85] J. Shi, S. Gider, K. Babcock, and D. D. Awschalom. Magnetic clusters in molecular beams, metals, and semiconductors. *Science*, 271:937, 1996.

[86] K. Yoshida. *Theory of Magnetism.* Springer, New York, 1996.

[87] Jonathan R. Friedman, M. P. Sarachik, J. Tejada, and R. Ziolo. Macroscopic measurement of resonant magnetization tunneling in high-spin molecules. *Phys. Rev. Lett.*, 76:3830, 1996.

[88] W. Chen, T. Jamneala, V. Madhavan, and M. F. Crommie. Disappearance of the Kondo resonance for atomically fabricated cobalt dimers. *Phys. Rev. B*, 60:8529, 1999.

[89] J. Stöhr and H. C. Siegmann. *Magnetism From Fundamentals to Nanoscale Dynamics.* Springer-Verlag Berlin Heidelberg, 2006.

[90] H. Brune and P. Gambardella. Magnetism of individual atoms adsorbed on surfaces. *Surface Science*, 603:1812–1830, Jun. 2009.

[91] R. Mozara. private communication. Nov. 2017.

[92] N. Noei, A. Weismann, and R. Berndt. Apparent tunneling barrier height and local work function of atomic arrays. *Beilstein J. Nanotechnol.*, 9:30483052, Dec. 2018.

[93] G. Binnig, H. Rohrer, C. Gerber, and E. Weibel. Surface studies by scanning tunneling microscopy. *Phys. Rev. Lett.*, 49(1):57, Jul. 1982.

[94] G. Binnig and H. Rohrer. Scanning tunneling microscopy. *Surf. Sci.*, 126(1-3):236, Mar. 1983.

[95] F. Seitz. *Modern Theory of Solids.* McGraw-Hill, 1940.

[96] N. D. Lang and W. Kohn. Theory of metal surfaces: Work function. *Phys. Rev. B*, 3(4):1215, Feb. 1971.

[97] R. Smoluchowski. Anisotropy of the electronic work function of metals. *Phys. Rev.*, 60(9):661, Nov. 1941.

[98] K. Besocke, B. Krahl-Urban, and H. Wagner. Dipole moments associated with edge atoms; a comparative study on stepped Pt, Au and W surfaces. *Surf. Sci.*, 68:39, Nov. 1977.

[99] K. Wandelt. The local work function: Concept and implications. *Appl. Surf. Sci.*, 111:1, Feb. 1997.

[100] J. G. Simmons. Generalized formula for the electric tunnel effect between similar electrodes separated by a thin insulating film. *J. Appl. Phys.*, 34(6):1793, Jun. 1963.

[101] G. Binnig, N. Garcia, H. Rohrer, J. M. Soler, and F. Flores. Electron-metal-surface interaction potential with vacuum tunneling: Observation of the image force. *Phys. Rev. B*, 30(8):4816, Oct. 1984.

[102] M. Becker and R. Berndt. Influence of band structure on the apparent barrier height in scanning tunneling microscopy. *Phys. Rev. B*, 81(3):035426, Jan. 2010.

[103] M. Becker and R. Berndt. Contrast inversion of the apparent barrier height of Pb thin films in scanning tunneling microscopy. *Appl. Phys. Lett.*, 96(3):033112, Jan. 2010.

[104] J. M. Pitarke, P.M. Echenique, , and F. Flores. Apparent barrier height for tunneling electrons in STM. *Surf. Sci.*, 217(1-2):267, Jul. 1989.

[105] N. D. Lang. Apparent barrier height in scanning tunneling microscopy. *Phys. Rev. B*, 37(17):10395, Jun. 1988.

[106] J. F. Jia, K. Inoue, Y. Hasegawa, W. S. Yang, and T. Sakurai. Variation of the local work function at steps on metal surfaces studied with STM. *Phys. Rev. B*, 58(3):1193, Jul. 1998.

[107] M. Sasaki and S. Yamamoto. Localized and delocalized features of microscopic work functions. *J. Vac. Soc. Jap.*, 50(5):313, 2007.

[108] M. Herz, Ch. Schiller, F. J. Giessibl, and J. Mannhart. Simultaneous current-, force-, and work-function measurement with atomic resolution. *Appl. Phys. Lett.*, 86(15):153101, Apr. 2005.

[109] S. J. Altenburg and R. Berndt. Local work function and STM tip-induced distortion of graphene on Ir(111). *New J. Phys.*, 16(5):053036, May 2014.

[110] Thomas Ihn. *Semiconductor Nanostructures.* Oxford University Press, Nov. 2009.

[111] L. Limot, J. Kröger, R. Berndt, A. Garcia-Lekue, and W.A. Hofer. Atom transfer and single-adatom contacts. *Phys. Rev. Lett.*, 94(12):126102, Apr. 2005.

[112] A. Garcia-Lekue and L. W. Wang. Plane-wave-based electron tunneling through Au nanojunctions: Numerical calculations. *Phys. Rev. B*, 82(3):035410, Jul. 2010.

[113] T. Fauster and W. Steinmann. *Electromagnetic Waves: Recent Developments in Research*, volume Vol.2: Photonic Probes of Surfaces. Elsevier, 1995. Chap. 8.

[114] G. Binnig and H. Rohrer. Scanning tunneling microscopy. *IBM J. Res. Dev.*, 30(4):355, 1986.

[115] L. C. Davis, M. P. Everson, R. C. Jaklevic, and Weidian Shen. Theory of the local density of surface states on a metal: Comparison with scanning tunneling spectroscopy of a Au(111) surface. *Phys. Rev. B*, 43:382, 1991.

[116] J. A. Verges and E. Louis. Electron states on the (111) surface of copper. *Sol. State Comm.*, 22:663, 1977.

[117] F. Reinert, G. Nicolay, S. Schmidt, D. Ehm, and S. Hüfner. Direct measurements of the l-gap surface states on the (111) face of noble metals by photoelectron spectroscopy. *Phys. Rev. B*, 63:115415, Mar. 2001.

[118] H. Lüth. *Solid Surfaces, Interfaces and Thin Films.* Springer, Berlin, Heidelberg, 2001.

[119] A. Euceda, D. M. Bylander, and L. Kleinman. Self-consistent electronic structure of 6- and 18-layer Cu(111) films. *Phys. Rev. B*, 28:528, Jul. 1983.

[120] V. Madhavan, W. Chen, T. Jamneala, M. F. Crommie, and Ned S. Wingreen. Local spectroscopy of a Kondo impurity: Co on Au(111). *Phys. Rev. B*, 64:165412, Oct. 2001.

[121] Nikolaus Knorr, M. Alexander Schneider, Lars Diekhöner, Peter Wahl, and Klaus Kern. Kondo effect of single Co adatoms on Cu surfaces. *Phys. Rev. Lett.*, 88:096804, 2002.

[122] Q. Li, S. Yamazaki, T. Eguchi, H. Kim, J. Kahng, F. Jia, Q. K. Xue, and Y. Hasegawa. Direct evidence of the contribution of surface states to the Kondo resonance. *Phys. Rev. B*, 80:115431, 2009.

[123] J. Merino and O. Gunnarsson. Role of surface states in scanning tunneling spectroscopy of (111) metal surfaces with Kondo adsorbates. *Phys. Rev. Lett.*, 93:156601, 2004.

[124] C. Y. Lin, A. H. Castro Neto, and B. A. Jones. First-principles calculation of the single impurity surface Kondo resonance. *Phys. Rev. Lett.*, 97:156102, 2006.

[125] C. Y. Lin, A. H. Castro Neto, and B. A. Jones. Microscopic theory of the single impurity surface Kondo resonance. *Phys. Rev. B*, 71:035417, 2005.

[126] M. A. Schneider, L. Vitali, N. Knorr, and K. Kern. Observing the scattering phase shift of isolated Kondo impurities at surfaces. *Phys. Rev. B*, 65:121406, 2002.

[127] L. Limot and R. Berndt. Kondo effect and surface-state electrons. *Appl. Surf. Sci.*, 237:576, 2004.

[128] M. Moro-Lagares, J. Fernández, P. Roura-Bas, M. R. Ibarra, A. A. Aligia, and D. Serrate. Quantifying the leading role of the surface state in the Kondo effect of Co/Ag(111). *Phys. Rev. B*, 97:235442, 2018.

[129] Q. L. Li, C. Zheng, R. Wang, R. X. Miao, B. F. andCao, L. Sun, D. Wu, Y. Z. Wu, S. C. Li, B. G. Wang, and H. F. Ding. Role of the surface state in the Kondo resonance width of a Co single adatom on Ag(111). *Phys. Rev. B*, 97:035417, 2018.

[130] M. F. Crommie, C. P. Lutz, and D. M. Eigler. Imaging standing waves in a two-dimensional electron gas. *Nature*, 363:526, 1993.

[131] Y. Hasegawa and P. Avouris. Direct observation of standing wave formation at surface steps using scanning tunneling spectroscopy. *Phys. Rev. Lett.*, 71:1071, 1993.

[132] O. Jeandupeux and D. Bürgi. Thermal damping of quantum interference patterns of surface-state electrons. *Phys. Rev. B*, 59:15926, 1999.

[133] J. Friedel. Metallic alloys. *Nuovo Cimento Suppl.*, 7:287–311, 1958.

[134] P. Avouris, I. W. Lyo, R. E. Walkup, and Y. Hasegawa. Real space imaging of electron scattering phenomena at metal surfaces. *J. Vac.Sci. Technol. B*, 12:1447, Jun. 1994.

[135] T. Uchihashi, J. Zhang, J. Kröger, and R. Berndt. Quantum modulation of the Kondo resonance of Co adatoms on Cu/Co/Cu(100). *Phys. Rev. B*, 78:033402, 2008.

[136] N. Néel, J. Kröger, M. Schrüler, B. Shao, T. O. Wehling, A. Kowalski, and G. Sangiovanni. Single-co Kondo effect in atomic Cu wires on Cu(111). *Phys. Rev. Research*, 2:023309, 2020.

[137] J. A. Larsson, S. D. Elliott, J. C. Greer, J. Repp, G. Meyer, and R. Allenspach. Orientation of individual C_{60} molecules adsorbed on Cu(111): Low-temperature scanning tunneling microscopy and density functional calculations. *Phys. Rev. B*, 77:115434, 2008.

[138] P. Wahl, L. Diekhöner, M. Schneider, and K. Kern. Background removal in scanning tunneling spectroscopy of single atoms and molecules on metal surfaces. *Rev. Sci. Instrum.*, 79:043104, 2008.

List of Figures

1.1 (a) Sketch of the energy-dependent DOS for a single *d* orbital on a metal surface. (b) Electron in *d* orbital can flip its spin with a bulk electron of opposite spin. The spin flip process can occur in two ways: *d* orbital of the adatom is filled with two electrons (process 1) or it is empty (process 2). Kondo resonance is generated close to the Fermi energy through this process. (c) Tunneling process from the probing tip to the metal. Adapted from Ref [34]. 16

1.2 Kondo resonance of Co adatom on Cu(111) measured with $V_{mod} = 1$ mV$_{rms}$ at T = 4.6 K fitted by Fano and Frota functions. Fano fit reproduces the Kondo resonance more accurately. The current feedback was opened at V = 250 mV and I = 440 pA. 17

2.1 Scanning tube-type piezo driver in mK STM machine [74]. 22

2.2 The overview of insert chamber components in mK STM machine [74]. . . . 23

2.3 (a) Constant current STM image of prepared Cu(111) with steps acquired at V = 100 mV and I = 36 pA (124.7 nm×124.7 nm). (b) The height profile along the dashed line in (a). It shows the step height of ≈ 200 pm. (c) STS data obtained on a Cu(111) flat terrace with its surface state at $V \approx -430$ mV. Current feedback was opened at V = 600 mV and I = 320 pA. 26

2.4 STM image of evaporated Co adatoms with apparent height of ≈ 60 pm on Cu(111) substrate. The image was acquired at V = 30 mV and I = 30 pA. 27

2.5 (a) Two measurements representing the Kondo resonances of two Co adatoms on different positions of a large Cu(111) terrace (black lines) and spectra at the same position of the surface in the absence of Co adatoms (green lines). The Kondo resonances show the similar background slopes as their corresponding spectra on the bare surface. Current feedback was opened at V = 20 mV and I = 500 pA. The spectra of measurement 2 are offset by 10 nS for clarity. Same tip was used for both measurements. The surface spectra are subjected to low-pass FFT-filtering for noise removal. (b) Kondo resonances of two Co adatoms measured with two different tips. The small overshoot of the resonance obtained with Tip 1 (red arrow) is interpreted as the higher tunneling probability of the electrons from the tip into the Kondo resonance. 28

3.1 Constant current images of (a) the tip indention area, (b) generated dislocations close to the indention area, and (c) fabricated long (up to 200 nm) copper chains on Cu(111). 30

3.2 (a) Constant current image (41.1 nm×41.1 nm) of a monatomic Cu chain on Cu(111) (V = 50 mV, I = 42 pA). (b) dI/dV spectra along a line perpendicular to the chain. Current feedback was opened at V = 3 V and I = 1.27 nA. 30

3.3 (a) Constant current image of two crossing chains with different widths on Cu(111) surface (left topograph: 65 nm×65 nm, V = 100 mV, I = 50 pA. Right topograph: 19.3 nm×19.3 nm, V = 60 mV, I = 47 pA). Green dots represent the STS measurement positions shown in figure 3.4. (b) Height profile along the white dashed-line in the right topograph. The two-atom wide chain has ≈ 175 pm apparent height and the crossing point has the apparent height of ≈ 275 pm. 31

3.4 STS data obtained on different positions of the structure shown in figure 3.3, namely on (a) the monatomic chain, the two-atom wide chain, and (b) the crossing position (measurement positions are shown as green dots in figure 3.3(a) right topograph). For the two-atom wide chain, the unoccupied state of the monatomic chain at ≈ 1.5 eV decreases in intensity and shifts downwards in energy (shown by red arrows). A sharp state at ≈ 3 eV was also observed for the crossing position. Current feedback was opened at V = 2.5 V and I = 800 pA for the monatomic and the two-atom wide chain and at V = 4 V and I = 800 pA for the measurement on the crossing position. 31

3.5 Manipulation process of Co adatoms to a monatomic chain. The manipulation directions are shown by arrows. Six Co atoms were attached to the chain from different sides and at different distances from each other. STM images were acquired at V = 30 mV and I = 30 pA (image size 19.8 nm×19.8 nm). 32

3.6 (a) Before and (b) after topographs of Co atom manipulation to the end of a Co_4Cu_m chain. Images were acquired at V = 30 mV and I = 54 pA (image size 15.2 nm×15.2 nm). 33

3.7 (a) Sketch of the Cu(111) surface illustrating the three different adsorption sites for a Co atom at the side of a fcc Cu chain. (b) Topograph of a monatomic Cu chain with Co atoms attached to its side (V = 30 mV, I = 28 pA, 20 nm×20 nm). During the manipulation, Co atoms were released at slightly different distances from the chain to study the possibility of obtaining the configurations shown in (a). 33

3.8 dI/dV spectra of Co atoms at three different positions namely on the (111) terrace, attached to the end of a Cu chain, and attached to the central part of a Cu chain. The data of Co at the central part of the chain exhibits depressions at ≈ ±10 mV indicated by arrows. While the energy of the resonance minimum for the end configuration is similar to the Co on terrace (≈ 3.3 mV), it was shifted to Fermi energy for the side configuration. For the spectroscopy on Co atom on terrace and at the end of the chain, the current feedback was opened at V = 30 mV and I = 70 pA and for Co atom attached to the side of the chain, it was opened at V = 30 mV and I = 110 pA. The spectrum from the end of the chain is offset by 0.5 nS for clarity. 34

3.9 (a-c) STM images of manipulating two single Co atoms to a two-atom wide Cu chain (V = 30 mV, I = 100 pA). White dashed circles show the positions of Co attachment. (d) dI/dV spectra acquired above the Co atom on (111) terrace and attached to the side of the wide chain. 35

3.10 dI/dV spectra of Co atom at the central part of a Cu chain in the presence of applied out of plane magnetic field, B_Z. A significant shift of the symmetric low energy steps by increasing the magnetic field was observed. The spectra were fitted by four Fermi functions shown as red lines. Current feedback was opened at V = 20 mV and I = 5 nA. The spectra of B_Z equal to 4, 8, and 9 T are subjected to FFT-filtering for noise removal. 37

3.11 Derivative of the dI/dV spectra in figure 3.10 for Co atom at the central part of a Cu chain in the presence of applied out-of-plane magnetic field, B_z. The inner steps positions in the dI/dV signal (Δ) appears as extrema in d^2I/dV^2. Its variation as a function of the magnetic field is shown in the inset. 38

3.12 dI/dV spectra of Co atom at the central part of a Cu chain in the presence of no external magnetic field, and applied magnetic field in the in-plane directions, B_x and B_y. Current feedback was opened at V = 20 mV and I = 5 nA. For the B_x direction, no change in the width of the resonance was observed, while its amplitude decreased by ≈ 10%. An increase of ≈ 13% in the width and ≈ 19% in the amplitude of the zero-centered resonance was observed when the magnetic field B_y =2 T was applied. 39

3.13 (a) Topograph of a monatomic Co_6Cu_n chain acquired at V = 30 mV, I = 30 pA and T = 4.6 K. Co atoms were attached to the Cu chain from different sides with separations ≈ 1.2 nm, ≈ 1.8 nm, and less than 6 Å. Dots represent the simulation for the adsorption sites of Cu chain and Co atoms at chain. Both Cu atoms of the chain and attached Co atoms are assumed to be at fcc sites of the surface. (b) Schematic plot of the simulation (dots in (a)) for adsorption sites of the Cu chain and the attached Co atoms. (c) Height profile along the white dots shown in (a). The closely attached Co_3 and Co_4 appeared as one single peak with an apparent height of approximately two times larger than the pairs with large separations. 40

3.14 (a) Constant current image of a monatomic Cu chain with two Co atoms attached to the same side of the chain with separation ≈ 1.5 nm (V = 30 mV, I = 40 pA). (b) dI/dV spectra of Co_1 before and after attaching Co_2 to the chain. No change of the Co_1 resonance line-shape was observed after attaching Co_2 to the chain. The current feedback was opened at V = 30 mV and I = 100 pA. 41

3.15 (a) Topograph of a Co_2Cu_n chain acquired at V = 20 mV, I = 1 nA, and T ≈ 400 mK. (b) Height profile along the dashed line in (a). The distance between Co atoms was ≈ 1.23 nm. (c) dI/dV spectra obtained on top of the Co atom in (a) in the presence of applied B_Z magnetic field up to 7 T. The current feedback was opened at V = 20 mV and I = 5 nA. Despite the presence of a second Co atom at the distance ≈ 1.23 nm at chain, both Co atoms showed the same behavior as a single Co atom at chain in the presence of an external B_Z field. At B_Z=7 T, the width of the central resonance increased by ≈ 38% and its amplitude decreased by ≈ 46% with respect to B_Z=1 T. The spectra of B_Z equal to 3 T and 7 T are subjected to FFT-filtering for noise removal. 42

3.16 (a) STM image of a monatomic Co_4Cu_n chain acquired at V = 58 mV and I = 50 pA. Co_1 and Co_2 were positioned similar to the (Co_3,Co_4) configuration in figure 3.13(c). (b) dI/dV spectra on Co_1 before and after attaching Co_2 to the chain. Current feedback was opened at V = 30 mV and I = 490 pA. For the closely-attached configuration, we observed a significant increase of the width and the amplitude of the central resonance by $\approx 61\%$ and $\approx 130\%$, respectively. Spectra labeled as (1), (2), and (3) were shifted by 1.5, 1, and 0.5 nS for clarity. 43

3.17 (a) dI/dV spectra obtained on top of Co atom in the closely-attached configuration (figure 3.16(a)) in the presence of applied magnetic field in Z direction up to 7 T. The current feedback was opened at V = 20 mV and I = 5 nA. (b) Derivatives of dI/dV signals shown in (a). By applying magnetic field up to B_Z=7 T, the amplitude of the central resonance decreased by $\approx 10\%$ and its width increased only by $\approx 0.6\%$. The spectrum of B_Z=3 T is subjected to FFT-filtering for noise removal. 43

3.18 Orbital and spin magnetic moment of Co atom with d^7 electronic configuration for (a) the gas phase, and (b) deposited on Pt(111) surface. Crystal field induced by the surface Pt atoms leads to a strong magnetization of the Co atom. Adapted from [90]. 44

3.19 The ball model of a $CoCu_n$ chain with Co atom attached to the side (left column) and to the end (right column) of the chain. The contour representation of Co $3d$ orbitals illustrates the spatial dependence of their hybridization with the chain Cu atoms. 46

4.1 STM images of a Cu(111) surface with chains and trenches of monolayer height. (a) A Cu chain approximately two atoms wide and a parallel trench. (b) Two wide trenches (approx. 2 and 3 atoms) with deposited single Cu atoms. (c) Monatomic chains and trenches. The images were acquired at (a) V = 20 mV and I = 3 nA and (b, c) V = 100 mV and I = 5 nA [92]. . . 51

4.2 Current-distance data $I(\Delta z)$. Negative values of Δz indicate reduced tip-sample distances with respect to the initial separation defined by I = 200 pA and V = 20 mV. Data recorded from a (111) terrace (black), a Cu adatom, a monatomic chain, a wider chain ($\approx$ 2 atoms), and trenches of monolayer depth with single atom and wider width ($\approx$ 2 atoms) are displayed. The curves are arbitrarily offset along the ordinate for clarity. The terrace data are shown with each curve for comparison. Small undulations of the data are due to low-frequency vibration of the microscope [92]. 52

4.3 The ball model of (a) a single Cu atom and (b) a monatomic Cu chain on Cu(111). The Cu chain and the Cu atom are simulated by two parallel steps and a polygonal prism, respectively. According to Smoluchowski effect, a lower apparent barrier height is expected at the upper edge of the steps. . . 53

5.1 Measured (solid line) and calculated (dotted line) dI/dV as a function of distance from a Cu(111) step edge at different bias voltages. Adapted from [130]. 57

5.2 **(a-i)** STM images of a single Co atom manipulation process on Cu(111) ($V = 250$ mV and $I = 30$ pA). Co atom was positioned at different distances from the step edge and it has the apparent height of ≈ 60 pm. **(j)** Top view of the same step region (12.9 nm × 12.9 nm) to see the spatial oscillation of surface LDOS at 250 meV above Fermi energy. **(k)** Height profile across the white line in (j). **(l)** dI/dV spectra with their corresponding Fano fits (red lines) of the Co atom on Cu(111) terrace with different distances from the step edge. The current feedback was opened at V = 250 mV and I = 420 pA. 58

5.3 (a) STM image of Co adatom close to a step edge of Cu(111) surface (V = 250 mV and I = 30 pA). (b) cross-section along the dashed line in (a). The separation between the adatom and the step edge was measured from the maximum apparent height of the adatom to the mid-rise (MR) point of the step. 59

5.4 Simulated ρ_s oscillations at Fermi energy as a function of the distance from a Cu(111) step edge. Red dots show the Co atom positions in our experiment. The distances from the step were defined according to figure 5.3. 60

5.5 **(a)** Kondo resonances of Co atom positioned at a minimum and a maximum of ρ_s oscillations. Despite the maximum variation of ρ_s, the spectra overlay with a good accuracy. **(b)** Black solid line represents the simulated Fano fit for the resonance in (a). The width of resonance (Γ) was considered as the variable parameter and increased up to the order of three. 61

6.1 (a) STM topograph of deposited C_{60} molecules and a monatomic Cu chain on Cu(111) (V = 125 mV and I = 35 pA). The triplet image is due to the multiple tip asperities. (b) Height profile along the black dashed line in (a). The Monatomic Cu chain is approximately five time smaller than the C_{60} molecule in apparent height. 64

6.2 STM topographs of deposited C_{60} molecules and a wide Cu chain on Cu(111) (V = 10 mV and I = 25 pA). Molecules A and B were attached to the chain by atom manipulation (c) dI/dV spectra acquired on molecule A on (111) terrace, and attached to the chain before and after the molecule B attachment. The current feedback was opened at V = 2.5 V and I = 180 pA. 65

A.1 (a) dI/dV spectra acquired on surface and on Co atom attached to a monatomic Cu chain. (b) dI/dV spectrum resulted from the subtraction of the surface spectrum and the spectrum of the Co at chain (subtraction of the two spectra in (a)). (c) Final spectrum after removal of the linear background from (b). The current feedback was opened at V = 20 mV and I = 5 nA. 68

A.2 dI/dV signal obtained on a Co atom attached to the side of a monatomic chain in the presence of applied out-of-plane magnetic field B_Z=8 T. Using FFT-filtering, the high frequency noise was removed from the original signal. 69

List of Tables

3.1 Extracted values from the fits for the resonance of Co atom at the side of a monatomic chain in the presence of external out-of-plane magnetic field. . . 37

4.1 Apparent barrier heights Φ_{app} extracted from Fig. 4.2 [92]. 53

5.1 Extracted values of the half width half maximum (Γ) and Kondo temperature for different distances from the step edge. The maximum variation of $\approx 10\%$ was observed in the width of the resonance. 59

Abbreviations

DFT	**D**ensity **F**unctional **T**heory
FCC	**F**ace-**C**entered **C**ubic
FFT	**F**ast **F**ourier **T**ransform
FWHM	**F**ull-**W**idth at **H**alf-**M**aximum
HCP	**H**exagonal **C**lose-**P**acked
HWHM	**H**alf-**W**idth at **H**alf-**M**aximum
IETS	**I**nelastic **E**lectron **T**unneling **S**pectroscopy
LDOS	**L**ocal **D**ensity **O**f **S**tates
LUMO	**L**owest **U**noccupied **M**olecular **O**rbital
MAE	**M**agnetic **A**nisotropy **E**nergy
MCA	**M**agneto-**C**rystalline **A**nisotropy
MR	**M**id-**R**ise
QMC	**Q**uantum **M**onte **C**arlo
SES	**S**pin-**E**xcitation **S**pectroscopy
SOC	**S**pin **O**rbit **C**oupling
STM	**S**canning **T**unneling **M**icroscopy
STS	**S**canning **T**unneling **S**pectroscopy
TIC	**T**hermal-**I**solation **C**hamber
UHV	**U**ltra **H**igh **V**acuum

Acknowledgements

First of all, I would like to express my sincere gratitude to my adviser Prof. Dr. Richard Berndt for giving me the opportunity of working in his group. Doing research under his supervision was literally the best working experience of mine. I am so grateful for his help and support.

I also want to thank

Dr. Alexander Weismann for all the support and proofreading of my thesis. Without his help, I would not be able to overcome the experimental obstacles and submitting this thesis.

Roberto Mozara and Prof. Dr. Alexander Lichtenstein for the theoretical calculations and discussions.

Michael Mohr for always coming immediately to the lab and helping me when I called for help at the beginning of my PhD time.

Dr. Johannes Schöneberg for introducing the 4 K lab to me.

Dr. Thomas Jürgens for his help regarding the technical IT issues.

Dr. Manuel Gruber for the information and advice he has shared when I had theoretical questions.

All my former and present colleagues for creating a friendly environment in our group specially Dr. Ling Fu, Dr. Garima Saraswat, Jan Homberg, Dr. Alexandre Artaud, Sven Johannsen, Dr. Peter-Jan Peters, and Dr. Thomas Knaak.

Torben Jasper-Tönnies for the small funny chats about politics and making me laugh.

My first german friend Hans-Joachim Neuman for helping me to get familiar with German culture and make our coffee breaks more enjoyable. He made work a nicer place.

Ms. Monika Seeger and Ms. Claudia Läufer for their help with paperwork.

My old friend and present colleague Nafise kalantari for encouraging me when I was tired.

Finally, I want to thank my parents who always make me feel secure and my Shahab who helped me more than I could imagine.